5-2010

Electron-Induced Electron Yields of Uncharged Insulating Materials

Ryan Carl Hoffmann
Utah State University

Utah State University
MERRILL-CAZIER LIBRARY

ELECTRON-INDUCED ELECTRON YIELDS OF UNCHARGED

INSULATING MATERIALS

by

Ryan Carl Hoffmann

A thesis submitted in partial fulfillment
of the requirements for the degree

of

MASTER OF SCIENCE

in

Physics

Approved:

_____   _____

Dr. JR Dennsion   Dr. D. Mark Riffe
Major Professor   Committee Member

_____   _____

Dr. Michael J. Taylor   Dr. Byron Burnham
Committee Member   Dean of Graduate Studies

UTAH STATE UNIVERSITY
Logan, Utah

2010

ABSTRACT

Electron-Induced Electron Yields of Uncharged Insulating Materials

by

Ryan Carl Hoffmann, Master of Science

Utah State University, 2010

Major Professor: Dr. JR Dennison
Department: Physics

Presented here are electron-induced electron yield measurements from high-resistivity, high-yield materials to support a model for the yield of uncharged insulators. These measurements are made using a low-fluence, pulsed electron beam and charge neutralization to minimize charge accumulation. They show charging induced changes in the total yield, as much as 75%, even for incident electron fluences of <3 fC/mm^2, when compared to an uncharged yield. The evolution of the yield as charge accumulates in the material is described in terms of electron recapture, based on the extended Chung and Everhart model of the electron emission spectrum and the dual dynamic layer model for internal charge distribution. This model is used to explain charge-induced total yield modification measured in high-yield ceramics, and to provide a method for determining electron yield of uncharged, highly insulating, high-yield materials. A sequence of materials with progressively greater charge susceptibility is presented. This series starts with low-yield Kapton derivative called CP1, then considers a moderate-yield material, Kapton HN, and ends with a high-yield ceramic, polycrystalline aluminum oxide. Applicability of conductivity (both radiation induced conductivity (RIC) and dark current conductivity) to the yield is addressed. Relevance of these results to spacecraft charging is also discussed.

(182 Pages)

ACKNOWLEDGMENTS

I will forever be in the debt of my advisor Dr. JR Dennison. His tireless efforts to teach me the practical side of physics has been invaluable in my development as a scientist and as a person. He will never know how much his influence has affected my life and perspective. I would also like to thank all the members of the physics department for always listening; without them it would have been easy to lose touch with reality. In particular I would like to thank Karalee Ransom, Sharon Pappas, and Judy Larsen for always keeping a full candy dish.

I would also like to thank the members of the Materials Physics Group past and present. Josh Hodges, Justin Dekany, Jennifer Roth, Alec Sim, Charlie Sim, and Amberly Evans are not just my colleagues, but they are my friends and will be forever. They have taught me how to let go and have fun even when things are at their darkest. It is only through the influence of the MPG and JR that I have gained the confidence and patience to finish this degree.

My parents deserve my deepest gratitude for raising me and not killing me during my teenage years no matter how much I deserved it. They provided me with an appreciation for education and the ability to question everything. I hope that this degree can help my mother overcome some of the hard feelings she has had for being told to become a home economics teacher. Science is in our blood.

Finally, I would like to give my deepest thanks to my wife, Amy, and three kids, Ari, Ian, and Kael. They have supported me through the last five years through thick and thin. Through late-night homework and this never-ending thesis, they have been there for me, supporting me and offering a much needed distraction. They are my life and I could not be luckier to have them on my side. I would like to thank Ari for all the wrestling; there is soon approaching a day that she will kick my butt…but not yet. I would like to thank Ian for being the most understanding son a man could hope for and tell him that I will be at his disposal very soon. And to Kael I would like to give him the attention he deserves despite the late night screaming. Lastly, I would like to

thank Amy for putting up with all this for the last five years and never letting me doubt that I could do it. It is only through her that I have been able to do this and I will forever be in her debt. We can finally start the next chapter in our lives.

Ryan Hoffmann

CONTENTS

LIST OF TABLES

Table

LIST OF FIGURES

LIST OF SYMBOLS

σ_{max} = the maximum ratio of emitted electron flux to incident electron flux (yield)

σ = ratio of emitted electron flux to incident electron flux (total yield)

E_o = incident electron energy

δ = ratio of secondary electrons to incident electrons (SE yield)

η = ration of backscatter electrons to incident electrons (BSE yield)

Q_{TOT} = total backscatter and secondary charge in Coulombs

Q_{BSE} = backscatter charge in Coulombs

Q_{SE} = secondary electron charge in Coulombs

E_1 = total electron yield first crossover energy

E_2 = total electron yield second crossover energy

E_{max} = incident energy at which σ_{max} occurs

E = kinetic energy of electron

φ = material work function

R = electron penetration depth or range

θ = internal SE trajectory with respect to normal

λ_{se} = mean free path of electron

E_{cr} = critical energy for an electron to escape a material

E_f = Fermi energy

p = electron momentum

p_{cr} = critical normal momentum for electron escape

S = SE's excited per unit energy per unit primary path

m = mass of electron

χ = electron affinity

k = material dependant proportionality constant

V_s = material surface potential

σ_o = uncharged total yield

δ_o = uncharged SE yield

η_o = uncharged BSE yield

eV_s = insulator surface potential barrier

Q_o = total incident charge

D = sample thickness

ε_o = permittivity of free space

ε_r = relative dielectric constant

A_o = cross-sectional beam area

R_{beam} = electron beam radius

σ_{DC} = dark current conductivity

τ = charge decay time

T = temperature

k = Boltzmann constant

I_{Fil} = electron gun filament current

ΔE = thin film interference peak separation

h = Plancks constant

c = speed of light in vacuum

n = optical index of refraction

t = thickness of thin film

N_v = number of valence electrons per atom

E_b = CSDA range

E_m = mean energy lost per collision

b_1/b_2 = component of five parameter SE yield fit

n_1 = component of five parameter SE yield fit

n_2 = component of five parameter SE yield fit

V_{esd} = electrostatic breakdown voltage

Z_{eff} = effective atomic number

J_{in} = beam current density

ρ_d = material density

q_e = charge on electron

k_{ric} = material dependant RIC fitting parameter

Δ = material dependant RIC fitting parameter

δ_{max} = maximum secondary yield

α = alpha crystalline structure

γ = gamma crystalline structure

E_a = activation energy

V_{eq} = equilibrium surface voltage

CHAPTER 1

INTRODUCTION

The focus of this thesis is the electron-induced electron emission from low-conductivity materials ($<10^{-16}$ (Ω-cm)$^{-1}$). This comes as an outgrowth of studies of the charging of spacecraft materials by the USU Materials Physics Group (MPG) over the past 15 years. The central theme of spacecraft charging is how spacecraft interact with the plasma environment to cause charging. Spacecraft materials accumulate negative or positive charge and adopt potentials in response to interactions with the plasma environment. A material's electron emission and electron yield (defined as the ratio of electron flux out of a material to the electron flux into it), determines how quickly net charge accumulates in spacecraft components in response to incident electron, ion, and photon fluxes. The material conductivity determines how quickly that charge is dissipated. Due to their high mobility, incident electrons from the space plasma play a more significant role in electron yield and in resulting spacecraft charging than do positively charged ions. For this reason the focus of this study is on electron interactions and ion and photon interactions are neglected.

The electron emission properties of electrically insulating materials, as a function of incident electron energy, are central to modeling spacecraft charging. Insulating materials generally exhibit higher yields than conducting materials, and accumulated charge cannot be easily dissipated. Therefore, insulating materials can become very efficient at collecting (yield) and storing (conductivity) charge. This becomes a very dynamic problem as electron emission in insulators is complicated by the fact that the emission mechanisms themselves can be influenced by accumulated surface and bulk charge, and in addition, the conductivity of the material can be modified by the energy deposited by the incident electron (Dennison *et al.*, 2008). The net charge that a material will obtain is dictated by the complex interplay of these processes.

This thesis presents a study of the changes in electron-induced electron yield that result from the buildup of internal charge distributions due to incident and emitted electron fluxes. The pulsed method of measuring electron yield is discussed with special attention given to the strengths and limitations of the methods. These limitations are discovered by the investigation of three materials with varying degrees of susceptibility to charging. All of the materials investigated here are good insulators with conductivities ranging from 10^{-16} to 10^{-19} (Ω-cm)$^{-1}$. What changes their charging susceptibility, in the context of this study, is primarily the maximum electron yield (σ_{max}) of the material, ranging from ~1.4 to ~7. To address when the instrumental limit of the pulsed method is reached, a theory and model is developed to understand the evolution of incident and emitted flux in response to the buildup of internal charge distributions. Specifically, we look at how charge buildup in highly charged insulating materials affects these emission fluxes. Quantifiable changes in yields are observed in response to fluences of less than 3 fC/mm^2, and constitute the limit of the experimental methods.

A model for the evolution of total electron yields as a result of surface charging is presented to computationally overcome inherent limitations in the experimental low-fluence, pulsed method. This expression is derived from two physics based models. The first component is the model for the emission spectrum of secondary electrons developed by Chung and Everhart (1974; Chung, 1975). This model is then fit to measured data thereby providing electron yields as a function of both incident electron energy and fluence. The second component is the double dynamic layer model (DDLM) for the multilayer internal charge distributions that develops in response to incident charge (Melchinger and Hofmann, 1995). By combining these component models, we derive an expression for the electron emission yield as a function of incident charge or equivalently surface potential (Cazaux, 1999, 2005; Meyza *et al.*, 2003). An estimate of the intrinsic electron yield curve can be extracted by extrapolating to a minimal accumulated internal charge distribution.

Throughout the body of this text there are explanations of how the data can be interpreted using the ideas developed to quantify how charging affects the yield. Some of the measurements at first glance appear to be nonsense, but arguments related to charging will be made for each eccentricity seen in the data.

The Coulomb force is the strongest long range fundamental force known (Thomson, 1897); this fact makes yield measurements in insulators exceptionally difficult. The interactions between electrons, both primary and secondary, are so strong that just a handful of either can interfere with the measurement, making it difficult to obtain "intrinsic" data about a material. As a result, great care must be taken to minimize the flux density of incident and secondary electrons, thereby minimizing their interactions. This thesis will qualitatively discuss the evolution of methods undertaken to measure the electron-induced electron yield in highly insulating materials, and present representative data to quantify the effectiveness of these new methods.

Two basic approaches have driven all the decisions and work described in this thesis. The first approach is to minimize the flux density used in the probe pulse. This has motivated the work on noise mitigation and management, as well as the theory developed to extrapolate to a flux density approaching zero. The second concept is to neutralize the surface voltage that develops as a result of the probe beam. This has lead to the development of UV and electron flooding charge neutralization capabilities, and the use of thermal modification of the conductivity as well as consideration of RIC enhancements. All the work presented here can be traced back to these two basic concepts.

The body of this text is organized into four main sections. Chapter 2 provides a theoretical framework for electron-induced electron yield and how it can be modified by induced surface potential. This theory section includes an overview of the secondary electron energy distribution and the physics based model developed by Chung and Everhart to describe the

secondary electron emission energy spectrum. This model is then related to the development of surface potential as the material is bombarded with electrons. This development is then shifted to the dual dynamic layer model (DDLM) that describes the internal charge distribution in the material during electron bombardment. The final subsection in the theory section combines these two models to form a model that describes how the total yield of a material will be modified by surface potential.

Chapter 3 describes instrumental capabilities and upgrades that have been developed to verify and implement the models developed in the theory section. Simple DC yield measurements using a continuous monoenergetic incident electron beam to measure the yield of a conducting gold sample are discussed to verify the systems basic operation. Next, DC secondary electron emission spectra are shown for an unbiased gold sample to establish baseline electron emission spectra functionality. Next, pulsed-yield measurement techniques are discussed, as they apply to insulators. This discussion includes charge neutralization techniques and careful beam characterization.

Chapter 4 shows the results of three sets of the measurements on three distinct materials. These materials were chosen to demonstrate the range over which the techniques described herein are valid. First, the data measured from a material, CP1, with relatively low conductivity ($\sim 10^{-19}$ $(\Omega\text{-cm})^{-1}$) and a low maximum total electron yield (σ_{max}=1.4) are shown. This material charges slowly because of its low yield, but what charge is accumulated is dissipated slowly (many hours) because of its low conductivity. Next, we investigate a material with more challenging material parameters. Kapton HN has a low conductivity ($\sim 10^{-19}$ $(\Omega\text{-cm})^{-1}$), but still maintains a moderate maximum total yield of σ_{max}=2.2. This material provides an intermediate step as it is charges more quickly due to its low yield, and the charge that is accumulated will remain for a very long time (many hours) due to its low conductivity. The final material presented here is the most challenging. Polycrystalline aluminum oxide has a very high maximum total yield σ_{max}=7, and

low conductivity ($\sim 10^{-16}$ $(\Omega\text{-cm})^{-1}$), thus making it very efficient at both collecting charge and storing it. The charge decay time of this material is less (hundreds of seconds) than the two previous materials, but it is still long in comparison to the time scale of the measurement (~ 5 sec). By investigating these materials we can establish the strengths and weaknesses of the instrumentation and methods described in this thesis.

The final section (Chapter 5) in this work provides a summary of all the ideas and information that have been learned throughout the course of this study. This section provides the reader with a broad understanding of material charging and how charging can affect the yield over a broad range of incident energies. This section will also provide a framework for future studies to be made by the Materials Physics Group at USU.

CHAPTER 2

MODELING YIELD MODIFICATION

In order to lay down a framework for the following discussion we must review the fundamental process involved in electron emission. Total electron yield, secondary electron (SE) yield and backscatter electron (BSE) yield and the processes involved in each are discussed. A treatment of electron emission spectra in the context of electron yield and based on the model proposed by Chung and Everhart (1974) follows. This leads to a conversation involving bulk charge accumulation and distribution models and their effect on electron emission spectra and subsequently on total electron yield measurements. This theoretical framework motivates the instrumental development described in Chapter 3, and provides an underpinning for the new model for the response of the electron yield to evolving surface potential developed in Section 2.4.

2.1 Electron Emission

The total yield, $\sigma(E_o)$, is the ratio of emitted flux to incident flux where E_o is incident flux energy. The secondary electron (SE) yield, $\delta(E_o)$, is this ratio for emitted electrons that originate from within the sample, which by convention, are delimited as having energies <50 eV (Seiler, 1983; Reimer, 2000). The backscattered electron (BSE) yield, $\eta(E_o)$, is this ratio for emitted electrons that originate from the incident source to incident electrons (by convection with energy >50 eV), as shown in FIG. 2.1. $\sigma(E_o)$ and $\eta(E_o)$ can also be expressed as the ratio of the sample emitted current to the total incident electron current as

$$\sigma \equiv \frac{Q_{SE} + Q_{BSE}}{Q_{TOT}} = \frac{\int (I_{SE} + I_{BSE}) \cdot dt}{\int I_{TOT} \cdot dt},$$

(2.1)
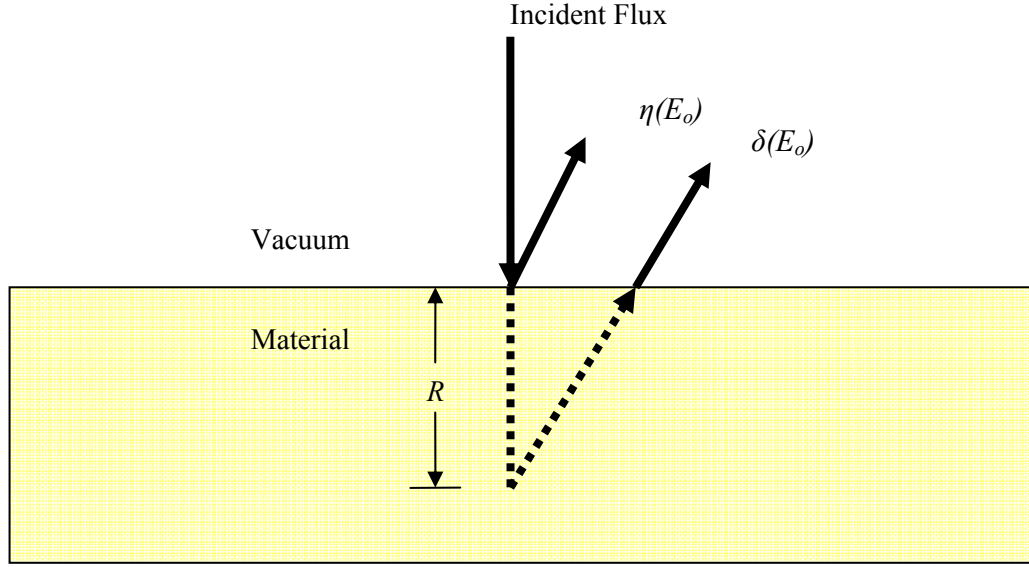
FIG. 2.1. Diagram of incident electron flux impinging on a generic material. $\eta(E_o)$ denotes the backscatter electrons that originate from within the incident beam that have energies >50 eV. $\delta(E_o)$ denotes the secondary electrons liberated from within the material that have energies <50 eV.

$$\eta \equiv \frac{Q_{BSE}}{Q_{TOT}} = \frac{\int I_{BSE} \cdot dt}{\int I_{TOT} \cdot dt},$$

(2.2)

and

$$\delta \equiv \frac{Q_{SE}}{Q_{TOT}} = \frac{\int I_{SE} \cdot dt}{\int I_{TOT} \cdot dt},$$

(2.3)

where Q_{TOT}, Q_{BSE}, and Q_{SE} are, respectively, the total, BSE and SE charge in Coulombs to and from the material (Thomson, 2004).

An electron yield curve of gold shows the yield as a function of incident electron energy, E_o (see FIG. 2.2). The total yield curve can be characterized in terms of five parameters: (i and ii) the first and second crossover energies, E_1 and E_2, occur when the total yield is equal to unity and no net charge is deposited; (iii and iv) the yield peak, σ_{max}, is the maximum yield and occurs between the crossover energies at E_{max} (the maximum yield is typically found between

$200 < E_{max} < 1000$ eV.); and (v) the rate at which the yield approaches the asymptotic limit, $\sigma(E_o \rightarrow \infty) \rightarrow \sigma_\infty$, with increasing beam energy (Abbott and Dennison, 2005).

The electron emission properties of conductors are relatively easy to measure, because emitted electrons are rapidly replaced by connecting the material to ground (Nickles, 2002; Dennison *et al.*, 2004). However, yield measurements on dielectrics are more difficult because of the inability to ground the dielectric and the resulting response of the yield to charge accumulation (Thomson, 2004; Sim *et al.*, 2005). Accumulated charge in insulators interacts with both incident and emitted charged particles through Coulomb interactions and affects electron emission in the production, transport and emission stages of emission models, as reviewed in Thomson (2004). Surface potentials resulting from the accumulated charge can influence yields by altering incident (landing) energies, by affecting the escape energies of secondary electrons (SEs) and backscattered electrons (BSE), or by reattracting (repelling) low-energy SE to a positively (negative) charged surface.

When measuring the yield of insulators, it is important to consider the effects of charging on the total and BSE yields. To understand this more fully we must review the electron emission spectrum and how it is affected by charging.

2.2 Electron Emission Spectra

2.2.1 SE Energy Distribution Model

When a material is exposed to high-energy electron irradiation, electrons can be from the material, and have a range of emission energies from 0 eV up to the incident electron energy, E_o. The escape energies of SE's depend on their production depth, as well as the energy-loss mechanisms and potential barriers experienced before exiting the material. A typical electron emission spectrum from polycrystalline gold with incident electron energy of ~400 eV is shown in FIG. 2.2. The electron emission spectrum of both conductors and insulators appear very similar

in shape, however charging from the beam causes the SE peak from insulators to shift and the high energy tail to fall off more gradually. Generally in uncharged materials, for incident energies >50 eV, a large population of electrons are emitted with energy <50 eV. Most of these electrons have undergone inelastic scattering interactions such that they have developed a well-defined energy distribution within the material before they escape the surface. An energy distribution generally exists at the energies near the incident beam energy that is comprised of elastically and quasi-elastically scattered electrons (Kite, 2007).

Chung and Everheart provide a useful model for the SE emission spectra, which expresses the energy distribution of the number of emitted SE per unit energy, *dN(E;E$_o$)/dE*, in terms of the work function for metals, ϕ. As this work is at the heart of the electron yield work presented here, it is important that we summarize the model. For a full derivation, the papers by Chung and Henke should be studied (Chung and Everhart, 1974; Henke *et al.*, 1979).

An energetic electron impinging on a semi-infinite material in a vacuum is depicted in FIG. 2.1. The incident electron impinges on the target along the z axis and penetrates to some range, *R*. Wilson provides a discussion of the energy dependence of *R* and its relation to inelastic mean free path, as well as a semi-empirical model of the yield from 40 eV to >10 MeV (Wilson and Dennison, 2010). We assume that all directions of motion of an internal excited SE are equally probable. We also assume that any scattering of the internal SE with the ambient electron gas produces absorption, hence only electrons that do not scatter between their point of origin and the surface can escape.

Consider an excited SE electron generated at depth *R* in FIG. 2.1 moving in a direction θ with respect to the normal. Due to the diverse nature of scattering processes involved, the SE transport process has generally been modeled as a diffusion process, where the probability a SE will reach the surface decays exponentially with creation depth, and varies with the associated SE
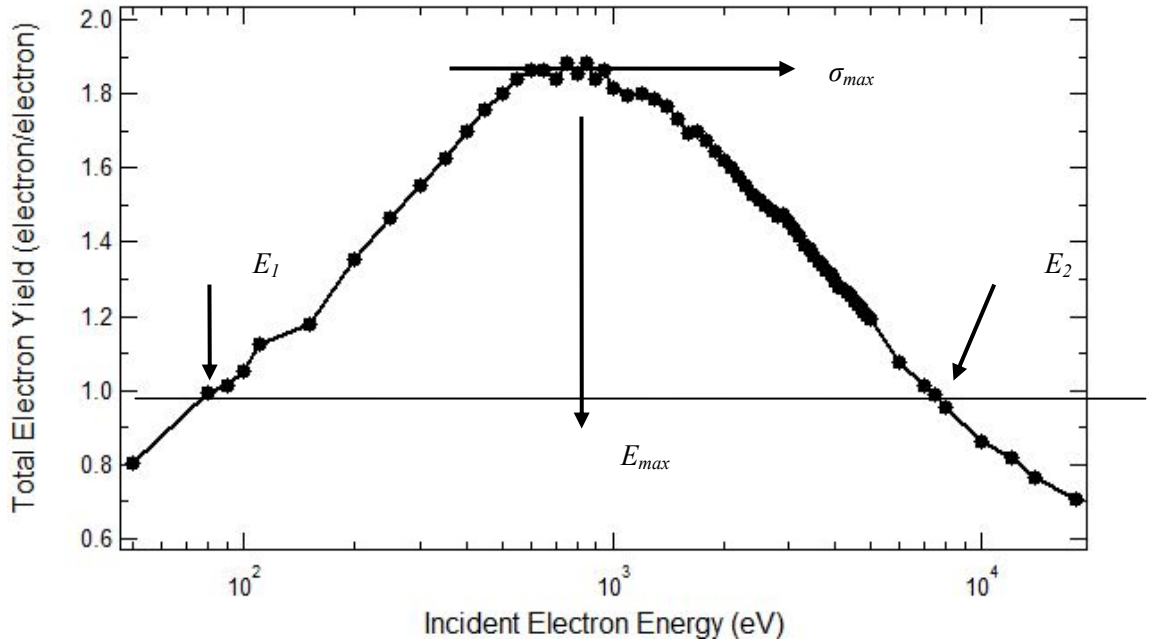
FIG. 2.2. Total electron yield of polycrystalline Au as a function of incident energy.
Data were taken using a DC electron beam. E_1 and E_2 are the first and second crossover energies.
The yield peak, σ_{max}, is the maximum yield and occurs between the crossover energies at E_{max}.

escape depth of the material (Lye and Dekker, 1957; Dionne, 1975). The probability that it will

reach the surface without a collision is given by

$$P(E,\theta,R) = \exp\left[\frac{-R}{\lambda(E)\cos\theta}\right]_,$$

(2.4)

where $\lambda(E)$ is the mean free path (MFP) of an excited internal electron with energy E. In order for

a SE to escape, E must be greater than a critical value E_{cr} that is given by,

$$E_{cr} = E_f + \phi_,$$

(2.5)

where E_f is the Fermi energy and ϕ is the work function of the target conductor. When the

condition $E > E_{cr}$ is met the maximum value of θ for escape is determined by requiring the normal

component of the momentum, $p \cos(\theta)$, must at least be equal to the magnitude,

$$p_{cr} = (2mE_{cr})^{\frac{1}{2}}.$$

(2.6)

We assume that all SE's with a normal component of momentum corresponding to an energy greater than the surface barrier height have unit probability of escape. For now the surface reflection and refraction effects are neglected for the purpose of this work, however Olifant (2009) provides correction terms to include reflection and refraction in the Chung and Everheart (1974) model. We now have the condition, $0 \leq \theta \leq \cos^{-1}(p_{cr}/p)$, for $E \geq E_{cr}$, where $E = p^2/2m$ in a free electron model.

The number of SE's excited per unit energy into an energy interval between E and $E + dE$ per unit primary path is denoted by $S(E, R)$. The energy distribution per unit primary path is given by

$$\frac{d^2 N}{dE\, dR} = \frac{1}{2} \int_0^{\cos^{-1}\left(\frac{P_{cr}}{p}\right)} S(E, R) \sin \theta \exp\left[-R/\lambda(E)\cos\theta\right] d\theta.$$

(2.7)

In Eq. (2.7) it is assumed that the primary electron moves in a straight line along the z axis inside the solid. This assumption is accurate for high-energy electrons, but becomes an approximation at lower energies as the mean free path (MFP) of low-energy electrons is smaller and therefore more likely to undergo a collision in the first few hundred angstroms of the material where the SE's are produced.

Equation (2.7) can be further simplified by assuming that $S(E,R)$ is independent of R and is equal to $S(E)$ within the MFP of a SE from the surface. We now integrate Eq. (2.7) from 0 to ∞. The upper limit of the integration is not critical as long as the MFP of the low-energy SE is small compared to the high-energy primary electrons. Hence Eq. (2.7) reduces to

$$\frac{dN}{dE} = \frac{S(E)\lambda(E)}{4}\left[1 - \left(\frac{E_f + \phi}{E}\right)\right].$$

(2.8)

The functions *S(E)* and *λ(E)* have been derived in the work presented by Stolz and Kanter respectively (Stolz and Streitwolf, 1958; Kanter, 1961). Upon substitution of these functions Eqs. (2.4, 2.5, and 2.6) into Eq. (2.8) we find that only the function

$$\frac{dN(E;E_o)}{dE} = \frac{k}{E_o} \frac{E}{(E+\phi)^4}$$

(2.9)

determines the shape of the energy distribution curve for SE emission. There is a prefactor, but it is material dependant and only contributes to the magnitude of the peak, the position of the peak and the full width at half max are both determined by Eq. (2.9).

The work function, ϕ, in Eq. (2.9) represents the energy required for a SE to escape from a material's surface. Since the measured SE energy distribution of both conductors and uncharged insulators are similar in shape, with the spectral magnitudes controlled by surface energy barriers (i.e., work function or electron affinity) it is reasonable to extend the Chung and Everhart model to uncharged insulators by replacing the work function term with the insulator electron affinity, χ (Baroody, 1950; Quinn, 1962; Thomson, 2004). *E* is the SE emission energy and *k* is a material dependent proportionality constant and as before E_o is the incident electron energy,

$$\frac{dN(E;E_o)}{dE} = \frac{k}{E_o} \frac{E}{(E+\chi)^4}$$.

(2.10)

Measured emission spectra for Au are shown in FIG. 2.3. The same data along with a fit based on the Chung-Everhart model and Eq. (2.9) are shown in FIG. 2.4a. The measured peak position of (2.5 ± 0.2) eV, minus a (0.583 ± 0.002) eV offset energy, is in agreement with a peak energy value of 1.9 eV reported in Reimer (2000). The measured FWHM of (4.6 ± 0.3) eV agrees with the previous published value of 4.4 eV. The work function ϕ derived using Eq. (2.9) for Au is measured as 4.3 eV using the electron-induced emission spectrum. The accepted work function for clean Au in vacuum is 5.2 eV, while the value in air is reduced to perhaps 4.8 eV due to minimal contamination (Hansen *et al.*, 1989). A prediction of the Chung and Everhart model is
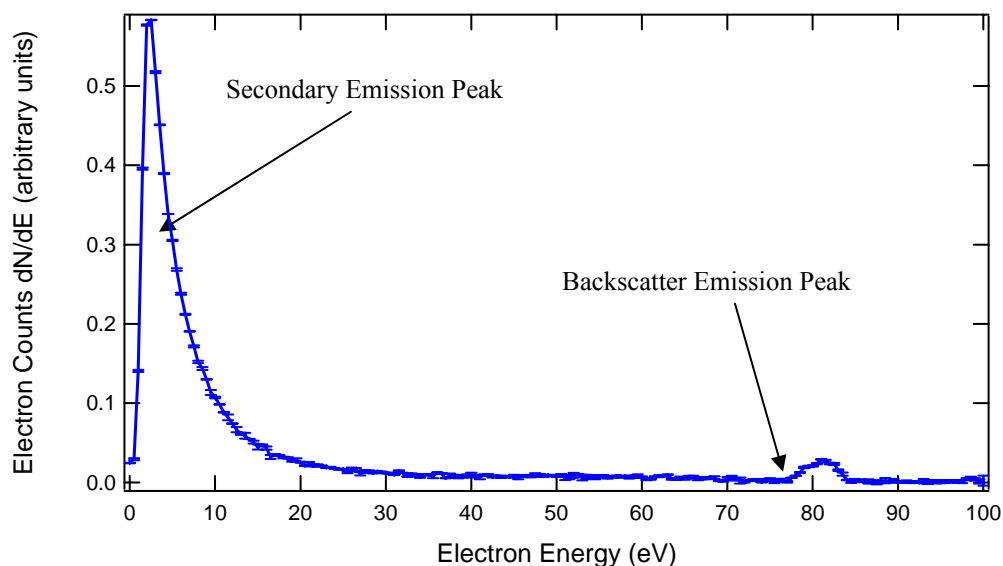
FIG. 2.3 Electron emission spectra from polycrystalline Au.
Acquired using the Hemispherical Grid Retarding Field Analyzer (HGRFA). Note secondary and backscatter peaks.

that the peak energy is one third of the work function; the measured ratio of peak energy to work function is 0.44, in reasonable agreement with the model. A spectrum of the same Au sample taken with a ~80 eV primary beam and an external sample bias of -20 V relative to the grounded inner grid is shown in FIG. 2.4b. The measured peak position is 24.2 ± 0.2 eV with a FWHM value of 8.5 ±0.2 eV. The work function found from fitting the data with Eq. (2.10) is 9.0 ± 0.1 eV. None of these values compare favorably with published values and do not validate the assumption made in the next section that the shape of the SE emission curve does not change with surface potential. It may be that the grid peak, as discussed in Section 3.1.2, needs to be properly subtracted from the electron emission curves before a valid comparison of peak shapes at different incident energies and sample biases can be made. This is an area that will have to be explored both in the theory and measurements.

This lends credibility to the model as a reasonable approximation of energy distribution of SE excited from a conductor. We have also provided a reasonable justification for extending the Chung model for conductors, to approximate the energy distribution of the SE from
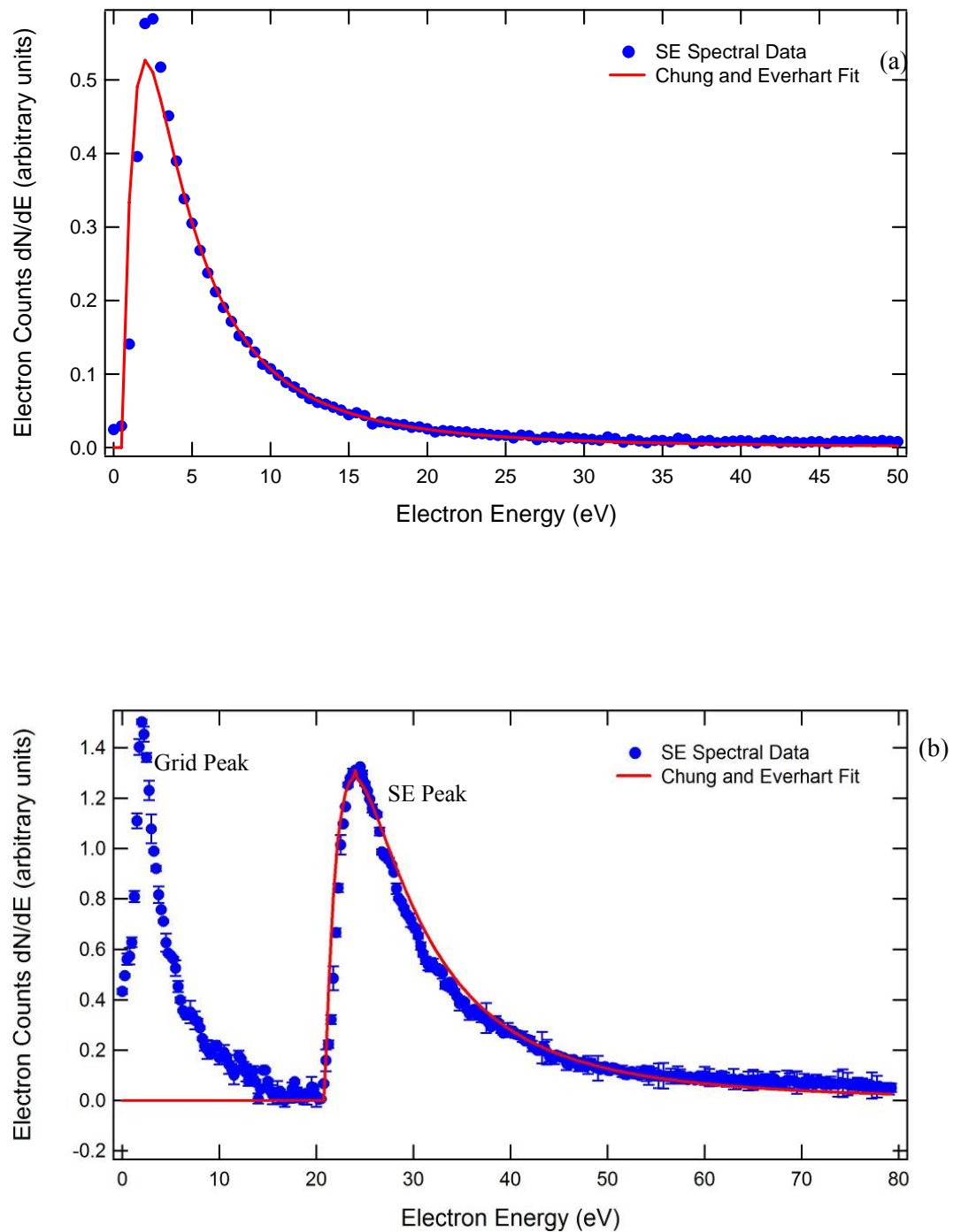
FIG. 2.4. Electron emission spectra from unbiased and Au biased.
(a) Is the emission spectra from an 80 eV beam on grounded Au fit to the model developed by Chung and Everheart, Eq. (2.9). (b) Shows the Chung and Everheart model for 80 eV SE emission on a Au sample biased to -20 V.

insulators. However, it would be beneficial to perform a thorough review of previous literature, particularly of Chung and Everhart (1974), Baroody (1950), and Quinn (1962), to make any necessary modification and interpretations to the Chung and Everhart model as applied specifically to dielectric material SE distribution theory. Such modification could involve differences in the conductor and insulator SE production terms, *S(E)*, mean SE escape depth, *λ(E)*, electric-field assisted SE transport, as well as the associated surface escape terms of electron affinity, *χ*, and surface potential, *V_s*.

2.2.2 SE Energy Distribution Related to Charging Modified Yield

The SE yield in terms of *N(E)* is given by integrating Eq. (2.10) from 0 eV to the cutoff from the definition of a secondary electron energy of 50 eV,

$$\int_{0eV}^{50eV} \frac{dN(E;E_o)}{dE} dE = \delta_o(E_o) + \eta_o(E_o) - 1 = \sigma_o(E_o) - 1. \tag{2.11}$$

In terms of the total yield this integration is the number of excess electrons that contribute to the yield being greater than or less than unity. Here

$$N \equiv \frac{N_{emitted} - N_{incident}}{N_{incident}} = \sigma_o(E_o) - 1 \tag{2.12}$$

is the net number of excess emitted electrons, leading to the one on the right side of Eq. (2.11). The subscript o in σ_o, δ_o and η_o denotes the uncharged total, secondary and backscatter yields to distinguish between the charged versions of these yields.

Between the total-yield crossover energies where the total yield *σ* =1, *E_1* and *E_2*, the polarity of insulator charging is positive (since the total yield is greater than one), and due to the reattraction of low-energy secondary electrons, the insulator attains a steady-state surface potential of just a few volts positive. This positive charging decreases the insulator surface potential barrier by an amount *eV_s*, where *V_s* is the positive surface potential. Hence, the resulting secondary electron yield emitted from a positively charged specimen can be expressed as an

integral of the uncharged spectrum (taken at the same incident energy) with the integration limits extending from the positive surface potential up to the arbitrary 50 eV limit of SE energy. This is depicted by the shaded region in FIG. 2.5a. $\eta(E_o)$ is assumed to be unaffected by the built up potential in the following discussion because η is roughly constant above ~150 eV (see Fig. 4.32). The total electron yield σ, at incident energy E_o for the sample potential V_s is,

$$\int_{eV_s}^{50eV} \frac{dN(E;E_o)}{dE}dE + 1 = \delta(E_o;V_s) + \eta_o = \sigma(E_o;V_s).$$
(2.13)

This integral can be solved analytically by direct substitution of Eq. (2.10) into Eq. (2.13)

$$\sigma(E_o;V_s) = \frac{k}{6E_o}\left[h(eV_s;\chi) - h(50eV;\chi)\right] + 1,$$
(2.14)

where

$$h(\alpha;\chi) \equiv \frac{3\alpha + \chi}{(\alpha + \chi)^3},$$
(2.15)

and α is an arbitrary energy at which h is evaluated (Thomson, 2004).

The positive surface charge inhibits the escape of lower-energy SE's, thus suppressing the lower-energy portion of the SE spectrum. This is represented by the shaded area in FIG. 2.5a showing a emission spectrum from aluminum oxide with 400 eV beam energy fitted with the Chung and Everheart model and parameters $k = (5.93 \pm 0.01) \cdot 10^5$ electron·eV^3 and $\phi = (5.3 \pm 0.1)$ eV. Consequently, only the unshaded area of the electron energy spectrum (above eV_s) contributes to the charged electron yield. It follows that the fraction of the total yield escaping the surface is

$$H(V_s;\chi) \equiv \frac{\sigma(E_o;V_s,\chi) - 1}{\sigma_o(E_o) - 1} = \frac{h(eV_s;\chi) - h(0eV;\chi)}{h(50eV;\chi) - h(0eV;\chi)}.$$
(2.16)

As illustrated in FIG. 2.5b, Eq. (2.16) gives the fraction of the generated SE's that have enough energy to overcome the surface potential and contribute to the yield. Between the crossover energies, typical fractional SE yields for insulators approach values of 0.2 to 0.6,
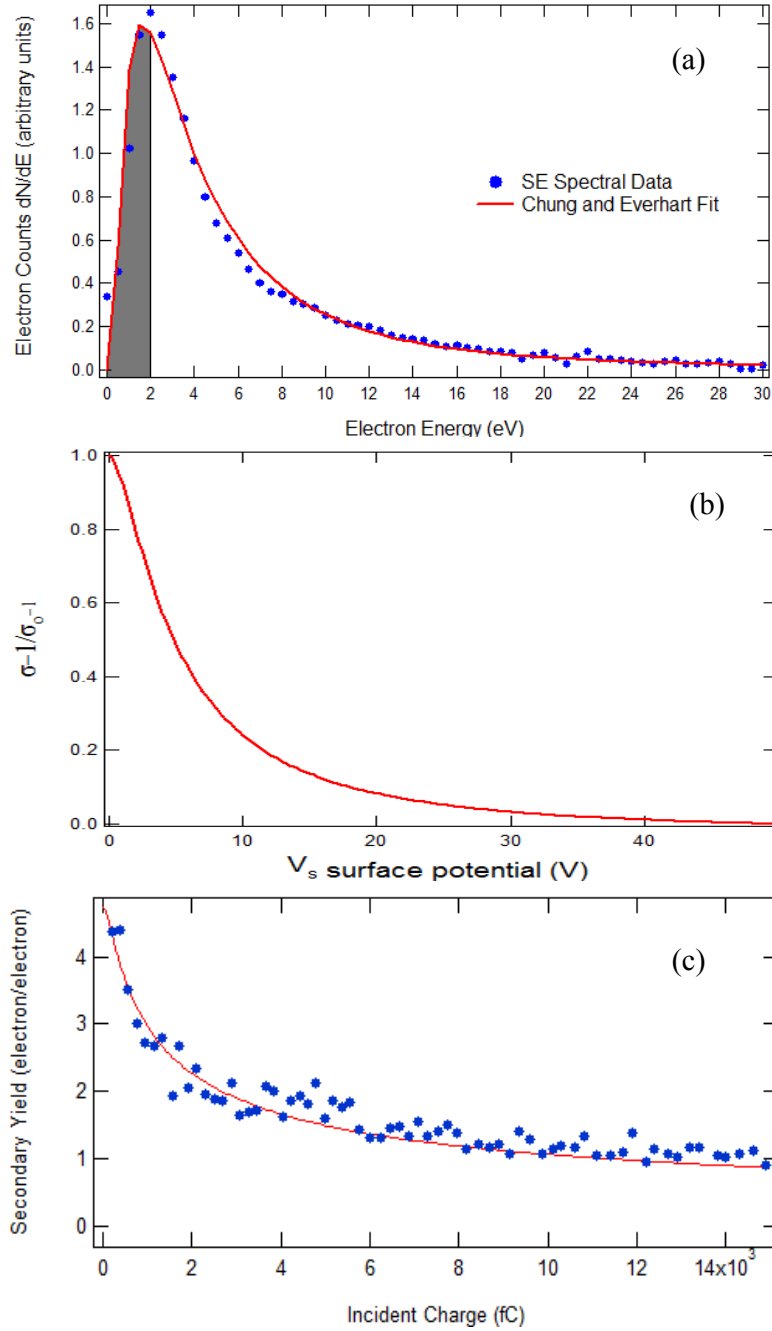
FIG. 2.5. Fraction of SE escaping a surface potential V_s.
(a) Electron emission spectrum on Al_2O_3 produced from a 400 eV electron beam. The shaded region represents the SE recaptured by a positive surface potential of ~2 eV. (b) The fraction of SE allowed to escape the surface as a function of evolving positive surface potential V_s in the positive charging region where $E_1 < E_0 < E_2$. (c) Yield decay curve taken on polycrystalline Al_2O_3 at 200 eV. The red line is the fit developed in Section 2.4 based on Eqs. 2.17 and 2.19.

corresponding to positive surface potentials of 3 to 8 V. For charged insulators, this is the fraction

of secondary electrons that escape the sum of the intrinsic electron affinity and the positive

surface potential created by accumulated charge. Using Eq. (2.16), to solve Eq. (2.13) for the

secondary yield as a function of surface potential, V_s, we obtain

$$\delta(E_o, V_s; \chi) = \sigma(E_o, V_s; \chi) - \eta_o(E_o) = [\sigma_o(E_o) - 1]H(V_s; \chi) - \eta_o(E_o) + 1 \qquad (2.17)$$

σ_o is the uncharged total yield; in practice this becomes the minimally charged yield and is used

as a fitting parameter. With χ, the electron affinity, representing an intrinsic material property, Eq.

(2.17) is a two parameter analytic expression for the yield as it responds to an evolving surface

potential. At this point it is necessary to find an expression for V_s as a function of incident flux

density.

2.3 Charge Distribution in Insulators

Let us consider a succession of progressively more sophisticated charge distribution

models for floating conductors above a grounded plane, as illustrated in FIG. 2.6. For the

purposes of this discussion we will focus only on the incident electron energies between the

crossover energies (i.e., the positive charging regime).

For charged floating conductors, the charge resides near the surface in accordance with

Gauss' law (see FIG. 2.6a). The simplest model for ideal insulators assumes that the charge does

not move appreciable distances within the material after deposition (e.g., that resistivity is

infinite), and that the net accumulated charge is in a single planar distribution at a depth equal to

the penetration depth or range of the primary electron, $R(E_o)$ (see FIG. 2.6b). This is the Bethe

approximation (Bethe and Heitler, 1934). For both of these cases, the deposition of the net total

accumulated charge, $Q_o(\sigma\text{-}1)$, can be modeled as a single charge layer at the surface of a sample

of thickness, D. Using a simple parallel plate capacitor model with the net total electron yield

dependence included gives
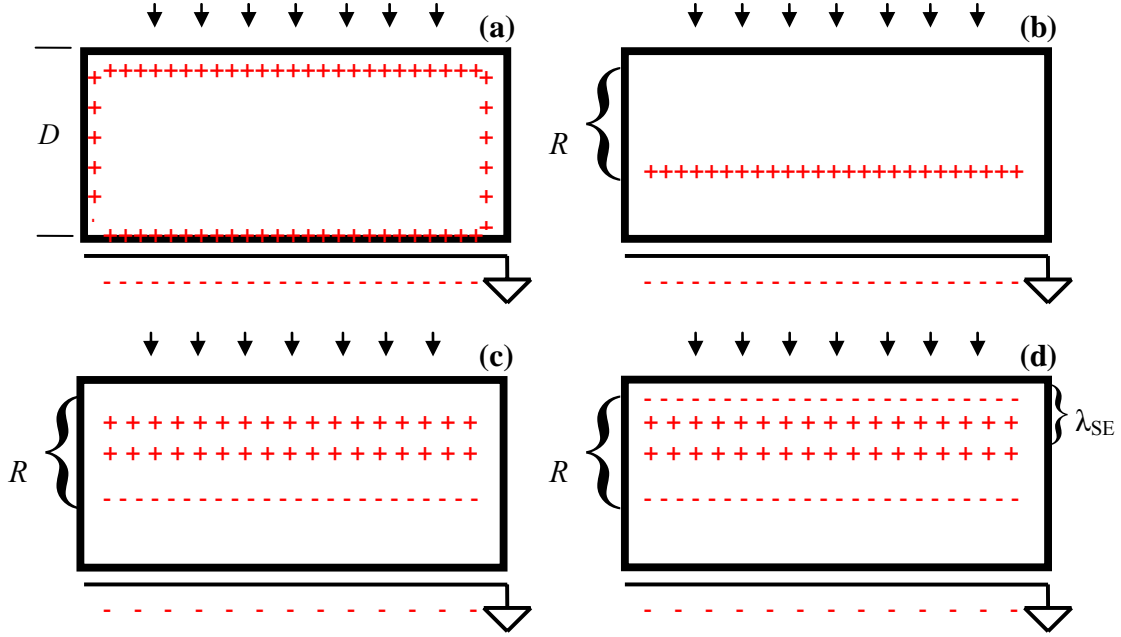
FIG. 2.6 Succession of progressively more sophisticated charge distribution models. (a) A charged floating conductor with charge residing very near the surface. (b) An ideal insulator with the simplest single-layer model of charge accumulation. In this model, the net charge resides in a thin layer at a depth equal to the penetration depth of the primary electron, $R(E_o)$. (c) A double-charge distribution (positive–negative) is formed from embedded incident electrons at a depth $R(E_o)$ and a positively charged region, from SE depletion, between the surface and λ_{SE}. (d) A more complex model of an ideal insulator with an additional layer for the SE reattracted to the surface by the positive charge within the insulator.

$$V_s = \frac{Q_o(\sigma - 1) D - R}{\varepsilon_o \, \varepsilon_r \, A_o}$$ (2.18)

,

where Q_o is the total incident charge, ε_o is the permittivity of free space, ε_r is the relative dielectric constant, and A_o is the cross sectional beam area. As expected, for Eq. (2.18), V_s is positive (negative) for σ greater (less than) unity and in the limit where $\sigma \rightarrow 1$ no charging occurs.

While this model provides a useful first order approximation for the surface potential, it is simplistic in its treatment of the internal charge distribution. Finite resistivity allows relocation of charge within the insulator, leading to more complicated internal charge distributions. Previous models of insulators have shown that the internal charge distributions (both evolving distributions, as well as static charge distributions) resulting from incident electron irradiation,

form multiple alternating positive and negative charge layers (Melchinger and Hofmann, 1995; Usui *et al.*, 2003), Measurements of internal charge distributions of thin-film insulators, for higher incident energies and thicker films, confirm the general nature of these distributions (Takada *et al.*, 2006). However, the spatial and charge-polarity configurations of these layers can be complex and difficult to predict. The SE distributions can depend on a number of factors that include the magnitude of electron yield, electron yield crossover energies (particularly E_2), material conductivity (both dark current (DC) and radiation induced conductivities (RIC)), dielectric strength, electron trapping and detrapping rates, incident electron penetration depths, mean SE escape depths, and incident electron fluxes and energies (Dennison *et al.*, 2007). The combination of these layers is what defines the overall magnitude of the surface potential. Thomson provides a useful review of the literature on models of charge distributions within insulators, with application to electron emission from insulators (Thomson, 2004).

A somewhat more realistic double-layer model is illustrated in FIG. 2.6c. Between the crossover energies, incident electron penetration is only somewhat larger than the SE escape depth, or mean free path, λ_{se}. The negatively charged planar distribution results from embedded incident electrons stopped at a depth $R(E_o)$. The use of a single depth follows from the Bethe approximation for primary electron (PE) stopping power used in the Sternglass formulation of the secondary electron (SE) yield formula (Bethe and Heitler, 1934; Sternglass, 1950). A positively charged region is formed by SE depletion that occurs between the surface and λ_{se}. The electric field from the negative charge again retards further incident electron penetration and acts to drive a greater number of low-energy SE from the sample, thereby enhancing the positive charge region (Jbara *et al.*, 2001; Hoffmann and Dennison, 2006).

The electric field from the positive charge region, in turn, acts to reattract the lowest energy SE emitted from the surface (gray region in FIG. 2.5a), thereby establishing a shallow negative surface charge region (see FIG. 2.6d). For this charging scenario, the dynamic double

layer model (DDLM) has been presented in the literature to predict ensuing internal electric fields

and potentials (Melchinger and Hofmann, 1995; Cazaux, 1999, 2003; Meyza *et al.*, 2003). For the

DDLM charge distribution deposited over the penetration range, the surface potential can be

approximated assuming a parallel-plate capacitor geometry as

$$V_S = \frac{Q_O D}{\varepsilon_o \varepsilon_r A_o}\left[(\sigma - 1) - \sigma\frac{\lambda_{se}}{2D} - \frac{R}{2D}\right]. \tag{2.19}$$

The first term is from the net charge distribution of magnitude $Q_o(\sigma\text{-}1)$ given by Eq.

(2.18), the term involving λ_{se} describes the positive charge distribution of magnitude $Q_o\sigma$ from SE

emission, and the term involving R is from the embedded PE distribution of magnitude Q_o. The

thin-film capacitor geometry is a reasonable approximation since the charge deposition area A_o,

which is determined by the electron beam radius R_{beam}, is much greater than R, and λ_{se} (for studies

reported here, R_{beam} was on the order of 0.85 mm, whereas insulator thicknesses ranged from 5

μm to 1 mm). Furthermore, it can be seen that the first term in Eq. (2.19) dominates if the

insulator thickness D is much greater than R or λ_{se} (R did not exceed ~1 μm for the incident

energies reported here as seen in FIG. 4.6). This approximation is equivalent to assuming a

uniform charge distribution, as given in Eq. (2.18). Notice that V_s is also a function of the total

yield $\sigma(Q_o)$, which itself is dependent on incident charge.

This model provides a useful and accurate depiction of the internal charge distribution

resulting from an impinging electron beam. It is reasonable to assume that this distribution

remains static as long as the material inhibits significant redistribution in response to internal

electric fields. This is true for materials with charge decay times that are much longer than that of

the experiment. We can estimate how material conductivity corresponds to charge decay time by

using Eq. (2.18) and model the distribution as a simple parallel plate capacitor. This allows us to

relate conductivity σ_{DC} to the decay time τ in the form (Brunson, 2009)

$$\tau = \frac{\varepsilon_r \varepsilon_o}{\sigma_{DC}}, \tag{2.20}$$

where ε_r is the dielectric constant of the material and ε_o is the permittivity of free space. Using Eq. (2.20), materials with conductivities $>5 \cdot 10^{-15}$ $(\Omega\text{-cm})^{-1}$ have a charge decay time that is much longer (>300 s) than our experiment (typically 5 s). This does not include the complex internal charge distribution discussed in this section, but it is an adequate treatment for determining charge decay times.

2.4 Response of Total Yield to Evolving Surface Potential

We can now combine our expression for the electron yield in terms of the Chung and Everhart model of electron emission, Eqs. (2.11-2.13), with a model of the surface voltage in terms of incident charge from the DDLM model, Eq. (2.19), to derive a model for the evolution of the yield in response to positive surface potential. Both of these component models are physics based and have been experimentally supported (Melchinger and Hofmann, 1995; Griseri *et al.*, 2004; Takada *et al.*, 2006). In order to proceed and combine these two expressions, we need to make several assumptions:

The energy distribution of emitted electrons given by Eq. (2.9) does not change shape with charge accumulation, but only changes amplitude and peak position. Experimental evidence for both biased conductors and charged insulators, as well as the theoretical development by Chung and Everheart (1974, 1977; Shih *et al.*, 1997a), suggest this is a reasonable assumption.

While these assumptions make the derivation possible, we still encounter considerable difficulty when merging these two models, because of the limit of integration for Eq. (2.13). This is due to the fact that V_s is itself a function of the total yield σ. In order to get an expression for measured electron yield decay data σ verses accumulated incident charge (or, equivalently, surface potential), one need only plot $\sigma(E_o, V_s)$ verses $Q_o(V_s)$ with either V_s or Q_o defined implicitly. It can be seen in FIG. 2.5c that the model described above provides a good fit to the decay curve taken at 200 eV on polycrystalline aluminum oxide.

CHAPTER 3

INSTRUMENTAL UPGRADES TO MINIMIZE SAMPLE CHARGING

The intent of this section is to detail the modifications made to the chamber during the course of this work. There are two areas of focus for instrumental upgrades. The first is charge mitigation and includes efforts to reduce pulse duration so that smaller pulses will be measurable above the systematic background noise. To do this, grounding was improved, cables shortened, noise sources removed and the beam characterized. The second focus is to improve the techniques used to dissipate accumulated charge. This includes low-energy (< 5 eV) electron and UV photon flooding and sample heating. All of this is done in an effort to increase the capabilities of the chamber to better measure the materials with high-resistivity and high-yield.

The work contained in this thesis was performed in the electron emission analysis chamber maintained by the Materials Physics Group. This chamber can simulate diverse space environments including controllable vacuum ($<10^{-10}$ to 10^{-3} Torr), ambient neutral gas conditions, electron, ion, and solar irradiation fluxes. The chamber is currently equipped with three electron guns, two ion guns, various photon sources, SEM, Auger spectroscopy, and a flood gun neutralization source (Chang *et al.*, 1998; Dennison *et al.*, 2003b; Thomson, 2004). For UHV measurements, the chamber is pumped using turbomolecular, magnetic ion, and titanium sublimation pumps to base pressures typically $<10^{-9}$ Torr. The sample stage holds 11 samples that can be positioned in front of various sources, and is detachable for rapid sample throughput.

The primary detector for electron emission studies is a custom hemispherical grid-retarding field analyzer (HGRFA) that fully encloses the sample under study, as depicted in FIG. 3.1 (Chang *et al.*, 2000a; Nickles *et al.*, 2001). The hemispherical detector features an aperture for incident electron/ion admission and a fully-encased hemispherical collector for full capture of emitted electrons with a retarding-field analyzer grid system for emitted-electron energy discrimination. The hemispherical grid detection system, shown in FIG. 3.1, has been carefully
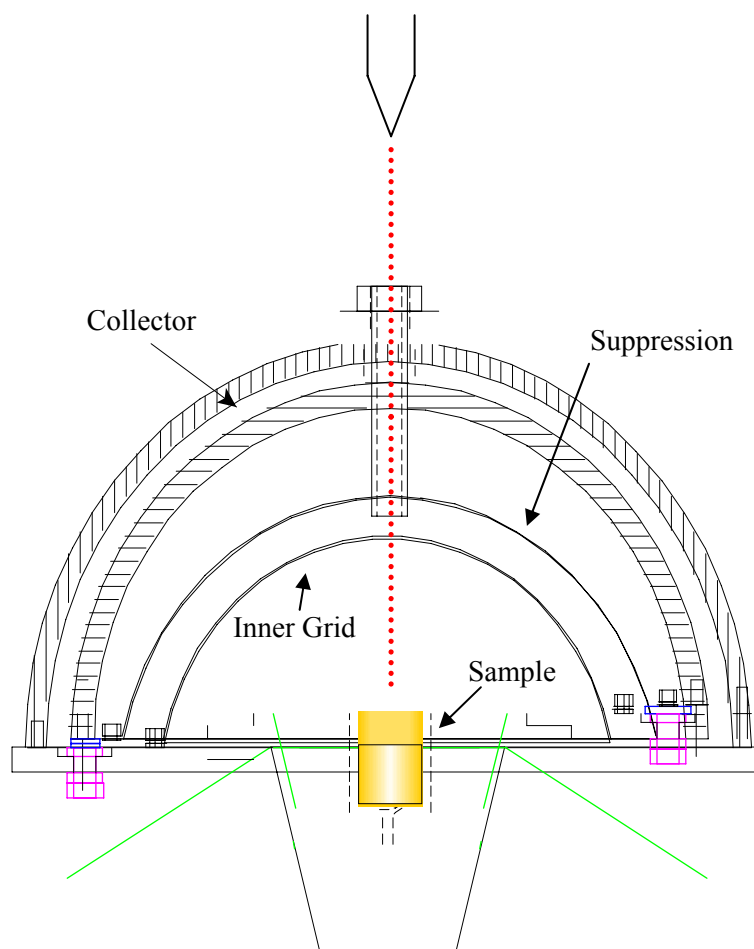
FIG. 3.1. Simplified cross-section of HGRFA.
Cross section diagram for original electron emission detector. Here the inner grid is tied to ground.

calibrated (both through calculation and measurement) to account for detector losses, allowing

yield accuracies with systematic errors <5% (Thomson, 2004). A simplified schematic diagram of

the HGRFA is show in FIG. 3.2. The incident electron (or ion) beam enters into the detector

assembly through a tubular aperture in the back of the detector housing. A suppression grid

within the detector is used to discriminate between BSE's (energies >50 eV) and SE's (energies

<50 eV), by applying a 0 V or -50 V bias. By ramping the grid bias, energy spectra of the emitted

electrons can also be measured using this detector with an energy resolution of 0.4±0.1 eV,
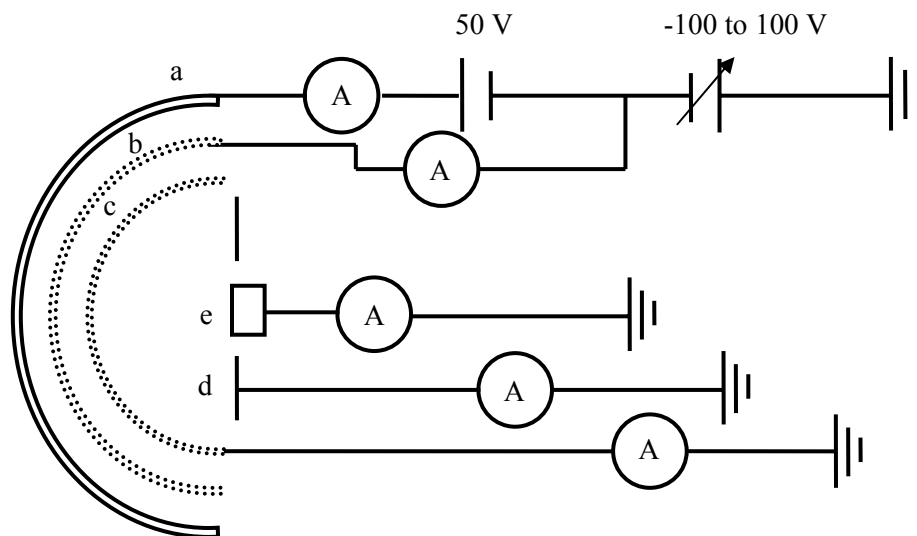
FIG. 3.2. Schematic of HGRFA.
(a) Solid hemispherical collector held at +50 V to attract all electrons that penetrate the bias grid.
(b) Bias grid used to discriminate electron energies coming from within. (c) Inner grid used to provide a uniform electric field and shield from unwanted edge effects. (d) Sample stage comprises the hemispherical and sample mounting platform. (e) The sample is held in the center of hemisphere.

limited by non uniformities in the suppression grid (Nickles *et al.*, 2001). Potentials on the suppression grid are controlled using a Keithley 230 voltage supply controlled via GPIB interfacing by a computer for both DC and pulsed-yield measurements.

Photos showing some of the elements of the analysis chamber are shown in FIG. 3.3 The photo in FIG. 3.3a is the vacuum chamber. The HGRFA and the sample carousel are shown in FIG. 3.3b-c respectively. The sample carousel is designed to hold 11 samples for rapid sample throughput. The carousel and HGRFA are shown mounted in the analysis chamber in FIG. 3.3d-e.

The full capabilities of the analysis are not discussed in the body of this thesis as they are not relevant to the work contained herein, but may be of interest to the reader (Dennison *et al.*, 2004).

3.1 DC Measurements

A DC method with a continuous, low-current beam of electrons is used to measure electron emission and electron yield from conducting samples. Charge added to or removed from a conductor, via electron emission, can be rapidly replaced by connecting the sample to ground (Bruining and De Boer, 1938; Baroody, 1950). The fully encased hemispherical grid retarding field detector, shown in FIG. 3.1, facilitates high accuracy measurements of absolute yields, with accuracy on the order of ±2% for conducting samples. It also allows the application of bias to each of the discrete elements of the detector. These biases allow for the discrimination of secondary and backscatter electrons and measurement of electron emission spectra. Also, the individually biased elements of the detector allow for extensive instrument characterization.

This section is devoted to the validation of the HGRFA in its new configuration. In previous studies, the inner grid (FIG. 3.2c) was electrically tied to the stage and was meant to provide a uniform electric field between the sample and the bias grid. This caused two problems: first, the current from the inner grid could not be measured independently from the stage and second, the inner grid could not be biased without biasing the entire stage. This becomes a problem when the sample adopts a potential and the inner grid begins to act like a discriminating grid.

The first test to be discussed is confirming the basic function of the HGRFA by taking the DC yield on Au. We then move to a more complex measurement of the DC emission spectra of Au. With the successful completion of these tests, we are able to validate the newly isolated inner grid by taking the emission spectra of an externally biased Au sample to test this new capability. The biased Au sample acts as a controlled surrogate for more difficult measurements on charged insulators. A permanent Au SEE standard has recently been added to a new surface voltage probe integrated within the HGRFA (Hodges, 2010).

FIG. 3.3. Photos of analysis chamber.
(a) Costello UHV surface analysis chamber. (b) *In situ* hemispherical grid retarding field analyzer. (c) Sample carousel removed from the chamber and setting vertical for sample replacement. (d) Sample carousel mounted in the chamber with HGRFA attached. (e) Another view of sample carousel and HGRFA mounted in chamber.

3.1.1 DC Yield

A thorough discussion of the DC system and methods is given in Thomson. This measurement technique has been thoroughly discussed in the literature (Chang *et al.*, 2000a; Nickles *et al.*, 2001). Where our system stands out is the use of the fully enclosed hemispherical detector and the detailed calibration of the instrument. By using this method we are able to measure the total and backscatter electrons directly rather than the more typical method of measuring a biased sample current. Our method not only improves accuracy it allows us to measure absolute yields with very high accuracy that is not possible using other methods.

For electron yield measurements on conductors, a continuous incident beam is directed on the sample and the currents on the detector (FIG. 3.2a), suppression grid (FIG. 3.2b), inner-grid (FIG. 3.2c), sample (FIG. 3.2d) and stage (FIG. 3.2e) are measured using electrometers designed by Dennison *et al.* (2002). A 50 V bias, relative to the suppression grid, is maintained at all times on the detector to insure that all electrons that are able to penetrate the grids are then collected. Grounding the grids through the electrometer facilitates the measurement of the total yield by allowing all emitted electrons to be collected. A -50 V bias relative to the sample is then applied to the suppression grid allowing only the BSE with energies >50 eV to reach the detector, thus determining the BSE yield. The secondary yield is calculated as the difference between the BSE and the SE yields. A representative yield curve for polycrystalline gold is shown in FIG. 2.2.

The yield of Au is presented to verify the accuracy and basic functionality of the system and to show that these data fall within the error bars of ±10% for the data available in the literature (Nickles *et al.*, 2001). It also serves as a springboard for more complex measurements.

3.1.2 DC SE Emission Spectra

From a theoretical physics perspective, the difference between a SE's and BSE's is the origin of the electrons. BSE's are electrons originating in the incident beam while the SE's are those that originate from within the material (Davies, 1996; Kite, 2007). In practice from an

applied physics perspective and when reporting electron yields in the literature, there exists an arbitrary 50 eV division to distinguish secondary electrons for backscatter electrons. This division is only valid for incident electron energies >50 eV. This demarcation has no basis in physics and is set merely as a convenience. Work done by Kite discusses a more accurate way of determining secondary electrons (Kite, 2007). However, for the purposes of this work, electrons with energies greater the 50 eV are labeled BSE and those less than 50 eV, are labeled SE.

Within these confines, there is an energy spectrum at which the SE's and BSE's are emitted. For most materials the energy spectrum for SE's peak at ~2 eV. For BSE's the peak is centered at that primary electron energy. These spectra can be measured using the same hemispherical detector described in Section 3.1.

A typical electron emission spectrum for Au is shown in FIG. 2.4a. The peak centered at ~2 eV is the secondary electron peak and the peak around 80 eV is the backscatter peak as the incident beam was 85±5 eV. This can be directly compared to the extensive angle resolved emission spectra of polycrystalline Au measured by Kite (2007). There are other features in these data, such as the quasi-elastic peak preceding the BSE peak, but for the purposes of this work, we need only note the gross features. These data were collected by biasing the suppression grid from 0-100 V in 0.5 V increments while measuring the current on the collector and taking the numerical derivative with respect to energy (dN/dE). It should be noted that the Staib election gun controller only has limited display resolution for incident energy. It can only display energies accurate to tens of eV's. If the display is reading 80 eV, the actual energy could be anywhere between 80 and 89 eV. The elastically scattered BSE peak should be the measure of what the incident energy is.

The data shown in FIG. 2.4a are consistent both with data taken previously on this system by Thomson and the extensive work done on Au by Kite (2007; Thomson, 2004).

3.1.3 Biased Spectra

Under a continuous-source electron beam, an insulator quickly charges to steady state, and the sample surface potential goes either positive (for energies between E_1 and E_2) or negative (for energies below E_1 or above E_2). These sample potentials can have considerable effects on SE escape kinetic energies as measured by the SE emission spectra. Typically a material with 0 V surface potential displays a SE emission peak near 2 eV (see, for example, Figs. 3.5a i and 3.5b i). However, if the sample potential becomes negative, the surface potential barrier will be lowered, and a repulsive electric field will accelerate escaping SE's away from the sample surface. This effect is illustrated in FIG. 3.4a ii and FIG. 3.4b ii.

In addition to the typical information that can be gleaned from measuring the SE emission spectrum, measuring shifts associated with the DC SE spectral emission peak provides an indirect technique for determining the sample surface potential induced by a continuous-source electron beam (Abbott and Dennison, 2005). A negative surface potential will increase the energy of escaping SE's and can be observed in the SE spectra by a right-shifting of the SE emission peak to higher energies (Girard *et al.*, 1992; Nickles *et al.*, 1998; Jbara *et al.*, 2001; Mizuhara *et al.*, 2002). Alternatively, if the sample surface is positive, the surface potential barrier will increase and inhibit lower energy SE's from escaping the sample surface as illustrated in FIG. 3.4a iii and FIG. 3.4b iii. In this case, an external positive potential must be applied, for example, by a surrounding grid to pull the full distribution of SE's away from the attracting surface potential of the sample. Hence, for positive surface potentials, a typical SE spectrum will show an SE peak left-shifted to apparent negative kinetic energies.

Previous studies in the analysis chamber have not had the ability to apply this external positive potential owing to the fact that the inner grid in the hemispherical detector was tied directly to ground. Positive potential manifests as a suppression of dN/dE if no external field is

(a) Normal Emission

| (i) $V_{bias} = 0$ V | (ii) $V_{bias} < 0$ V | (iii)   .$V_{bias} > 0$ V |

(b) Non-Normal Emission

| (i) $V_{bias} = 0$ V | (ii) $V_{bias} < 0$ V | (iii) $V_{bias} > 0$ V |
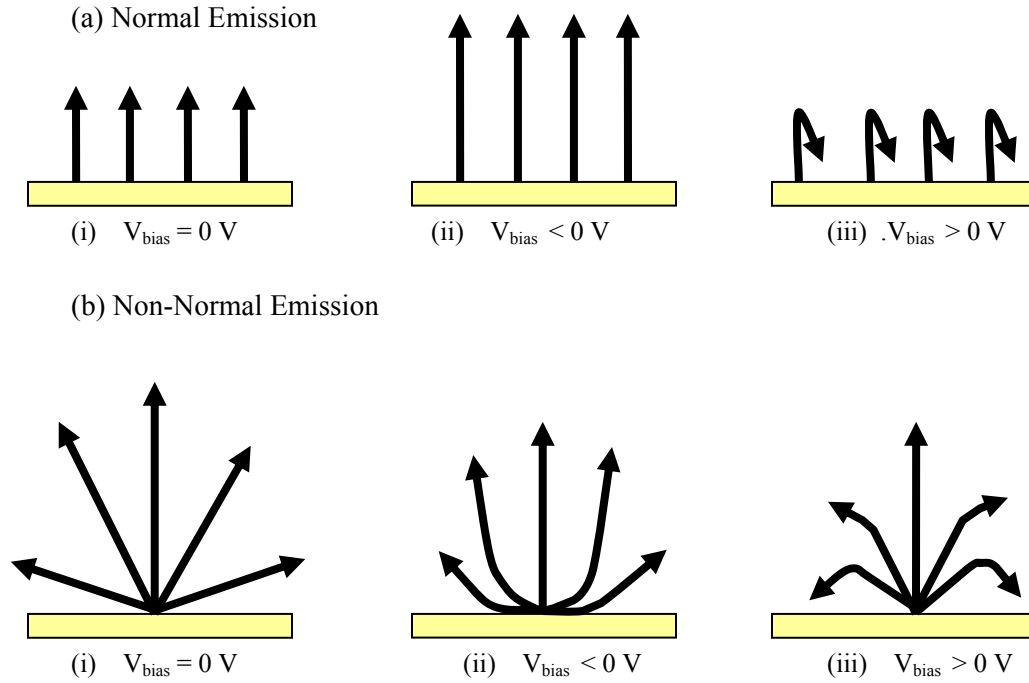
FIG. 3.4 The effect of surface voltage on SE emission.
(a) SE emission normal to the surface and (b) angular-dependant SE emission for: (left) no bias, (center) negative bias, (right) positive bias.

applied, but it is not possible to quantify the magnitude of the surface potential from this. For this reason the detector was modified to allow the inner grid to float to ~±600 V as shown in FIG. 3.2

In order to characterize the system in this new configuration, a series of spectra were taken on polycrystalline Au with several biases placed on the sample and inner grid. For reasons of time only brief analysis of the basic capability is discussed here, but there exists a large body of spectral data that has not been analyzed that could provide a wealth of information about the instrument and its capabilities.

To verify that the basic ability of the system to measure unbiased emission spectra has not been compromised by system modifications described in this thesis, several spectra were taken for Au as shown in FIG. 3.5a. These spectra were taken with incident energies 58±2 eV, 79±2 eV and 90±2 eV, from bottom to top respectively. There are no external biases applied to
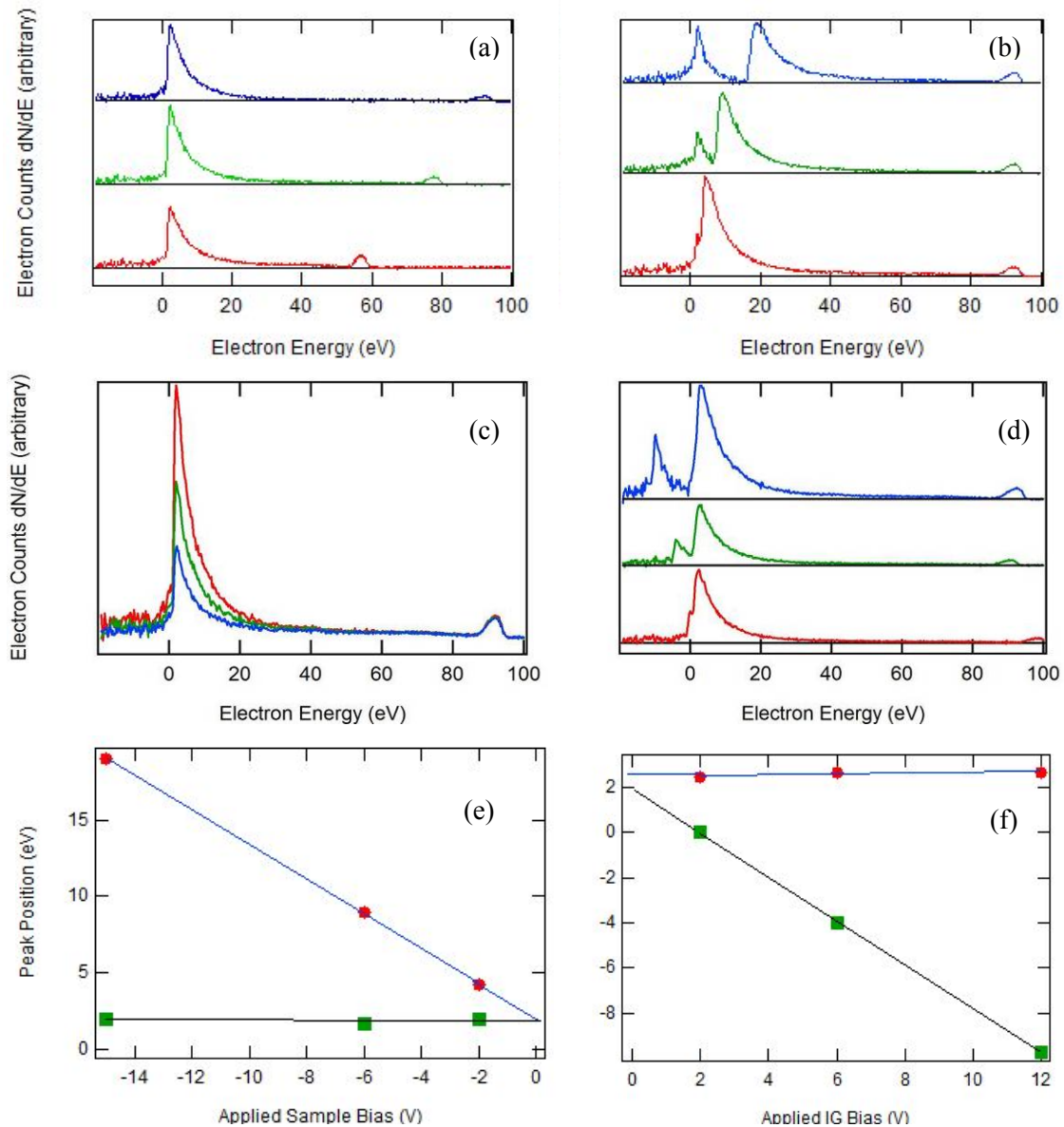
FIG. 3.5. SE emission spectrum taken on Au with bias placed on sample and inner grid (IG). (a) Zero bias on any element, taken ascending at 58 eV, 79 eV and 90 eV incident beam energy respectively from bottom to top, as seen in the backscatter peak. (b) 93 eV incident electrons; (bottom red) -2 V applied sample bias, (mid green) -6 V applied sample bias, (top blue) -15 V applied sample bias. (c) 93 eV incident electrons; the peaks tallest to shortest have a 2 V, 6 V and 12 V applied sample bias respectively. (d) 93 eV incident electrons; (bottom red) 2 V applied IG bias, (mid green) 6 V applied IG bias, (top blue) 12 V applied IG bias. (e) Red circle shows sample peak position as sample is biased and have a linear fit with a slope of -1.06±0.09 eV/V. Green squares shows IG peak position as sample is biased with a linear fit with a slope of 0.00±0.03 eV/V. (f) Red circle shows sample peak position with a slope of 0.00±0.03 as IG is biased and green square shows IG peak position with a slope of 1.02±0.06 eV/V.

the sample or any of the surrounding elements. Notice that the large SE peak centered at ~2 eV does not change in shape or magnitude despite the change in incident electron energy. The backscatter electron peak can be seen shifting to higher energy as the incident electrons increase in energy. This is consistent with work done by and cited in Thomson and many other spectra taken on this system before the upgrades detailed in this thesis. This confirms that no significant changes have been made to the basic function of the detector.

The next issue to investigate is the detector's ability to measure negative surface potential by measuring the right-shifting of the SE peak as the potential increases. These data can be seen in FIG. 3.5b; from bottom to top the sample had -2 V, -6 V, -15 V, respectively, applied. All these data where taken at a constant beam energy of ~93 eV as can be seen from the high-energy BSE peak. As negative bias is applied, there begins to emerge a peak centered at ~1 eV that does not move with sample bias. This peak is from the SE generated as BSE impact the inner grid. This peak is steady and does not move with sample potential; it can be used as a feudal mark from which to measure sample SE peak shifts.

In the case of a positive surface potential, our detector apparatus has had the inner grid (tied to the sample stage) between the sample and the suppression grid used to extract SE's from the positively charged sample (refer to FIG. 3.5c). Hence, an SE spectra influenced by a positively charged sample would appear to decrease in the magnitude (instead of shifting to the left) since only higher-energy electrons could escape the sample, pass through the inner grid and suppression grid, and arrive at the detector. This effect is seen in FIG. 3.5c where increasing positive potential was applied to the Au sample and, as predicted, the overall shape was unaltered, but the magnitude was suppressed.

The ultimate goal of this upgrade was to allow the inner grid to be biased and thus allow a full spectrum of SE's generated from the sample to reach the detector in the case of a positive sample bias. In FIG. 3.5d data are shown with the sample at 0 V and the inner grid held at several

positive biases. It can be seen that the SE peak from the sample is stationary and the other peak begins to shift to the left. This shows that this peak is indeed originating from the inner grid and that biasing can shift this peak to allow the measurement of a positive sample potential. The plots shown in FIG. 3.5e-f show the sample peak position of both the sample peak and the inner grid peak to verify that they are independent and that the peak position is linearly related to the potential of the respective elements. The red dots in FIG. 3.5e shows sample peak position as sample is biased and has a linear fit with a slope of -1.06±0.09 eV/V. The green squares shows IG peak position as sample is biased with a fit slope of 0.00±0.03 eV/V. In FIG. 3.5f the red circle show sample peak position with a slope of 0.00±0.03 as IG is biased and green square shows IG peak position with a slope of 1.02±0.06 eV/V.

At the time of this study, data have not been taken with both the sample and inner grid biased to a positive voltage. Future study should include extensive biased conductor studies that include positive sample and inner grid biases, as well as insulators that have been charged with an electron beam to both positive and negative potentials. With that being said, the work expressed in this section provides a basic verification of the functionality of the new detector configuration and some of its capabilities.

The conclusion that we can now draw is that measurement of sample peak position can yield information about the surface potential of the sample. Further we have confirmed that the IG peak is originating from the inner grid and that we can control the position of this peak to make possible the measurement of a positive sample potential.

3.2 Pulsed Measurements

The system at USU to measure electron emission from insulators uses the same fully encased hemispherical grid retarding field detector used in DC measurements, in concert with methods to control the deposition and neutralization of charge (Chang *et al.*, 2000c; Nickles *et al.*, 2001; Dennison *et al.*, 2003b; Thomson, 2004). Two electron sources provide electron energy

ranges from ~30 eV to ~20 keV and incident electron currents (1 to 500 nA or < 0.1 nA/cm^2 to 50

nA/cm^2 current densities) with pulsing capabilities ranging from 10 ns to continuous emission.

The low-energy Staib electron gun operates at incident electron energies of ~30 eV to 5000 eV

with a maximum beam current of ~ 100 nA and a <0.1 mm diameter minimum beam spot. The

high-energy Kimball electron gun operated at incident electron energies of 3.5 keV to 20 keV

with a typical beam current of ~ 20 nA and a 500 μm minimum diameter beam spot. The electron

flood gun used for charge neutralization can also provide a focused low-energy (1 eV to 200 eV)

source. Typically, charge deposition is minimized by using a low-current beam focused on a

sample area of ~2.3±0.2 mm^2 that is delivered in short pulses of ~5 μsec. The pulsed system uses

custom detection electronics with fast (1-2 μs rise time) sensitive/low noise (10^7 V/A / 100 pA

noise level) ammeters (Thomson, 2004).

Great pains have been taken during the course of this thesis to minimize overall system

noise to reach the capabilities listed above. Previous work done by Thomson was limited in the

energy range of the Staib gun (100 -5000 eV), as well as the lowest measurable beam current.

The work outlined in this thesis has allowed the lowest measurable incident pulse charge to go

from 1·10^6 electrons/mm^2 to 6·10^3 electrons/mm^2. A simplified approximation assumes an

isotropic distribution of electrons in the material from the surface to the penetration depth of

about a micron. For perspective, the electron density of 6·10^6 electrons/mm^3 that we are capable

of producing, can be compared to that of intrinsic silicon with a free carrier density of 6·10^9

electrons/mm^3. These efforts have included AC power filtering, increased cable shielding,

identification and removal of problematic noise sources, identification and removal of ground

loops.

Because surface charging is a function of incident flux density and not simply incident

fluence, a careful characterization has been performed on the primary electron source (the Staib

gun). By measuring the beam profile, and establishing controller settings for the full energy range

of the gun (20 eV to 5 keV), we ensure that the spot size (and consequently flux density) is consistent at 1.7±0.3 mm FWHM over the entire yield curve. This is a departure from the work previously performed on this instrument when spot size ranged from 0.3 to 1.5 mm in diameter.

3.2.1 Charge Neutralization

This section discusses the effectiveness of mounting the flood gun in the detector. It also details other methods of sample discharge, such as UV photon flooding and sample heating. Previous work in the analysis chamber has used the same flood gun as will be shown here, the difference being that in this work the flood gun is mounted in the detector housing rather than in sample block number one. The purpose of this upgrade was to allow charge neutralization of any sample positioned in the HGRFA.

To dissipate accumulated insulator charge, the pulsed-yield process is coupled with a low-energy electron neutralization source. The source, a flood gun, uses thermionic emission of low-energy electrons ((~3±1) eV from thermal spread) near the sample to dissipate positive near-surface charge. A sequence of events must take place in order for the flood gun to be effective. First, a low flux density, monoenergetic pulse is directed at the sample and the total yield is measured. The low-energy flood gun is then activated and allowed to flood the sample for 5 seconds. This is repeated with a -50 V bias on the discriminating grid so that only the BSE's can be measured, thus allowing the BSE yield to be determined. The entire sequence is then repeated typically for 15 pulses at a given energy to produce good statistics. After averaging, this produces one point on the total and BSE yield curves. This entire process is computer automated and controlled through a LabVIEW^{TM} interface. A complete timing diagram of the pulse yield system can be found in Thomson.

The thermionic electron neutralization techniques are only effective in a limited range of incident beam energies, namely those in the positive charging regime (σ>1). One way of dissipating negative potential is to irradiate the sample with higher energy electrons, at energies

between the crossover energies where the total electron yield is greater than one. However, this energy range is not well defined, varies from sample to sample, is dependent on sample charging, and is not even present for some materials. A more practical solution is to irradiate the sample with light to eject electrons via the photoelectric effect, thus causing the sample to adopt a smaller negative charge. UV sources with energies at a fraction of typical insulator direct band gaps (<10 eV) have been shown to be effective in discharging insulators such as Kapton^{TM} and polyethylene by stimulating photo-induces conductivity (Bass *et al.*, 1998; Osawa *et al.*, 2003), and the incident photon flux is not affected by sample potential. Levy *et al.*(1985) has reported discharging of deep distributions using a UV source of > 4 eV.

To neutralize charge near the surface of the insulator, an optical flood lamp needs to deliver low fluence (typically enough to produce 10^2 nC/mm^2 of photoemission) at visible/UV energies sufficient to exceed the work function threshold and induce photoemission (typically only a 1-10 eV to minimize penetration depth and secondary electron production and to prevent deep negative charging of the sample). The optimum flood lamp energy depends on both the sample material (work function) and charging level (electron affinity).

For this, a UV photon source has been developed to induce the photoelectric effect and dissipate negative charge build up between pulses. There are two sources mounted in the HGRFA. First is a UV diode with wavelength peaked at 350 nm and controlled externally. The second is UHV fiber optic through which we can introduce any energy photon available in the lab through a fiber optic feedthrough.

The photoelectric effect coupled with sample heating overnight via a heat lamp, serves to increase sample conductivity and facilitate the discharge of deep charging. Sample heating is effective due to the fact that material conductivity at room temperature (around 300 K) is proportional to $e^{-E/k_b T}$, where T is the temperature and k$_b$ is the Boltzmann constant. Therefore, a modest increase in the temperature from 300 K to 360 K can dramatically reduce the charge

decay time of a highly insulating material like Kapton from a few days to a few hours. This is an effective way to dissipate deep dielectric charging as is detailed in Section 3.2.1.1 and shown in FIG. 3.8c.

With both the inner grid and bias grid grounded through electrometers, the currents measured on each discrete element are collected and used to calculate the total yield using Eq. (2.1). With a -50 V bias on the bias grid, the data collected can be used to calculate the backscatter yield using Eq. (2.2). The currents measured by the electrometer are captured on a Tektronix oscilloscope and read into the controlling LabVIEW program. The pulses are then numerically integrated over the entire pulse (typically 0 μs to 5 μs) to get total incident charge in fC. Since measuring the SE yield is difficult to do directly, it is calculated by finding the difference in the total and BSE yields, σ and η. Once this is complete, both UV and electron flooding is turned on to neutralize the charge induced by the probe beam. A flow diagram is shown in FIG. 3.6. This sequence is then repeated no less than 15 times at each energy, so that good statistics can be used.

3.2.1.1 Flood Gun

The work done previously by Thomson shows that the above described system is sound and adequate for limited materials testing including conductors low-resistivity insulator and low-yield, high-resistivity insulators. In order to provide a more robust and versatile instrument with greater throughput, the flood gun has been moved from its position on a single sample block into the detector housing to provide flooding for any sample under investigation (Thomson, 2004).

The new flood gun uses the same basic design as was developed by Thomson, but was modified to be installed in a mount attached to the grounded hemisphere shielding the detector. The gun has a line of sight view of the sample via a small hole drilled in the detector that constitutes <1% of the detectors collecting surface. To neutralize charge very near the surface of the insulator, such a flood gun needs to deliver low currents (typically 10 nA) at low electron
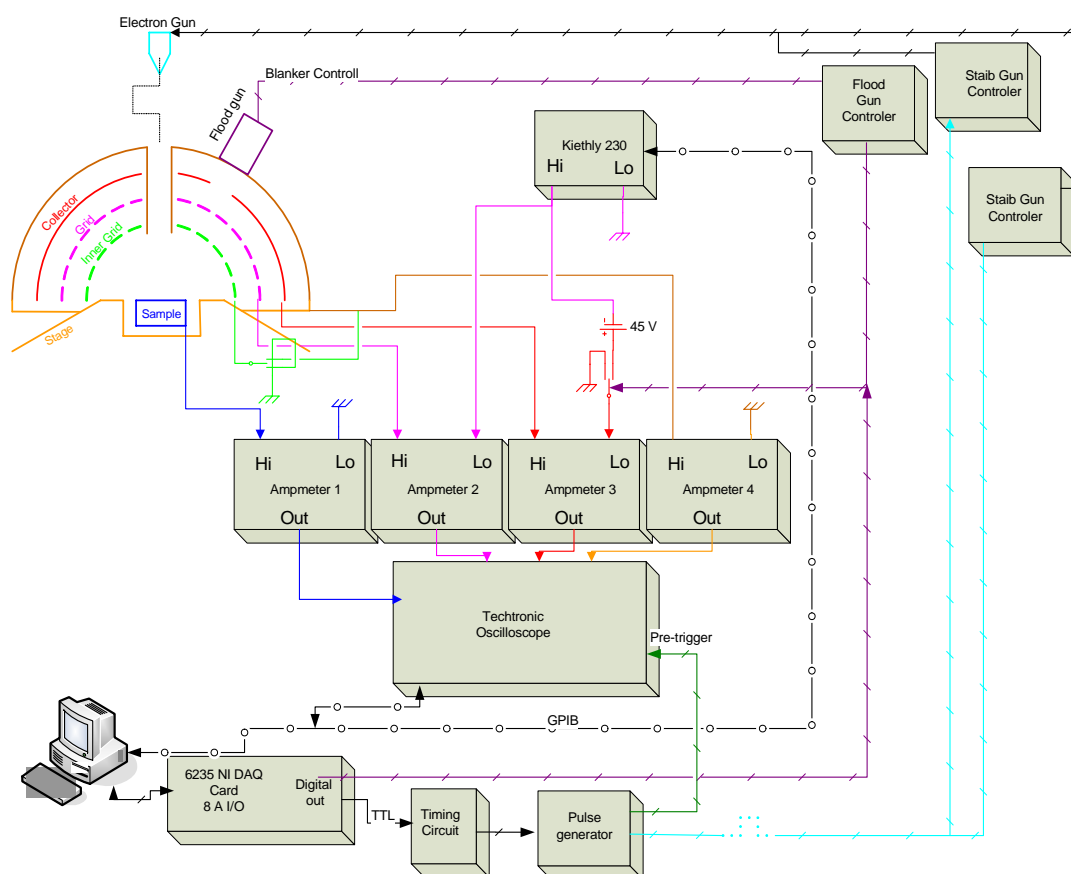
FIG. 3.6. Block diagram of the pulse yield system detailing signal flow.
Upgrades to the analysis chamber to suppress noise and enhance the systems ability to measure high-yield, high-resistivity materials, are shown.

landing energies (typically only a few eV to minimize penetration depth and secondary electron production and to prevent negative charging of the sample), extraction potentials were 2 V. The characterization of the flood gun is shown in FIG. 3.7. In FIG. 3.7a a positive voltage was placed on a conducting sample and the current was measured as the extraction potential was increased in the flood gun. In FIG. 3.7b the emission energy spectra of the flood gun was measured by stepping the suppression grid in 0.5 V increments. This was done for several extraction potentials and it can be seen that the emission peak and distribution do not change much as extraction potential is changed.
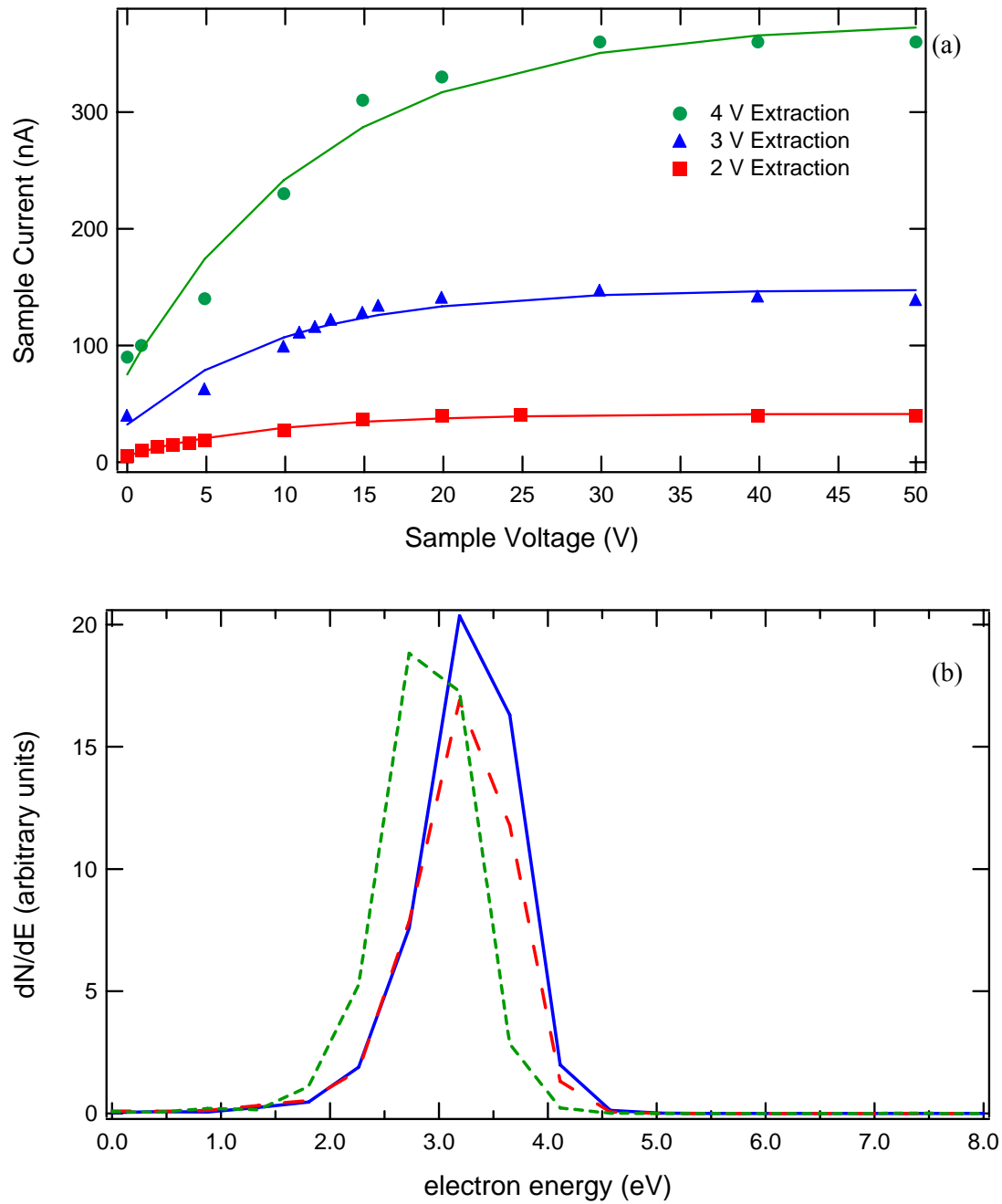
FIG. 3.7. Electron emission characterization of flood gun.
(a) Flood gun current to a biased Au sample. I_{Fil}=1.3 A for all data; only the gun extraction potential is varied from 4 V (●), 3 V (▲), and 2 V (■). Sample current ranges from 5.5 nA to 75 nA at a 0 V sample potential, and from 42 nA to 380 nA at saturation. (b) Flood gun emission spectra as measured by the collector. The suppression grid potential was stepped in 0.5 eV increments and the sample potential was kept at 0 V. I_{Fil}=1.3 A for all data; only the gun extraction potential is varied from 3.5 V (solid), 3 V (long dash), and 2.5 V (short dash).

The flood beam should be roughly uniform in charge density over the size of the charge region; however this is not critical due to an effective self-regulation of the positively charged insulator. The most positively charged regions of the sample will preferentially attract the most flood electrons; as the positive charge in these regions is dissipated they will attract less and less of the flood electrons. Electrons with kinetic energy less than the potential energy barrier of negatively charged surfaces will be fully repelled and will not reach the insulator surface at all. Thus, low-energy flooding will naturally develop a uniformly charged surface with a negative potential equal to the flood gun beam energy (to within the difference between the electron affinity of the insulator and the work function of the electron gun source or filament). Once charged to this potential, no more electrons will reach the surface. Given this self-regulation, it is practical to have the flood beam irradiate the full insulator surface. The flood aperture in the detector allows electron into the interior of the detector where they are attracted to the positively charged regions of the sample surface.

The effectiveness of this modification can be tested by using the pulse system to look for any modifications in the yield that would indicate that the material was retaining some charge after the discharge cycle. Of course, the material would have to be one that is of high resistivity and therefore especially susceptible to charging. The yield of a highly resistive material (Kapton) after multiple pulse discharge cycles to show that there is little change in the yield are shown in FIG. 3.8b. The same type of measurement except that the flood gun was not used to discharge the sample is shown in FIG. 3.8c. These two plots suggest that the flood gun is working and that positive sample charge can be removed in this way.

To determine the total incident flux impact on the sample, the current from all elements in the detector are summed. Since all the elements are carefully monitored and the efficiency of the detector is known, any excess charge in the system is a result of the incident pulse. To confirm this, the data shown in FIG. 3.8a provide a direct comparison of the summation and the
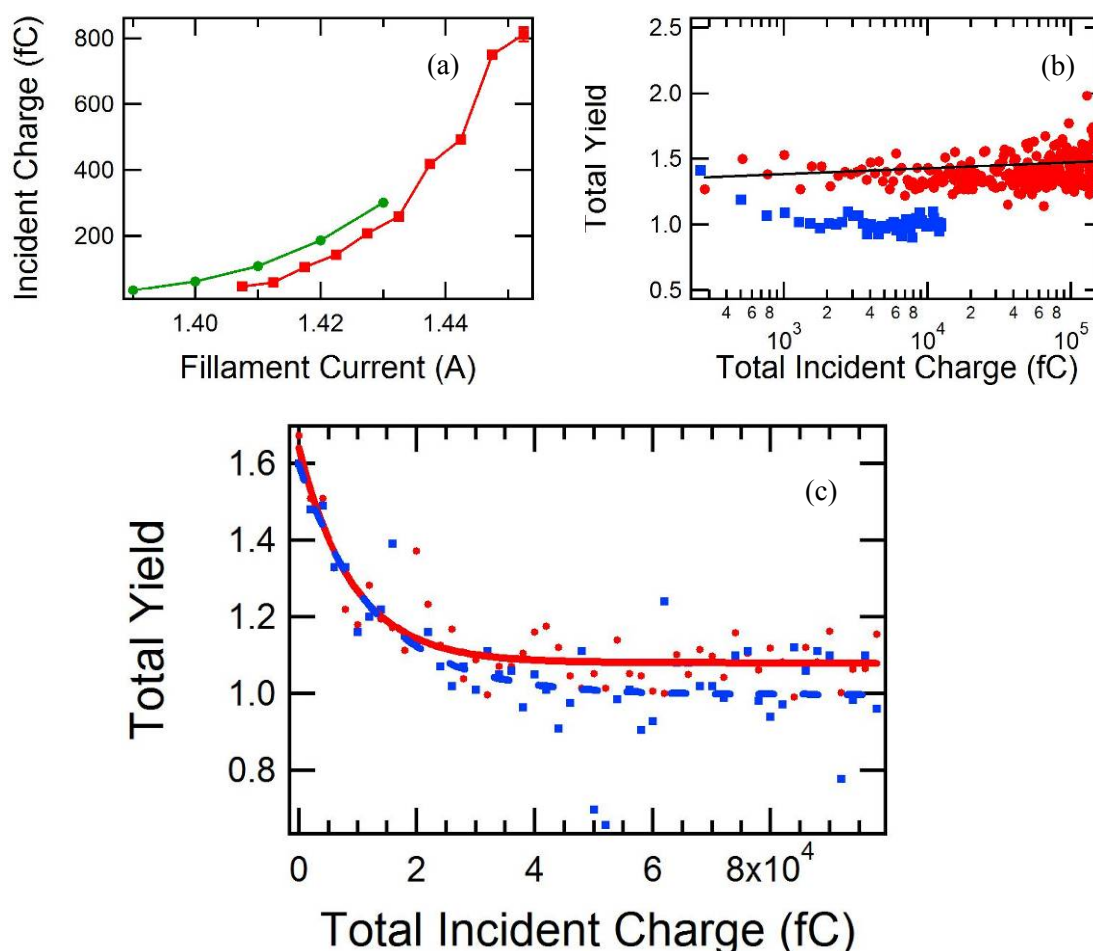
FIG. 3.8. Effectiveness of detector mounted flood gun and sample heating.
(a) These data are a comparison of the incident charge per pulse measured in the Faraday Cup (green circles) and by summation of all elements in the detector (red square) using a Kapton HN sample. Where the data overlap, there is a constant offset of ~50 fC. (b) Red circles indicate 500 pulse-flood cycles fit with a linear curve to show only modest instrumental drift (slope 0.5 ppm/fC). The blue data are taken without discharging between pulses. (c) Red circles show decay curve of 50 μm Kapton HN at 400 eV incident pulses. Note asymptote of 1.08 not 1.00 as expected. This is evidence of deep charging from past exposure. Blue squares are the same decay curve taken after the sample was heated with a heat lamp for 4 hr to ~50° C and allowed to cool.

incident pulse measured in a Faraday cup. This was accomplished by maintaining all gun settings

and keeping all but the filament current constant. This allows a measurement to be made on the

Faraday cup and then repeated in the detector. We have good agreement in the two methods with

a constant offset of 50 fC. This offset could be due to modest changes in the detector since its

efficiency was calculated in Thomson. This is an area that would warrant further study in the future and recalculation of detector efficiency outlined in Section 5.2.5.

3.2.1.2 Photon Flooding

Initial studies were conducted to determine the effectiveness of optical flooding at discharging negative charge build up (Thomson, 2004). A series of lamps including a mercury-gas, tungsten-filament, and UV LED array (385 nm) were mounted next to a quartz view port with a focusing lens to irradiate insulator samples inside the chamber (Otterstrom and Dennison, 2005). These had limited success at discharging the sample mainly due to the limited intensity and frequency range possible in this configuration. The primary objective of the upgrade described here was to add flood gun charge neutralization capabilities to any sample under investigation in the HGRFA. This required fabrication of a mount mentioned in Section 3.2.1, which had an added benefit that it was large enough to accommodate several other capabilities. This allowed the addition of the fiber optic cable and UV LED, both for the purpose of flooding the sample with UV light, inducing the photoelectric effect, and thereby neutralizing negative charge build up. A cross section of the HGRFA and neutralization mount can be seen in FIG. 3.9.

In our original configuration, photon neutralization could only be done by swinging the detector apparatus away from the samples, and then irradiating the samples with lamps through the vacuum chamber port window. This is not only extremely time consuming, and difficult to incorporate into an automated pulse/flood sequence, but it is very difficult to irradiate the same spot on the sample. In order to engage in viable studies of photo-discharging, the installation of light sources into the detector housing was needed. To accomplish this, the neutralization mount shown in FIG. 3.10 was designed.

Dual color blue/yellow or green/red LED's and a UV LED were mounted on the Cu detector mount. The LEDs are held in place by a collimating lens assembly (Ocean Optics Model 74 UVHT). These lens holders are made of anodized aluminum with a fused silica (SiO_2) lens
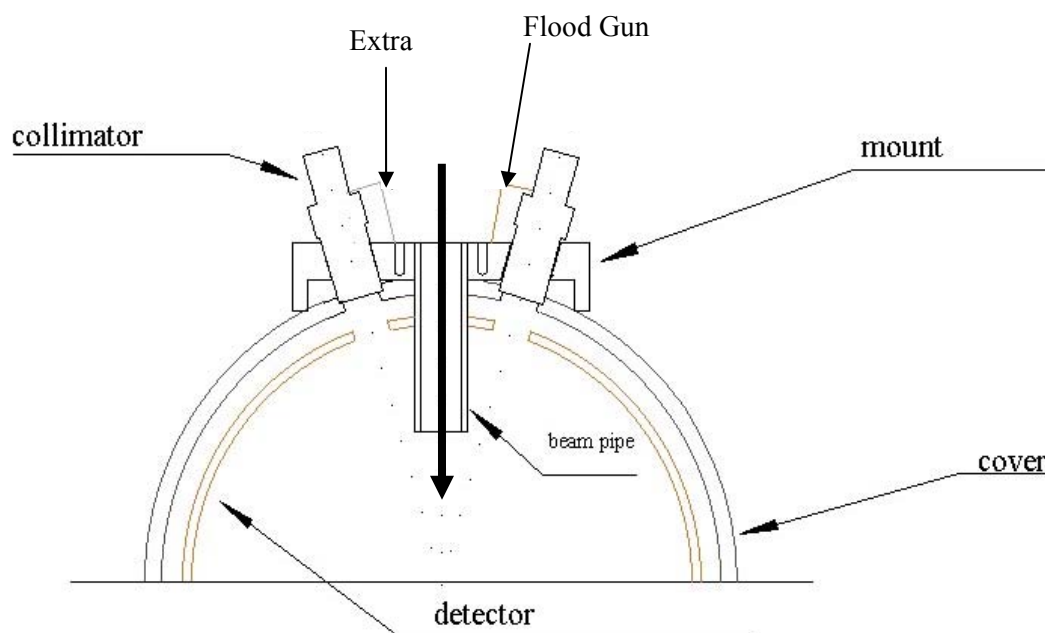
FIG. 3.9. Cross section of neutralization mount fixed to HGRFA.
Collimating lenses are shown in the foreground and the flood gun in the right rear. One lens is attached to a fiber optic cable and the other holds the UV LED. There is one more extra position for future use.

made to transmit UV light. They have a 3/8" external thread on one end and are threaded for an

SMA connector on the other end. The Cu detector mount is threaded to hold three of these lenses

and aim them at the sample. The piece that the SMA connects to is held in place by a set screw

and can be removed.

All three lens holders have a common problem. They need to be in line of sight with the

sample and are therefore exposed to emitted electrons from the sample. The lenses are insulators

and will charge up and distort the data. Two approaches to eliminate this problem were

considered. The first was to stop the electrons, but still let the light through. This would require a

transparent conductor such as indium tin oxide (ITO). While the electrical properties of the ITO

were acceptable, it will not transmit UV light, thus making it unsuitable for our application. The
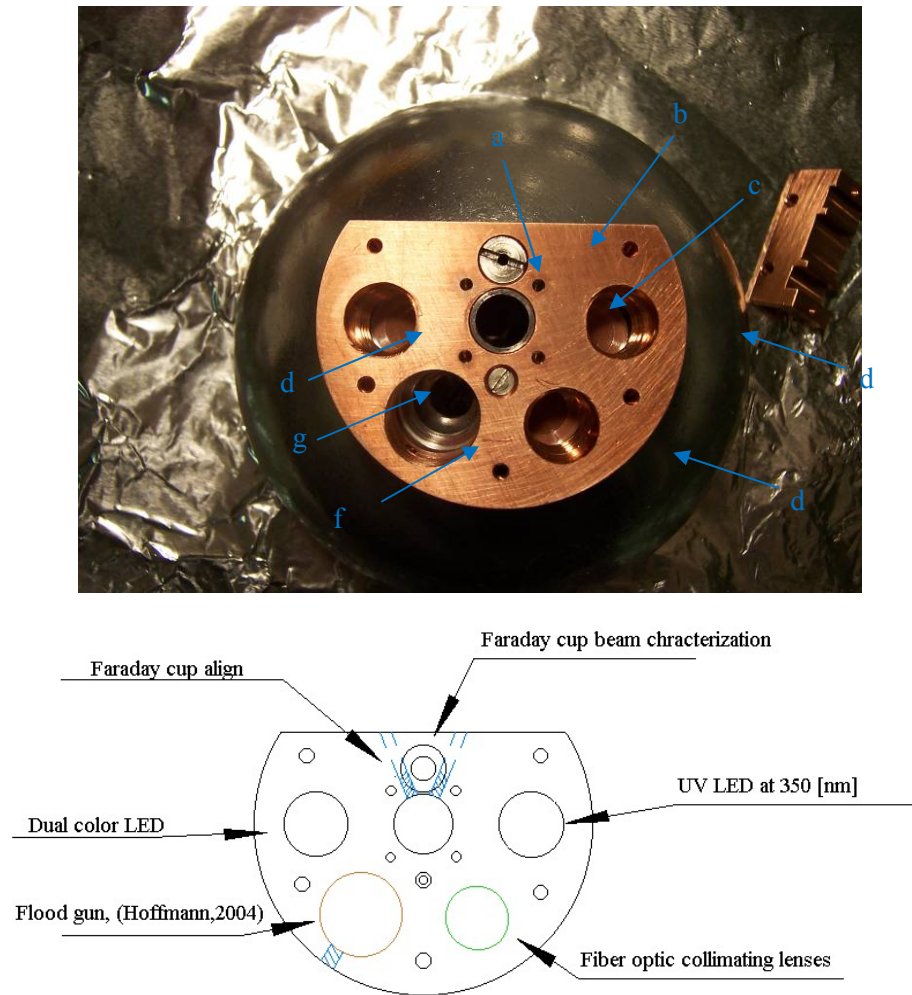
FIG. 3.10. Details of neutralization mount.
(a) Four Faraday cups (1.5 mm dia., 5.1 mm deep, 3.4:1 depth-to-diameter ratio) machined in the Cu mount on a 13.7 mm diameter bolt circle for beam alignment. (b) Faraday cup has been installed in the upper of the two screws for beam characterization. (c) 7 mm ID beam pipe. (d) threaded mounting holes for Ocean Optics collimating lenses. (e) Mounting hole for low energy electron flood gun. (f) 2-56 bolt ring for lead strain relief and future modification.

other approach was to allow the electrons to charge the lenses and shield the charge-induced electric field from the detector area. The shielding is accomplished with a high transmission copper mesh used in electron microscopy (Ladd Research, Part No. 10415SP; 150 lines per inch, 130 μm hole diameter, 37 μm wire diameter, ~75% transmission). This mesh was cut with a hole punch to fit in the holes in the Cu detector mount and held in place by the lens holders when they

were screwed in place. The mesh screens stayed in place very well, even when the lenses holders were removed, nevertheless care should be taken.

An ultra high vacuum compatible fiber optic for piping light from exterior sources into the vacuum system is attached to the third lens holder on the Cu detector mount. A custom made UV transmission, UHV compatible fiber bundle (~6 x 250 μm bare fibers bundled in a Teflon tube for wear resistance) 1 m long is attached to the lens holder and to a UHV compatible vacuum feedthrough (Ocean Optics, Model VFT-600-40) using standard SMA connectors and UHV compatible splice bushings (Ocean Optics, Model 21-02 SS). The exterior of the vacuum feedthrough is connected to various sources using a solarization resistant, high-UV transmission, 1 m long 600 μm diameter single fiber optic cable. The detailed emission and transmission characteristics of these source and fiber combinations has been measured in previous work detailed in Otterstrom and Dennsion (2005).

All of these measures have been installed and the basic operation has been confirmed. At the time of this paper, the validity of these upgrades as an effective method of discharging negative charge build up has not been investigated. This delay has been fortuitous because there now exists an instrument in the detector that is not discussed in this paper but is designed to measure surface potential directly (Dennison and Green, 2006c; Hodges, 2010). For this reason validation of the UV flooding has been outlined in Section 5.2.4 as future work to be done.

3.2.2 Other Detector Upgrades

A 7 mm ID beam tube is visible at the center of this Cu detector mount shown in FIG. 3.10c. This is a marked improvement from the 5 mm ID beam tube used in previous work. The larger tube makes centering of the sample much easier and more repeatable.

The Cu mount is held in place on the hemispherical shield by two machine screws visible in FIG. 3.10b immediately above and below the beam tube. A Faraday cup (referred to as the screw Faraday cup; 1.5 mm dia., 10.9 mm deep) is installed in the upper of these two screws.

This will allow fairly accurate determination of the beam current with minimum beam deflection and with an aspect ratio of 7.3 it will have an efficiency of 92%. Four smaller Faraday cups (1.5 mm dia., 5.1 mm deep, 3.4 aspect ratio) were machined in the detector housing on a 13.7 mm diameter bolt circled centered on the beam pipe. These are shown just outside the beam tube diameter in FIG. 3.10. Because of the small aspect ratio, these Faraday cups are only useful for beam alignment. These smaller cups make it possible to automate the beam centering process so that there is no incident flux on the sample before the yield is measured.

Five small tapped holes are visible at the outside diameter of the Cu detector mount; these are used to secure lead wires.

3.2.3 Dark Current Measurement

A timing block diagram of the pulsed-yield measurement setup is shown in FIG. 3.11. As can be seen in the figure, a digital TTL signal from the computer DAQ card was used to activate a timing circuit that delivers a trigger to the Tektronix 115 pulse generator. The pulse generator sends a square-wave pulse (typical pulse duration of 5 μs and 100 ns rise time) to one of the two electron guns that emit an electron-beam pulse with an amplitude ranging from 1-100 nA to the sample and to the oscilloscope. As with the DC setup, current signals from the collector, suppression grid, sample (sample displacement current for insulator samples), and stage were measured independently using sensitive ammeter circuitry. However, ammeters used for pulsed measurements were optically isolated, fast (1-10 μs rise time), and sensitive ($1 \cdot 10^8$ V/A to $2 \cdot 10^6$ V/A) with low internal noise (0.6-3 nA noise level). Generally, an ammeter amplification of $2 \cdot 10^7$ V/A (with a response time of ~1 μs) was used for signal processing. These signals were captured using a Tektronix TDS 2100 500 MHz digital storage oscilloscope with 1GS/s sampling rate. Details of the current measuring circuitry are provided in Zavyalov (2003). The response time of the electrometers and the electron gun ultimately define the shortest pulse the system is capable of measuring. Pulses from the Staib gun into a Faraday cup are shown in FIG. 3.12. Pulse widths

Computer
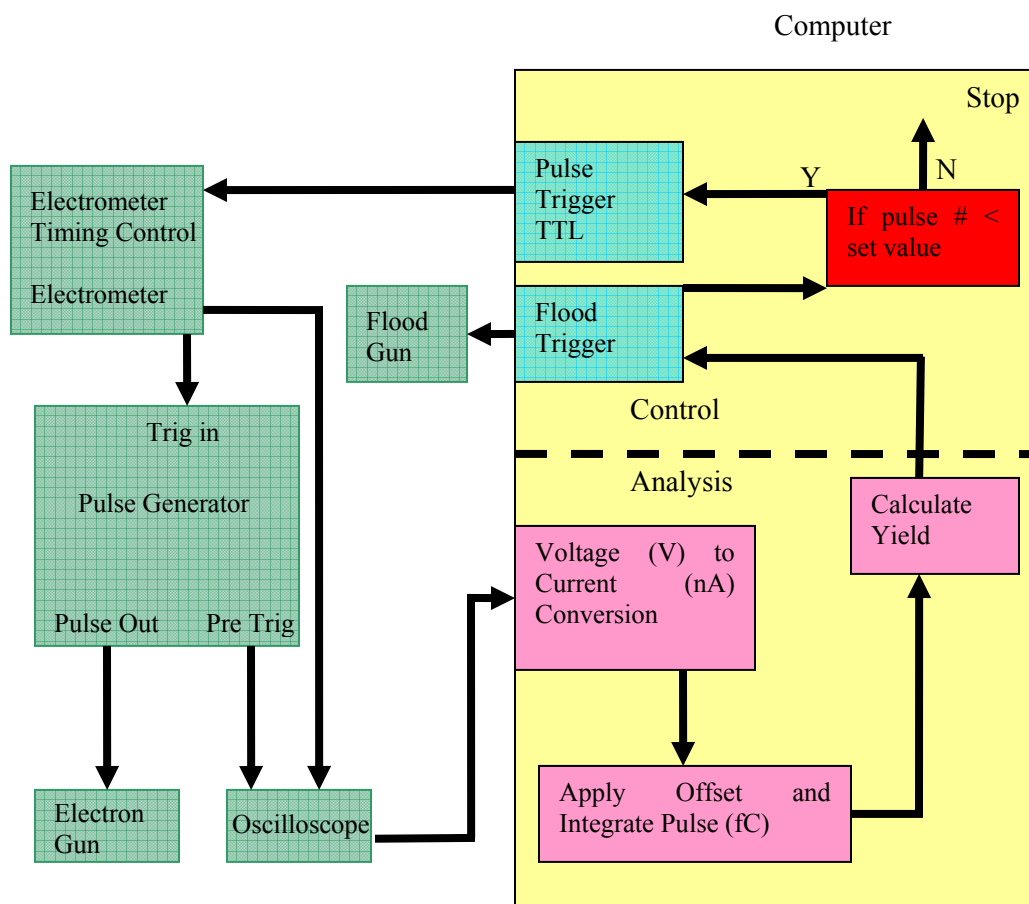
FIG. 3.11. Timing diagram of pulse yield system.
The sequence starts in the red box. For the first iteration the sequence is started by the user. For all subsequent iterations the sequence will repeat until the stop condition is met with a user defined value for the number of pulses.

supplied by the generator were 2 µs, 3 µs, 4 µs, 5 µs, 7 µs, and 10 µs duration square waves. As seen in FIG. 3.12, electron pulse profiles emitted from the gun were not square or symmetric in time. It might be possible to further push the sensitivity of the pulse yield system by calculating the yield point for point throughout the duration of pulse rather than integrating it to calculate the yield. This process will be outlined in Section 5.2.6 as an item of future work.

As with the DC setup, the pulsed-data acquisition and analysis setup was fully automated using LabVIEW™. In the pulsed system described by Thomson, two of the four measured currents (detector, sample, grid and stage) were measured using the integrator circuits detailed in
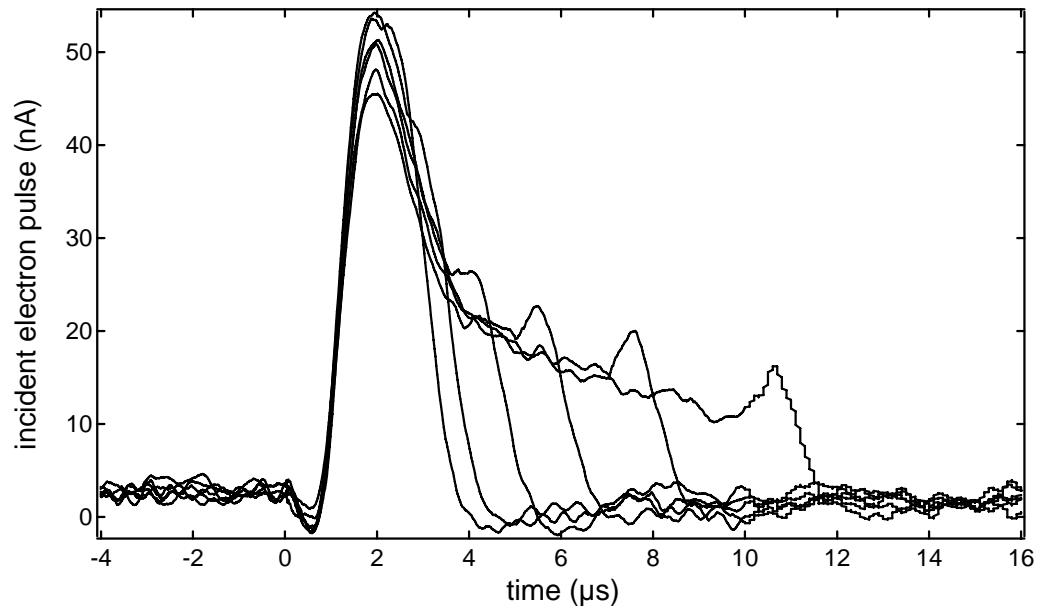
FIG. 3.12. Pulse profiles for the Staib gun at 1 keV as measured by the Faraday cup.
Similar profiles were seen in sample current profiles. Pulse widths supplied by the generator
were 2 μs, 3 μs, 4 μs, 5 μs, 7 μs, and 10 μs duration square waves. As seen in the figure, electron
pulse profiles emitted from the gun were not square or symmetric in time.

Zavyalov (2003). These circuits integrate the entire signal from beginning to end. If the signal is

clean before and after the pulse, this method is adequate. However, it was found that the two

signals measured by the integrators (grid and stage; particularly the stage) contain more noise

than the other two. This leads to inaccurate measurements of the yield. To overcome this, a four

channel Tektronix digital storage scope is used to measure all currents. LabVIEW then integrates

all the traces to calculate the total current from each element. In this way, only the current during

the pulse is measured. This is illustrated in FIG. 3.13a by the region between the shaded areas.

Although the data before and after the pulse (as seen in FIG. 3.13a) are not contributing

to the yield, they can be used to determine the dark current offset. This is accomplished in

LabVIEW by averaging all the data before (15 μs) and after (10 μs) the pulse and subtracting it
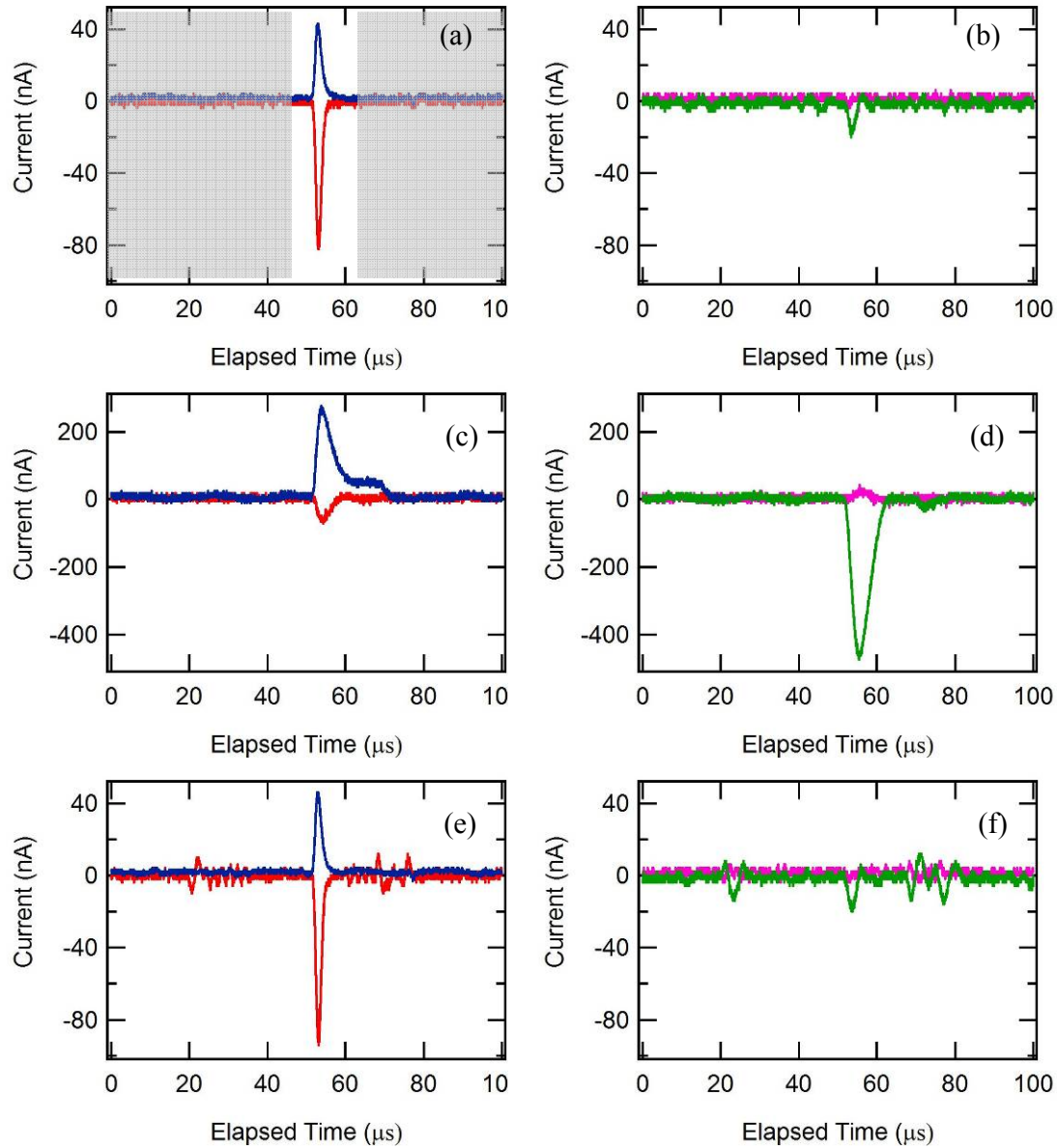
FIG. 3.13. Electron pulses measured on oscilloscope.
(a) Typical signal captured on Tektronix oscilloscope from Kapton HN measuring the total yield (i.e., with 0 V bias on grid). Blue data are measured from the sample, red are from the collector. (b) Data showing the grid and stage current during a pulse with 0 V bias on the grid (c) Shows collector and sample current during a pulse with -50 V on the bias grid. (d) Data showing the grid and stage current during a pulse with -50 V bias on the grid. Note the large stage signal to the stage due to SE being repelled from the grid. (e) Noisy signal from a total yield measurement from the sample and collector respectively. (f) Noisy signal from stage and grid. Note the relatively large peaks in the normally quiescent signal well before and well after the pulse, for example the peaks at ~20 μs and ~70 μs.

from the entire signal, illustrated by the shaded region in FIG. 3.13a. This effectively zeros the current signal for each pulse.

In addition to zeroing the signal and providing a more accurate calculation, these data are used as rejection criteria. Despite all the pains taken to minimize the noise in the system, there remains troublesome intermittent noise. This noise is not constant and effects only approximately one pulse in seven; but in that one pulse noise can significantly distort the signal (see FIG. 3.13f-e). For this reason there is a user defined threshold for the standard deviation of the pre- and post-pulse data. If the threshold is exceeded, the entire pulse is discarded. This threshold (typically set at value of $4 \cdot 10^{-13}$ C) is not constant from day to day, but seems to be adequate for one day's worth of data acquisition. Efforts have been made to eliminate this noise altogether, but they have all failed. There are some clues to its origin in the fact that it is largest in the stage current that shields the other elements (see FIG. 3.13f). Other detector elements register it as well, but appear to be inverted. This suggests capacitive coupling. Also the noise seems to get worse during the middle of the day and then better later on. This is roughly consistent with the buildings power consumption; it should be noted that the laboratory is near the buildings transformers and power relays. This is an unconfirmed hypothesis and needs further exploration, but for the time being rejecting bad data provides adequate capabilities.

3.2.4 Beam Characterization

Up to this point all the efforts to mitigate surface charging have focused on charge neutralization (electron and UV flooding) and incident beam flux minimization. However, charge accumulation is not a function of the flux (beam current), but the flux density (beam current per unit area). The work done previously has paid little regard to the spot size as beam current alone was assumed to be sufficiently low as to not induce a surface voltage of any significance. Given the data shown in Section 4.2.2.5, it is clear that the probe beam is capable of causing significant charging in some materials. For this reason it is necessary to normalize the spot size over the

entire energy spectrum of the gun so that the flux density would be the same if beam current was kept constant. This allows only the yield and resistivity to affect the surface potential from one beam energy to the next.

The beam profile was measured using a Faraday cup (FC) residing in the analysis chamber and mounted on a computer controlled translation stage with 0.7 μm resolution. Using translation and rotation the pulsing beam is centered in the FC using as little beam deflection as possible to limit beam distortion. Once centered, the FC is moved in 0.19 mm steps with the current from the pulse beam measured at every step. In the interest of time, the spatial resolution of this test was set at 0.19 mm; but for future studies, the resolution is limited only by that of the stage (0.7 μm), and the sensitivity of the FC current to small changes in position.

The FC is a circular aperture with a 5.5 mm diameter that is surrounded by a tertiary shield in the shape of a washer. The current on both elements is measured independently and the whole unit is mounted in the sample carousel that also has independent current monitoring. Using a small ~0.1 mm spot size, it is possible to profile the surface of the FC by scanning the beam across it as shown in FIG. 3.14.

Mapping the FC surface is an interesting and useful exercise to determine accuracy of this method. To determine the profile of the beam, we need to look at the FC current as the beam enters over the sharp lip of the FC. If the diameter of the beam is smaller than that of the FC then the method of beam characterization is straight forward. It is assumed that the beam has a Gaussian distribution and since the FC is bigger than the beam, we can approximate it as a step function. This allows the deconvolution of the two functions to be accomplished by fitting the measured FC current with a Gaussian. The FWHM of the fit is the diameter of the beam. These profiles and their fits are shown in FIG. 3.15 and FIG. 3.16. If the beam is larger than the FC, it is necessary to deconvolve the Gaussian beam with a circular aperture rather than the simple step
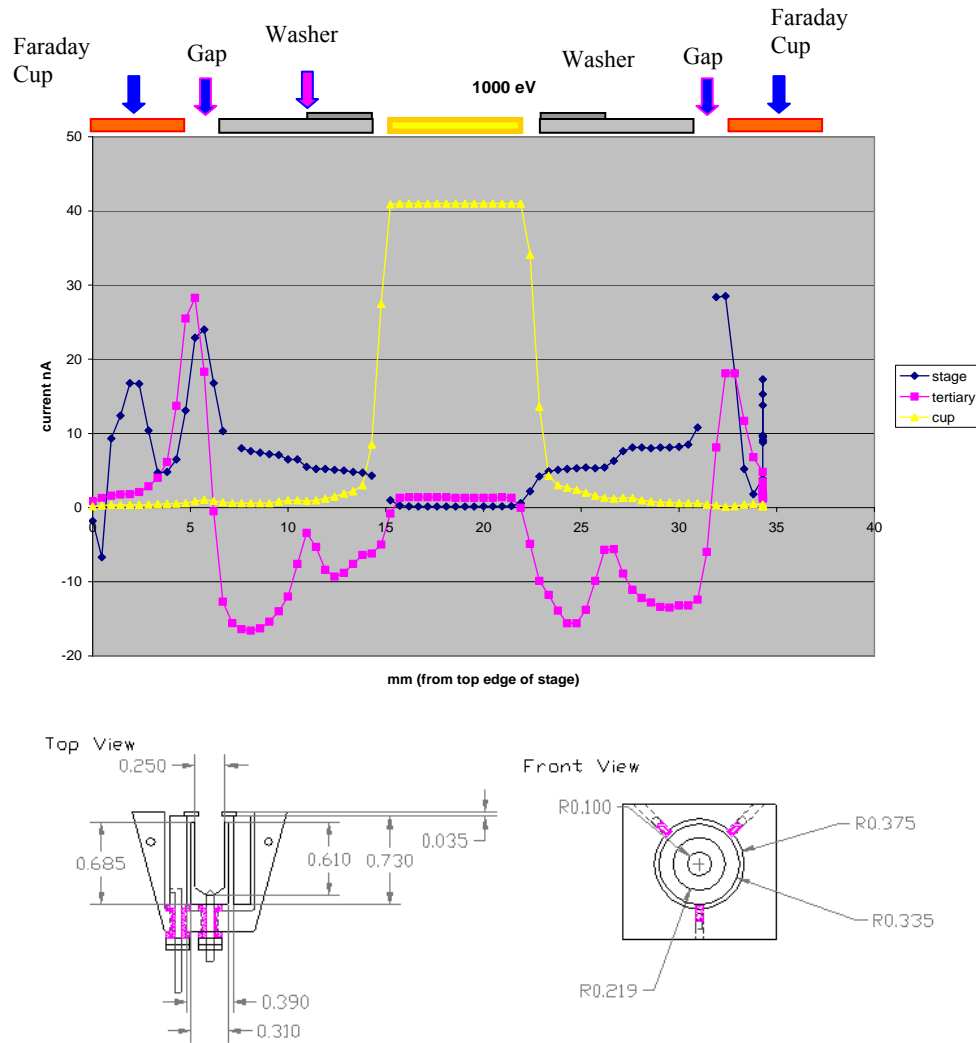
FIG. 3.14. Staib electron gun DC beam profile and Faraday cup.
The width of the electron beam and features of the Faraday cup are evident as the Faraday cup is translated past the electron beam.

function. For this study the beam was significantly smaller than the FC, so the simpler step function deconvolution is used here.

A complete series of profiles was taken at energies that span the range of the gun. By fitting each, the gun settings were found that provided a consistent pulsed spot diameter of 1.7±0.1 mm. 1.7 mm was chosen because that is the largest size obtainable at 5000 eV; at lower
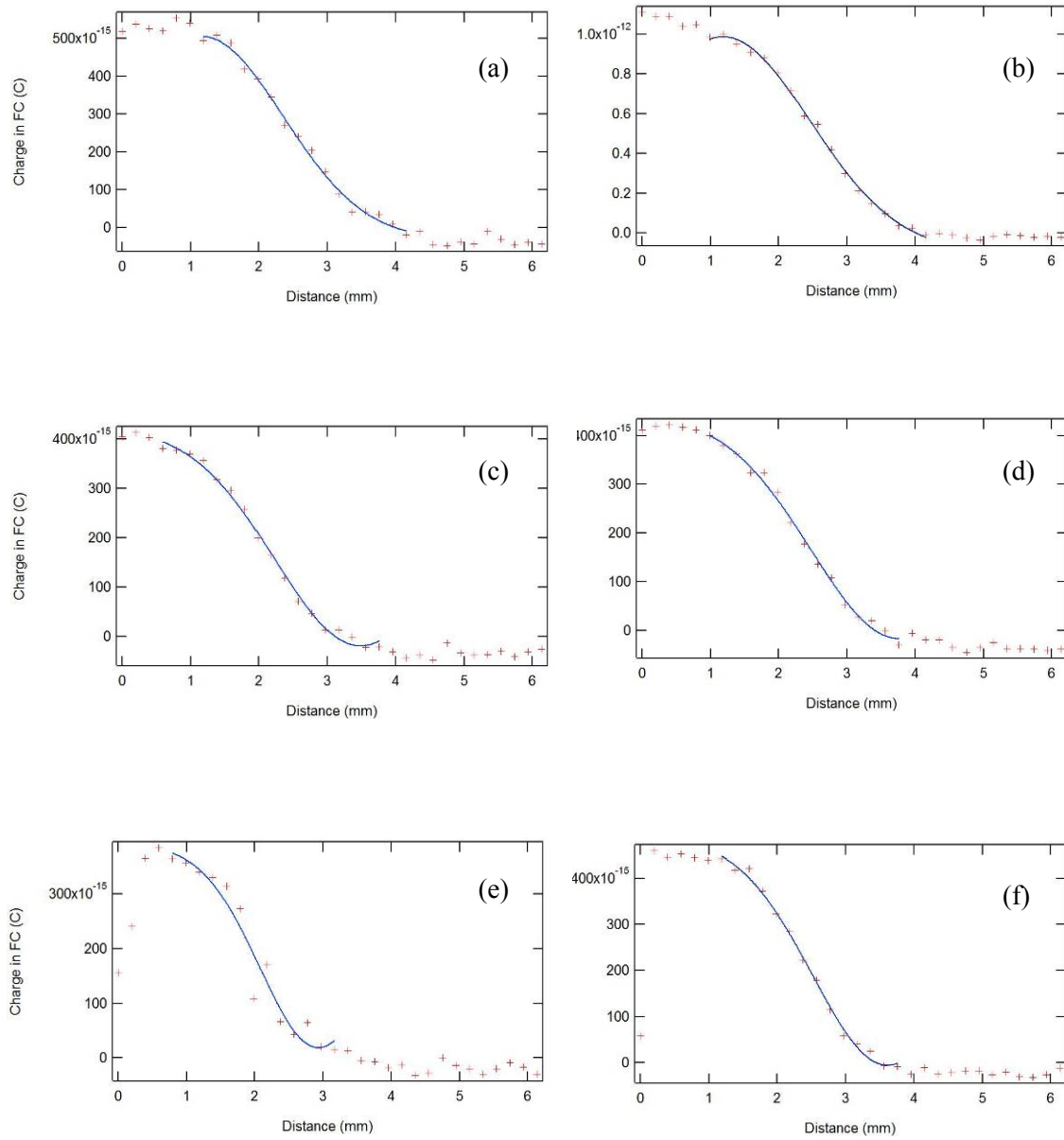
FIG. 3.15. Staib electron gun pulsed beam profiles
(a) Beam profile at 50 eV with grid setting of 1.74 and focus at 0.69. (b) Beam profile at 80 eV with grid setting of 1.75 and focus at 0.79. (c) Beam profile at 100 eV with grid setting of 2.21 and focus at 0.91. (d) Beam profile at 200 eV with grid setting of 2.37 and focus at 1.18. (e) Beam profile at 300 eV with grid setting of 2.41 and focus at 1.41. (f) Beam profile at 1000 eV with grid setting of 2.62 and focus at 1.57.
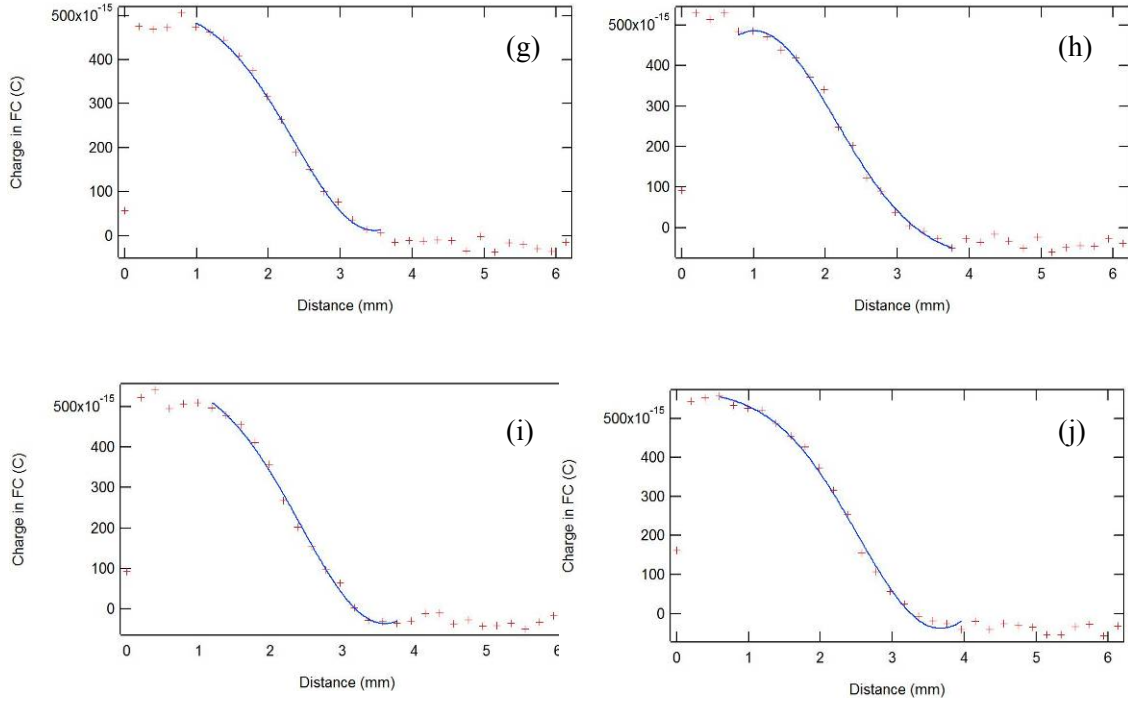
FIG. 3.16. Continued Staib electron gun pulsed beam profiles.
(g) Beam profile at 2000 eV with grid setting of 2.8 and focus at 1.9.(h) Beam profile at 3000 eV with grid setting of 2.93 and focus at 2.18. (i) Beam profile at 4000 eV with grid setting of 2.92 and focus at 2.3. (j) Beam profile at 5000 eV with grid setting of 2.89 and focus at 2.32.

energies, larger sizes are possible, but it will not be possible to normalize them over the full range of the Staib gun.

Because of the difficulty of these measurements it is not possible to measure a profile at every energy that might be of interest. It is assumed that the spot size has some consistent relation to the grid and focus settings on the gun. The red and green data FIG. 3.17 show the settings for the Staib gun at the normalized spot size of 1.7 mm. It was found that a double exponential, of the form

$$y(x) = y_o + A\exp(-bx) + C\exp(-dx),\tag{3.0}$$

fit the settings for the grid and focus. The fits are also shown in FIG. 3.17, with fitting parameters tabulated in TABLE 3.2. This fit provides settings for the gun at any desired energy
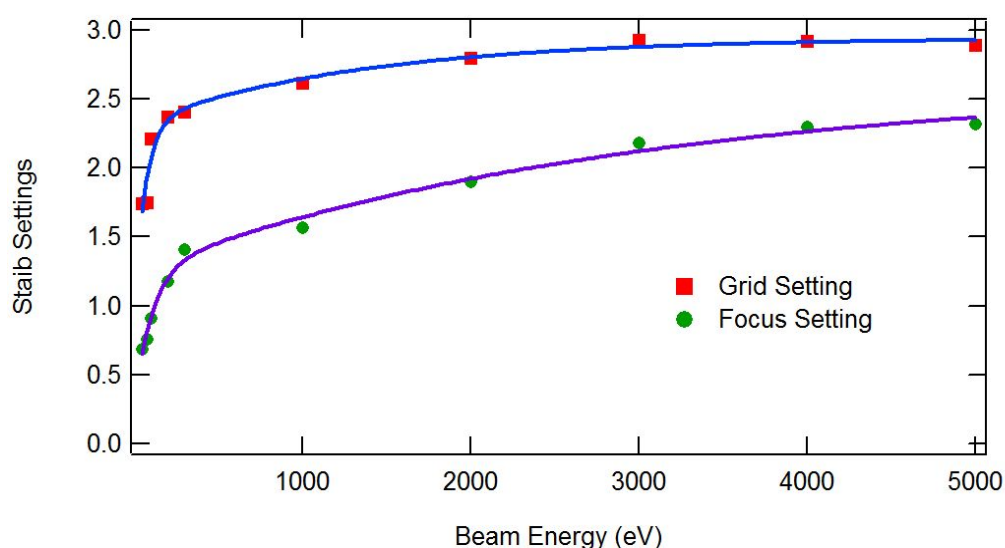
FIG. 3.17. Grid and focus settings for Staib electron gun.
The red data are the grid settings for the Staib gun at a spot size of 1.7 mm FWHM. These data are fit with a double exponential fitting function. The green data are the settings for the focus and are also fit with the same function.

to maintain the spot size at ~1.7 mm. It should be noted that the fit is not valid for energies less than 70 eV as there is insufficient data at the low end of the curve where the data are changing most dramatically.

The settings found in this section should be used with the Staib gun whenever surface charging is critical. This includes yield measurements, decay curves and charge accumulation measurements. All the data presented in Chapter 4 have been taken using the setting describe in this section. It should also be noted that these settings are only valid for the pulsed Staib gun. Other setting need to be use while using the gun in DC mode, but typically charging is of little concern while operating in this mode. Settings for the high-energy Kimball gun are also not included here and would need to be profiled in the same manner to provide a uniform spot size before an investigation could be conducted.

TABLE 3.1. Measured spot sizes and corresponding gun settings

Beam Energy (eV)	Grid Setting	Focus Setting	Spot Size FWHM (mm)
50	1.74	0.69	1.7±0.2
80	1.75	0.76	1.8±0.2
100	2.21	0.91	1.8±0.2
200	2.37	1.18	1.8±0.2
300	2.41	1.41	1.8±0.2
1000	2.62	1.57	1.6±0.2
2000	2.8	1.9	1.6±0.2
3000	2.92	2.18	1.6±0.2
4000	2.93	2.30	1.7±0.2
5000	2.89	2.32	1.6±0.2

TABLE 3.2. Fitting parameters for Staib gun grid and focus.

Fitting Parameter	Grid		Focus	
	Value	Error	Value	Error
y_o	2.9	0.1	2.6	0.3
A	-0.6	0.2	-1.4	0.2
b	0.0007	0.0006	0.0003	0.0002
C	-1.4	0.7	-1.0	0.2
d	0.02	0.01	0.010	0.005

CHAPTER 4

INSULATOR MEASUREMENTS

The instrument described up to this point has been characterized and validated. It is now possible to discuss yield measurements taken on progressively more charge susceptible insulators. Susceptibility to charging is a function of total yield and resistivity. The total yield defines how quickly a material will accumulate charge. Resistivity (both DC and RIC) defines how well charge is transported away from the surface, through the bulk of the material and to a grounded substrate. Therefore, to determine the effectiveness of the pulse yield system for measuring the minimally charged yield of an insulator, we consider a progression of more challenging materials. First we examine CP1, a material similar to Kapton HN that has a low total yield of (σ_{max}~1.4) and a relatively low conductivity (~10^{-19} (Ω-cm)$^{-1}$) (ManTech, 2010). With a resistivity in this range, the charge decay time will be several days and will therefore dissipate any charge build up in that time frame. Next, we investigate the polyimide Kapton HN (DuPont, 2010). This material has a slightly higher yield (σ_{max} ~2.2), and has low conductivity (~10^{-19} (Ω-cm)$^{-1}$), again leading to a decay time of several days. This material is a good test of our discharge methods and is representative of most of the materials of interest for space-based application. Finally, we consider polycrystalline aluminum oxide with a high yield (σ_{max} =~7) and low conductivity (~10^{-16} (Ω-cm)$^{-1}$) (Donegan *et al.*, 2010). This material accumulates charge quickly and retains it for tens of minutes. This material not only tests our discharge methods, but also our minimum probe pulse current and ultimately our noise floor.

The three materials presented in this chapter are shown in three subsections (Section 4.1-4.3). Because these subsections are of great interest to the spacecraft charging community as a whole, they have been written and formatted is such a way as to make them independent from the rest of this thesis and from each other. For this reason there will be considerable repeat information presented for each material. This can be tedious to a reader interested in this entire

document, but it will allow a more rapid and widespread dissemination of the information contained herein.

4.1 Low-Conductivity Low-Yield Material (CP1)

This material was part of a broader study, and is being explored as material for use as a solar sail by NASA JPL. The bulk density of LaRC™-CP1 is tabulated as (1.434 ± 0.02) 10^4 kg·m^{-3} by the manufacturer of these materials (ManTech, 2010). Much of the information contained in this section is repeated in a report generated by the MPG. The data presented there is of greater detail, so if there is information required about the material it is likely found in the full JPL report (Dennison *et al.*, 2006a).

4.1.1 Material Characterization

The SRS Technologies solar sail sample is a layered material comprised of ~2.5 ± 0.2 μm fluorinated polyimide with ~80 ± 10 nm vapor deposited aluminum on the back side as given on the manufactures product sheet (ManTech, 2010). No compositional analysis was available for the sample from manufacturer. The sample substrate is a 2.5 μm thick CP1 fluorinated polyimide (PI) material developed by NASA Langley Research Center and manufactured by SRS Technologies. The CP1 material is closely related to polyimide, manufactured by DuPont under the trade name Kapton™ HN. The polymer repeat unit, or mer, for polyimide is shown in FIG. 4.1; it has an atomic composition of $C_{22}O_5N_2H_{10}$. This material is a fluorinated polyimide accomplished by some number of F's replacing H's, although the exact formula is proprietary. However, a range of compositions can be considered when one or more of the ten hydrogen atoms in the polyimide mer shown are substituted by fluorine atoms. It is believed that CP1 has an atomic composition of $C_{22}O_5N_2F_nH_{10-n}$.

In some portions of the material there are embedded Kevlar™ fibers, on the order of ~1 μm diameter. The relative amount of Kevlar to CP1 varies for different portions of the material.
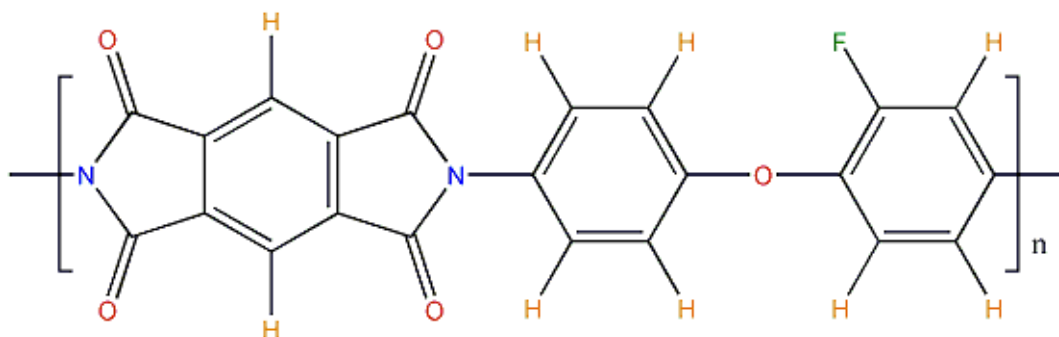
FIG. 4.1. Possible structure of CP1 mer $C_{22}O_5N_2FH_9$.

The polymer repeat unit, or mer, for Kevlar has an atomic composition of $C_{14}O_2N_2H_8$. Because the relative concentration of Kevlar to CP1 is unknown, it has been neglected in this discussion.

The back surface is coated with ~80 nm thick vapor deposited Al (VDA). The aluminum as deposited is usually of high purity, but will become oxidized after deposition. Typical aluminum oxide (Al_2O_3) layers formed in atmosphere are on the order of ~2 nm (Boggio and Plumb, 1966). This is only perhaps 2-3% of the VDA layer by thickness.

There was a 2.5 μm dielectric film (CP1) covering the conducting Al sample. The tabulated value of the dielectric constant for CP1 at 1 MHz and 30% relative humidity is 2.77 (ManTech, 2010). Bulk resistivity of the sample is listed as the tabulated value of the bulk Al resistivity of (2.655 ± 0.004) 10^{-8} Ω-m (Lide, 1993). The tabulated value of the CP1 bulk resistivity is not available. The bulk conductivity was measured with the charge storage methods to be $\sim 2 \cdot 10^{-19}$ (Ω-cm)$^{-1}$ under vacuum conditions (Green $et\ al.$, 2006b). Surface resistivity was calculated based on thickness measurements and the tabulated bulk resistivity values.

For comparison, the tabulated value of the bulk resistivity of Kapton measured with constant voltage conductivity methods is $1.5 \cdot 10^{-18}$ (Ω-cm)$^{-1}$ at 50% relative humidity (DuPont, 2010). The bulk conductivity of Kapton was measured with the charge storage methods to be $\sim 9 \cdot 10^{-20}$ (Ω-cm)$^{-1}$ under vacuum conditions (Dennison $et\ al.$, 2006b).

The radiation induced conductivity was not measured for CP1, but we can approximate it with the values measured for Kapton HN. This can be done because of the chemical similarity of the two polymers.

Reflectivity measurements were made for the sample over a range of photon wavelengths of ~200 nm to ~1100 nm (~1.1 eV to ~6.2 eV), shown in FIG. 4.2 and FIG. 4.3 . Measurements were made using a grating spectrometer (Ocean Optics, Model HR4000) with a resolution of 0.6 meV (0.75 nm) and 0.2 meV (0.25 nm) data increments. A deuterium/tungsten halogen dual light source was used. An Al high-reflectivity specular reflectance standard (Ocean Optics, Model STAN-SSH) was used with a UV-enhanced fiber optic reflectivity probe. Measurements had an estimated uncertainty in reflectivity of ±5%.

Four separate spectra were taken at four different locations on each sample surface. These four spectra were averaged; no appreciable variations were observed between these spectra. Dark current spectra were subtracted from both the average sample spectra and the reflectivity standard spectra; the reflectivity was found as the ratio of these two differences.

A plot of the specular reflectivity at normal incidence as a function of energy is shown in FIG. 4.2a; a similar plot versus wavelength is shown in FIG. 4.3a. A plot of the diffuse reflectivity with both the source and detector in the same fiber optic reflectance probe at 45° from normal as a function of energy is shown in FIG. 4.2b; a similar plot versus wavelength is shown in FIG. 4.3b.

The specular reflectivity of the SRS solar sail sample CP1 side was highly reflective, between 55% to 85%, at lower energies from ~1.2 eV to 3.0 eV. The CP1 sample has a sharp drop off and has a reflectivity of <10% from ~3.7 eV to 4.8 eV. The sharp drop off is identified as an absorption edge in the CP1. The increase in reflectivity above 4.8 eV may result from noise in the lower amplitude signals from both the sample and the reflectance standard above 4.5 eV.
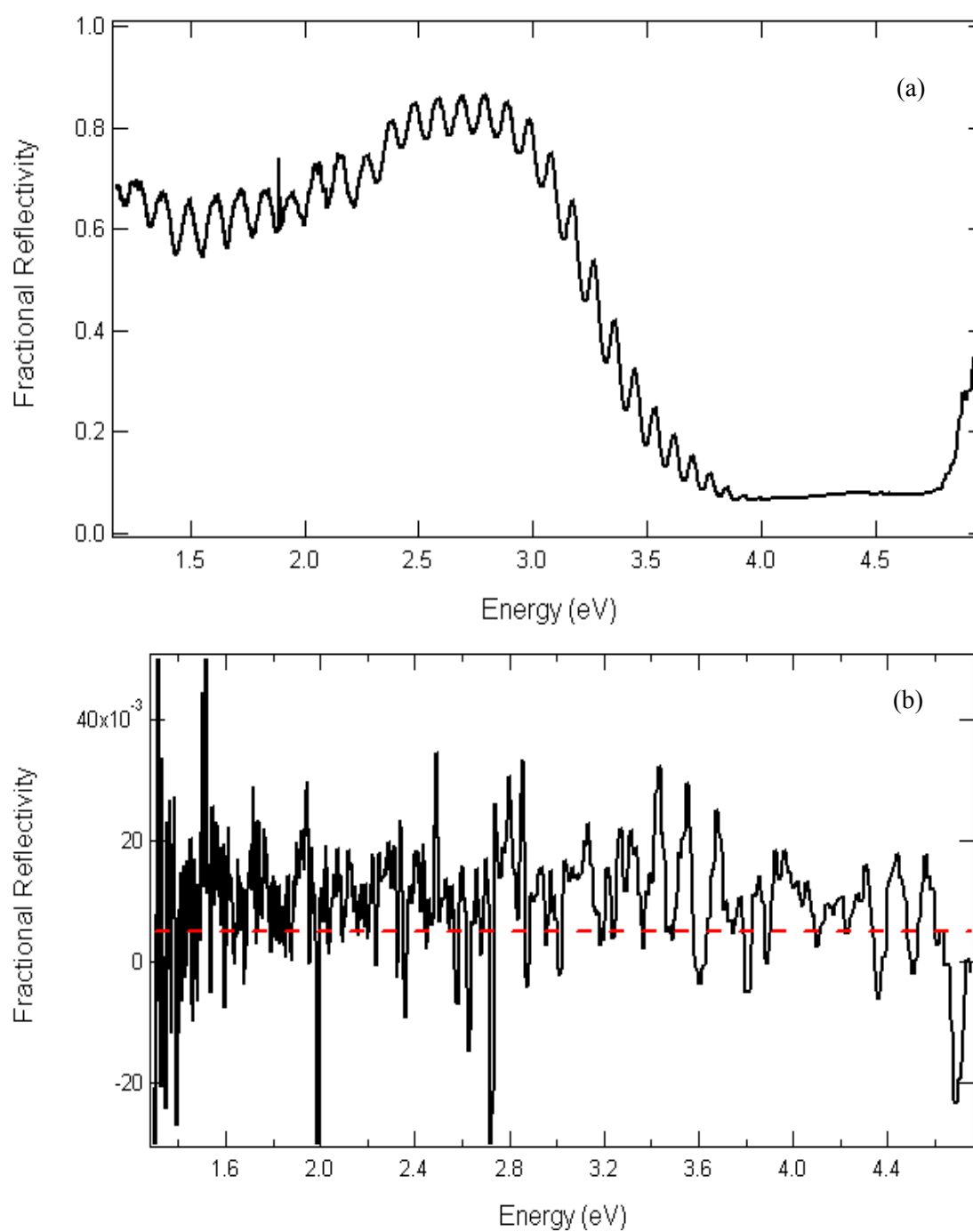
FIG. 4.2. Reflectivity of CP1 as a function of incident energy.
(a) Specular reflection, for normal incidence. (b) Diffuse reflectance for 45° incidence and scattered light.
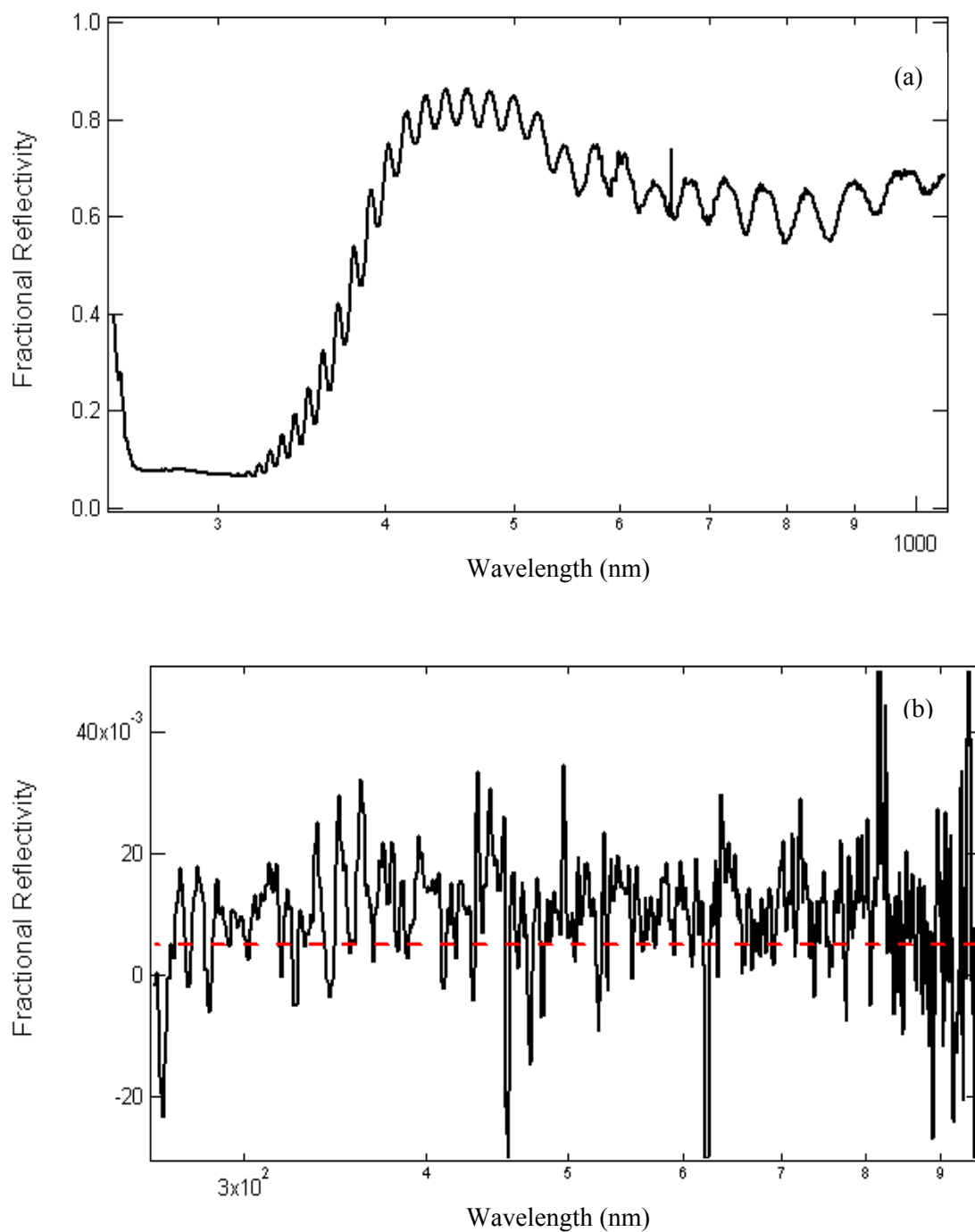
FIG. 4.3. Reflectivity of sample as a function of incident wavelength.
Note logarithmic wavelength scale. SRS—CP1 side. (a). Specular reflection, for normal incidence. (b) Diffuse reflectance for 45° incidence and scattered light.

The reflection spectra exhibits oscillations in intensity that are approximately evenly spaced with 97 meV between peaks, over an energy range of ~1.2 eV to 4.0 eV. The phenomenon is explained as a thin film interference pattern. It can be shown that for this process $\Delta E=hc/2nt$, where ΔE is the energy difference between maxima, h is Planck's constant, c is the speed of light in a vacuum, n is the index of refraction (n is 1.58 for CP1 (ManTech, 2010)), and t is the CP1 film thickness. Based on this model, the CP1 film thickness is found to be ~4 μm, in reasonable agreement with the thickness of ~2.5 μm listed by the manufacturer. The disagreement may be due in part to the presence of Kevlar, which is not taken into account in the calculations. The magnitude of the intensity oscillations is relatively constant with increasing energy, up to the sharp drop-off in intensity. The point at which the oscillations are fully damped is in very good agreement with the UV cut off at 320 nm (3.88 eV) listed by the manufacturer (ManTech, 2010).

Typically, a measure of reflectivity cannot easily reveal an absorption edge, but the nature of this layered material makes this possible. Recall that the back of CP1 is coated with highly reflective VDA and acts as a mirror. Photons impinge on the surface and some are reflected while the rest enter the material, travel through it, reflect off the reflective VDA and interfere with the light initially reflected.

For reference, optical images were taken using an Olympus BX41 microscope and are shown in FIG. 4.4 and FIG. 4.5. What is interesting to note in these photos is the extensive damage of these samples. This material was flight-ready and fully qualified, so this level of damage is surprising.

We have developed a composite function to approximate the range, R, which an incident electron travels before all kinetic energy is lost and the electron comes to rest in the material (Wilson and Dennison, 2010). The function is applicable over more than six orders of magnitude
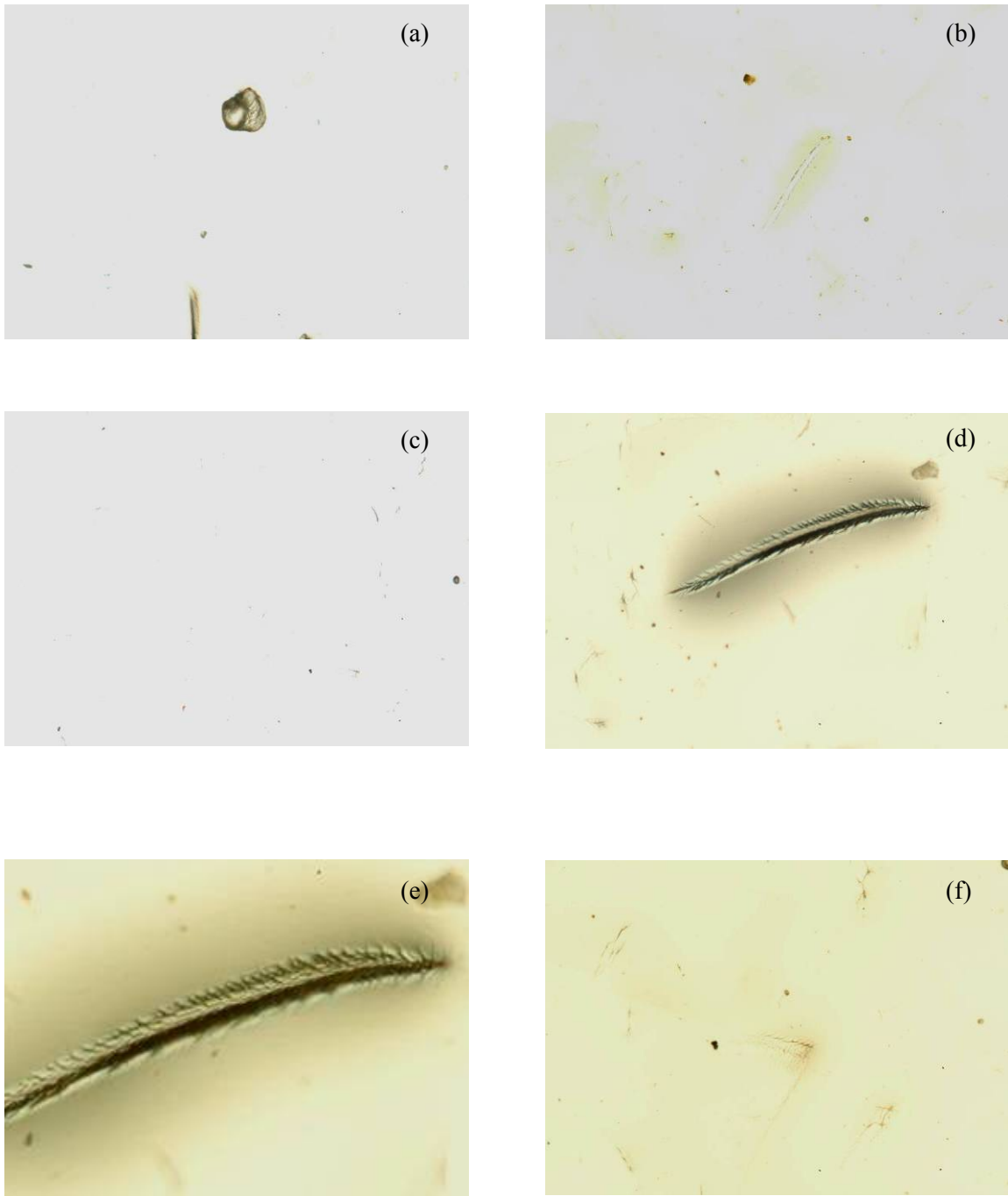
FIG. 4.4. Optical micrographs of the CP1 side of the using the Olympus BX41 microscope. (a-c) Images at 150x magnification showing an image of size 0.64 mm (h) x 0.98 mm (w). (d) Images at 300x magnification showing an image of size 0.32 mm (h) x 0.49 mm (w). Image shows an apparent tear in the material. (d-f) Images at 300x magnification showing an image of size 0.16 mm (h) x 0.25 mm (w). Image shows details of an apparent tear in the material. (f) Images at 300x magnification showing an image of size 0.32 mm (h) x 0.49 mm (w).
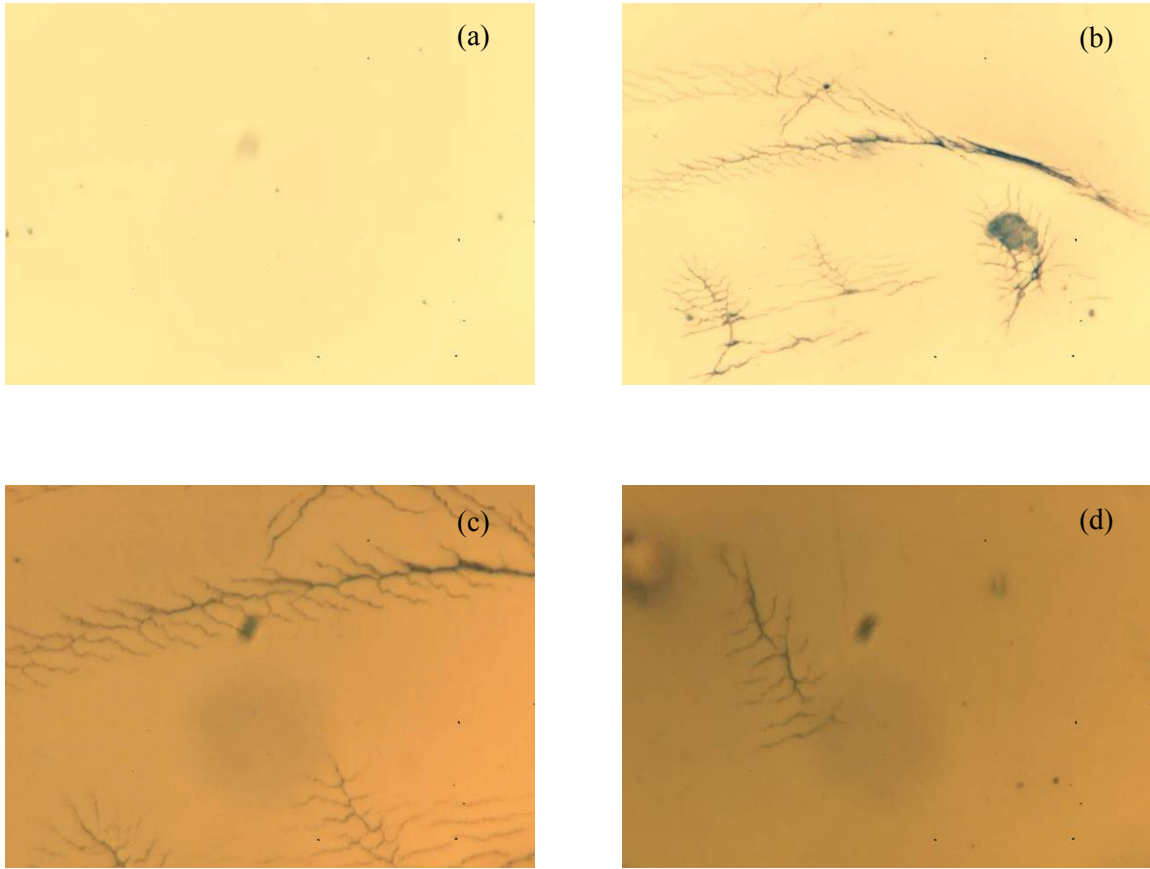
FIG. 4.5. Optical micrographs of the CP1 side using the Olympus microscope.
(a-b) (d) Images at 750x magnification showing an image of size 0.13 mm (h) x 0.20 mm (w).
(c-d) Images at 1500x magnification showing an image of size 0.064 mm (h) x 0.10 mm (w).

in energy (~3 eV to ~ 3 MeV) and range (10^{-9} m to 10^{-3} m), with ~20% uncertainty for a very broad range of conducting, semiconducting, and insulating materials. This is accomplished by fitting data from two standard NIST databases (ESTAR) (NIST, 2010a) for the higher energy range and inelastic mean free path (IMFP) (NIST, 2010b) for the lower energy electron inelastic mean free path). In turn, the data in the NIST databases have been fit with well established semi-empirical models for range and IMFP that are related to standard materials properties (e.g., density, atomic number, atomic weight, stochiometry, and band gap energy or plasmon energy). A single free parameter, the effective number of valence electrons per atom N_v, is used to predict the range over the entire energy span.

Electron ranges at high energies using the continuous-slowing-down approximation (CSDA) are given by the NIST ESTAR database spanning incident energies from ~10 keV to ~1 GeV. The CSDA for range is a very close approximation to the average path length traveled by a charged particle as it loses energy and comes to rest. In this approximation, the rate of energy loss (total stopping power) at every position along the penetration path is assumed constant and equal to $(dE/dx)=E_b/R$; energy-loss variations with energy, E, or penetration depth, x, are neglected. The CSDA range is obtained by integrating the reciprocal of the total stopping power with respect to energy (Spencer, 1955; Reimer, 2000) (or equivalently, the stopping power) over the full penetration depth such that $E_b = \int_0^R \frac{dE}{dx} dx$. This implies $\frac{dE}{dx} = \frac{E_b}{R} = \frac{E_m}{\lambda_m}$ is a constant, with E_m equal to mean energy lost per collision occurring at mean free path λ_m. A reasonable approximation for E_m is the geometric mean of the plasmon energy (as determined from $E_p = \hbar(N_V q_e^2/m_e \varepsilon_0)^{1/2}$) and the bandgap energy times an empirically determined factor of ~3 (Alig and Bloom, 1975).

The ESTAR database (NIST, 2010a) range data are fit using a modified power law formula for the energy dependence of the range, based on the Bethe stopping power formula (Bethe and Heitler, 1934) as extended by Tanuma *et al.* (2005). This formula uses the bandgap energy for semiconductors and insulators and the plasmon energy (or equivalently N_v) for conductors as fitting parameters. Direct extrapolation of the range from the ESTAR data to lower energies is not valid for energies comparable to the atomic electronic structure, typically a few keV and below, because the discrete energy nature of the collisions becomes important.

The NIST Electron Inelastic-Mean-Free-Path Database provides values of electron IMFP in solid elements and compounds at selected electron energies between 50 eV and 10 keV (although most of the available data are for energies <2 keV) (NIST, 2010b). This database was designed mainly to provide IMFPs for applications in surface analysis by Auger electron spectroscopy (AES) and X-ray photoelectron spectroscopy (XPS). It provides IMFP information

for each material from up to three types of sources: calculated IMFPs from experimental optical data for a limited number of materials, IMFPs measured by elastic-peak electron spectroscopy (EPES) for some elemental solids, and IMFPs from predictive formulae for all materials. The calculated and measured IMFPs were fit with the standard TPP-2M formula used to predict the IMFP over an energy span of ~50 eV to ~30 keV (Tanuma *et al.*, 2005).

A simple extension of the CSDA can relate the range to the electron IMFP, where $\frac{dE}{dx} = \left. E_b \middle/ R(E_b) \right. = \left[E_m \middle/ \lambda_o(E_b) \right] \left(1 - e^{-E_b/E_m} \right)$. Here the stopping power is again assumed equal to the total energy lost (incident energy) divided by the total distance traveled (range). This is set equal to the mean energy lost per collision, E_m, divided by the mean distance traveled per collision all times the probability that a collision occurs, $\left(1 - e^{-R/\lambda_m} \right) = \left(1 - e^{-E_b/E_m} \right)$. Here, the energy dependence in the range is fully contained in the energy dependence of the mean free path. For $E_b > E_m$, $\lambda_o(E_b)$ is assumed to be given by the TPP-2M formula used in the NIST IMFP database, while for $E_b < E_m$, the IMFP is constant and equal to the IMFP at the mean energy loss or $\lambda_o(E_b) = \lambda_m$. Zangwill also presents a universal curve of mean free paths for conductors at lower energies (Zangwill, 1988), which provides an estimate of the IMFP below ~50 eV. As a final step, the power law fit of the ESTAR data and the extended range formula based on the TPP-2M fit to the IMFP data are set equal at points in the intermediate incident energy span; this allows a composite fit to the data with only a single fitting parameter.

Plots of the range for Kapton HN based on this method are shown in FIG. 4.6. A complete discussion of this calculation is beyond the scope of this work but is discussed in more detail by Wilson and Dennison (2010).
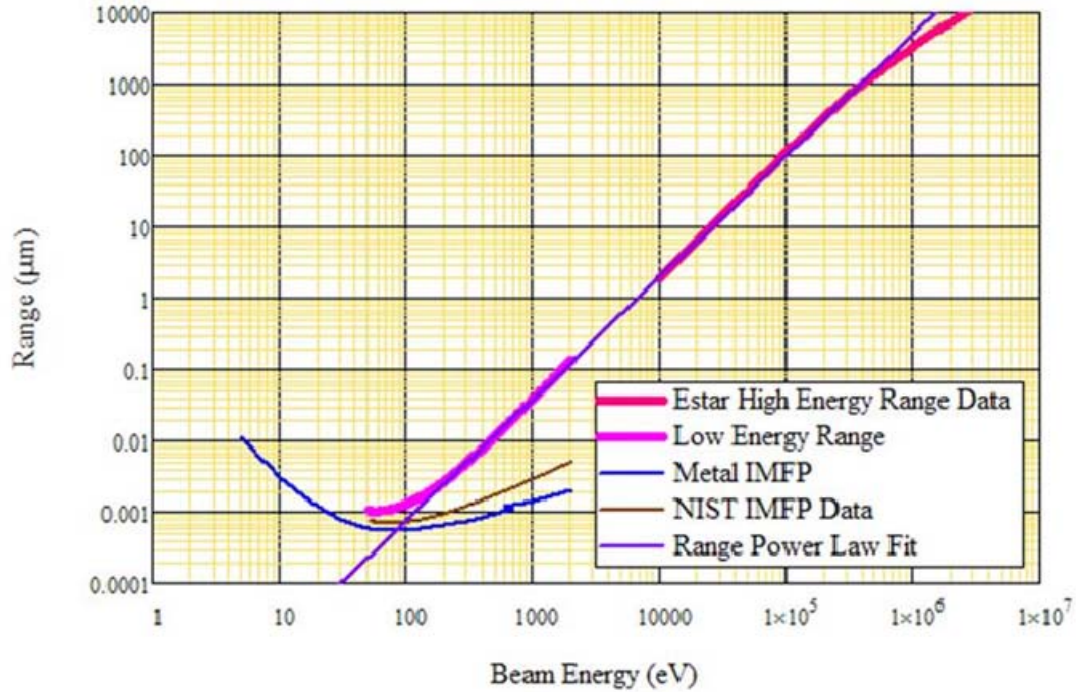
FIG. 4.6. Penetration range of Kapton HN.

4.1.2 Electron-Induced Emission

To measure points on the yield curves at a particular energy, a series of ~10 to 200 or more pulses at constant incident energy are measured with ~5 sec of neutralization between each pulse using both low energy electron flooding and visible-ultraviolet flooding as described in Section 3.2. A similar series of pulses at fixed incident energy, taken without neutralization, constitute so-called electron yield decay curves. For each curve there are speculations about the effects that charging is having on the yield. These are only speculations at this point, but they do provide a useful back drop for the discussion.

Data are then presented for BSE yields. At this point it is necessary develop methods for determining the crossover energies and electron emission spectra. These two data sets, taken together, help to explain some of the anomalous results seen in the preceding sections.

Finally, a decay curve is measured to establish the susceptibility of CP1 to charging. These data indicated that CP1 is not particularly charge susceptible despite the obvious charging features seen in the sections above. This might be explained by the application of RIC to our understanding of how the material charges (Dennison *et al.*, 2007).

4.1.2.1 SE Yield

Measurements of the SE yield were made using the pulsed system, due to initial problems with surface charging of the samples with the DC system. FIG. 4.7a shows the SE yield as a function of incident electron energy, with energy on a log scale. The green line in FIG. 4.7a is a best guess at what the yield curve might look like without the effects of charging. The overall shape of this line is based on the 5 parameter fit used by NASCAP 2K modeling code (Mandell *et al.*, 2001) to model the electron yield curve. It was projected by assuming the yields at the crossover energies are unaffected by charging. It is used to provide a guide only and while it is based in SE yield theory two points (E_1 and E_2) are not enough data to provide anything more than an educated guess.

Values obtained for the SE yield parameters for CP1 surfaces of SRS Solar Sail have not been measured previously. The best fit to the SE yield curve was provided by the NASCAP five parameter SE yield model. For this model, we found values for the five parameters of $\delta_{max} = (1.10 \pm 0.01)$ electrons/electron, $E_{max} = (0.17 \pm 0.01)$ keV, $b_1/b_2 = (0.32 \pm 0.02)$, $n_1 = (0.47 \pm 0.1)$ and $n_2 = (1.55 \pm 0.01)$. The values for the five parameter fit values differ from those stated in the original JPL report for CP1 (Dennison *et al.*, 2006a). This is due to an error in the calculation of b_1/b_2 and is corrected here.

It is interesting to note that the general shape of the secondary electron yield curve for the CP1 side of the sample (excluding the regions from 600 eV to 1600 eV and 6000 eV in FIG. 4.7a) is rather similar to the secondary electron yield curve of the Al side of the same sample (FIG. 4.7b). Recall that this material has CP1 on one side and a thin coating of VDA on the other. The
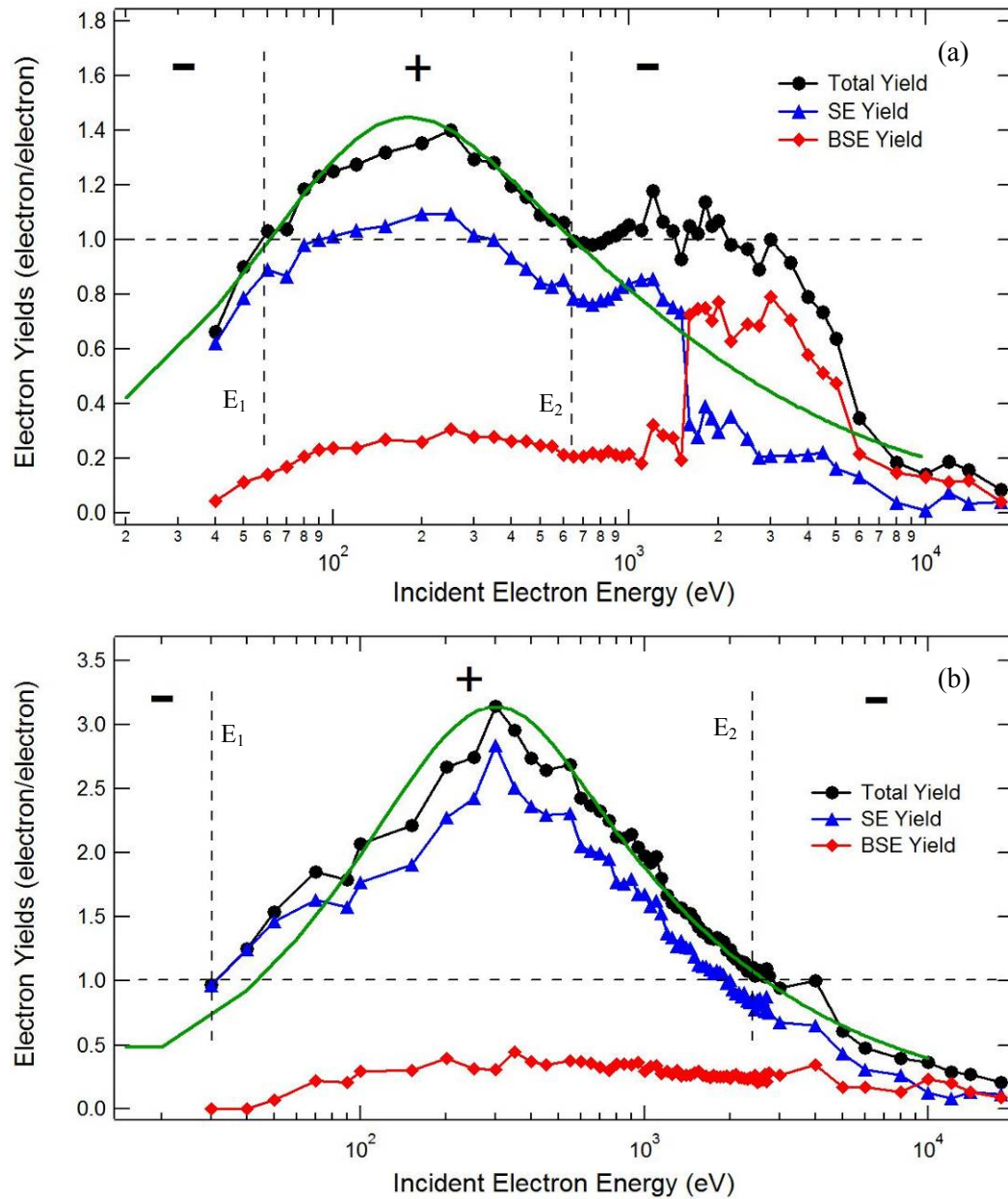
FIG. 4.7. Yields from CP1 and VDA.
(a) Total, SE and BSE yields as a function of incident electron energy on CP1. (b) Total SE and BSE yields of the oxidized VDA side of the material shown here for comparison to the CP1 side of the material. The dashed horizontal line indicates a yield of one and the two vertical lines indicate when the total yield changes from a negative to a positive regime, E_1 and E_2 respectively. The green lines in both plots indicate a best guess at an uncharged total yield.

overall magnitude of the CP1 secondary electron yield curve, however, is a factor of ~2.2 smaller than that from the oxidized Al of the SRS sample. In fact, δ_{max} for the CP1 side is much closer to that of unoxidized Al (Dennison *et al.*, 2006a), which is near $\delta_{max}=1$. It is interesting to speculate that this may somehow result from the CP1 yield curve partially originating from the unoxidized rear surface of the 80 nm vapor deposited Al of the SRS sample. Insulators are known to have significantly longer inelastic mean free paths than conductors, as a result of the presence of a band gap that inhibits scattering of low energy electrons. The absorption edge seen in the reflectivity measurements of CP1 on Al clearly indicates a band gap of ~4 eV in CP1 (ManTech, 2010). Most emitted secondary electrons have energies less than 4 eV (see FIG. 2.4) and would therefore have a longer inelastic mean free path. Still, it would be surprising but not impossible for the secondary electron to have an inelastic mean free path as large as 2 μm, the thickness of the insulating side. A rough approximation for the inelastic mean free path of a SE as it makes its way to the surface is ~0.2 μm (Donegan *et al.*, 2010).

Figure 4.8a shows the total and BSE yields for CP1 with curve discretized into several distinct areas (zones 1-6) and specific energies (A-C). At first glance this curve does not seem to make much sense, as it does not follow the typical profile one would see in an uncharged conductor. If we take each section in turn and apply what we know about penetration range, internal charge distribution and how that charge will affect the yield, we can start to speculate about the deviation of the measured (charged) yield from the ideal uncharged (green curve in FIG. 4.7a) yield.

We start by identifying the zones and points of interest in FIG. 4.8a. In zone 1 below E_1 SE yield is not affected by charge. At these energies the IMFP of the SE is greater than the incident electron IMFP. Also, below 50 eV BSE cease to be defined and $\sigma=\delta$. In this energy range the DDLM is not an accurate model. At point A (namely E_1) there is no net charging by definition. Here E_1 is less than the minimum in the IMFP curves so the DDLM is again

inapplicable. Zone 2 spans from above E_1 to below E_2 and makes up the section of the total yield

curve that results in positive charging. As such, the total yield curve is depressed due to positive

sample charging and the subsequent reattraction of some SE's. The BSE yield in the section is

unaffected by the relatively small positive surface potential. Point B (namely E_2) is accurate as

there is no net charge accumulating on the sample and $\sigma=1$. The BSE yield at this point is also

accurate. Zone 3 for $E_2<E_o<\sim 1200$ eV is above the true uncharged total yield depicted by the

green line. This may result from extra SE from the depletion region (surface side of the negative

deposition layer at the penetration depth R) that are accelerated out due to the large electric field

from the negative layer at R. We will also observe that the BSE are near normal or slightly

depressed. Zone 4 in the range of 1200 eV $<E_o<1500$ eV total yield is still above the true yield ,

but decreasing as many of the SE's are accelerated up into the BSE range (>50 eV). In this

section we start to see an increase in the BSE yield as we would expect. At about 1500 eV at

point C there is a large jump up in the BSE yield at the expense of an approximately equal

decrease in δ and a commensurate drop in the SE yield. This occurs as the peak in the electron

emission spectrum (nominally at ~ 4 eV) is accelerated to greater than 50 eV by a large net

negative surface potential. That is, SE from the depletion region are now being measured as extra

BSE as they meet the criteria of having energies over 50 eV. In zone 5 the total yield is enhanced

because of the negative surface potential and the acceleration of the SE up into the BSE range. In

zone 6 total and BSE yields largely to return to the idealized uncharged green curve as essentially

all SE have been accelerated to BSE and the number of SE that can be accelerated continue to fall

with increasing incident energy.

  This could be due to a physical breakdown in the material; that is to say, the surface

voltage V_s exceeds the voltage for electrostatic breakdown V_{esd} typically 278 MV/m or ~ 700 volts

for Kapton HN. However, given E_o at zones five and six boundary at ~ 6000 eV and $E_2^{eff}\approx 3100$

eV, this doesn't appear to be related to E_{esd}. The notion of the PE being reflected by the surface
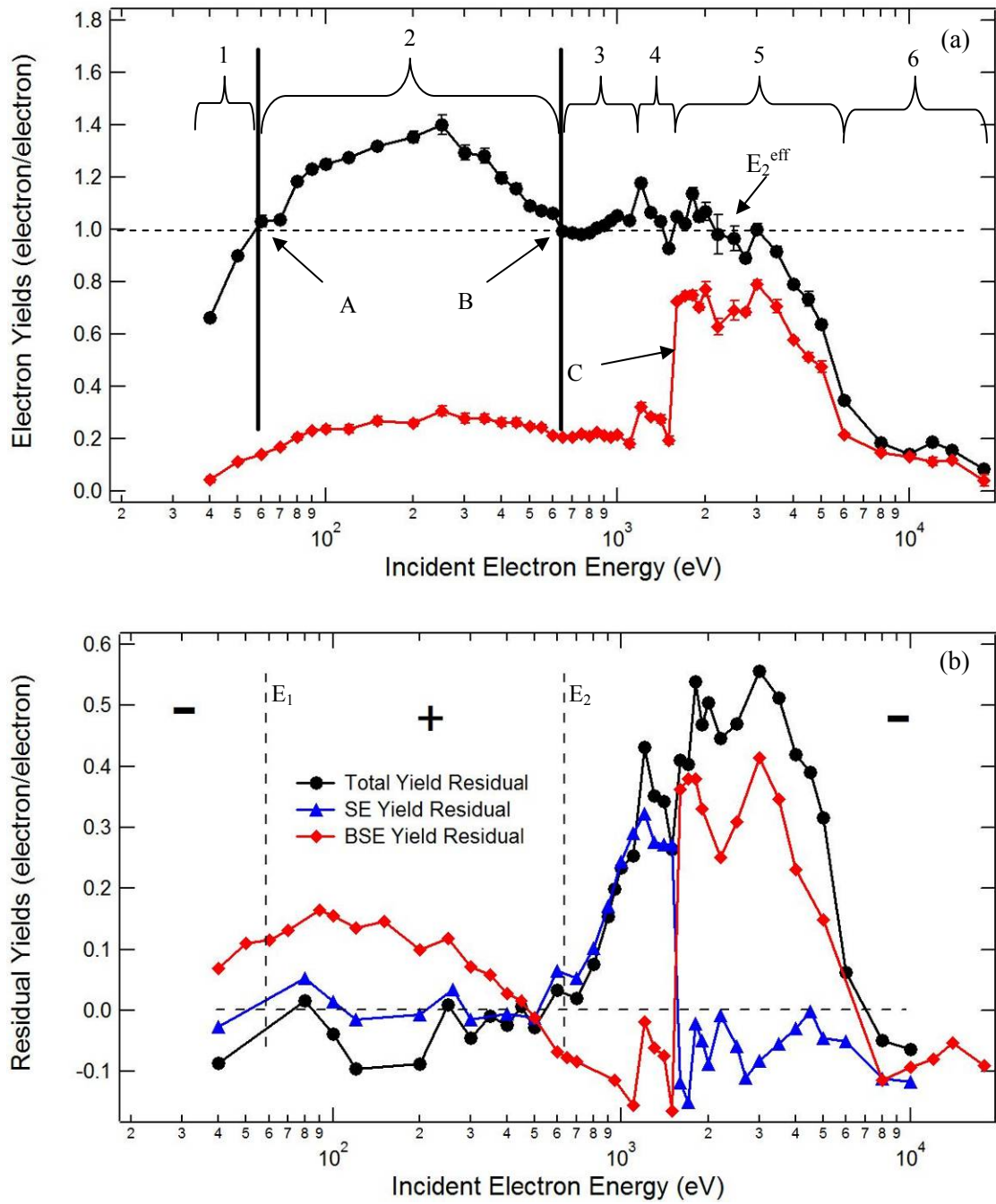
FIG. 4.8. Discretized and residual yield for CP1.
(a) Total yield (black) and BSE (red) for CP1 showing zones 1-6 and points A-C as discrete regions of charging behavior. (b) The difference between the idealized fits to the total (green line in figure 4.1.5), SE (5 parameter fit) and BSE (3 parameter fit in FIG. 4.7) and the data from CP1 that exhibits evidence of charging.

potential (i.e. mirror method) suggests a surface voltage at equilibrium charge with an effective total yield of unity at a landing energy of $E_b–E_2$ (or perhaps $E_b–E_2{}^{eff}$). The observed transition from zone five to six occurs at ~6000 eV for CP1, that is 5350 eV above E_2.

4.1.2.2 BSE Yield

Measurements of the BSE yield were made using the pulsed system, as was done for the SE yield. The BSE yield as a function of incident electron energy is shown in FIG. 4.9, with energy on a log scale. The plots include the NASCAP one parameter fit and an extended three parameter fit to the BSE yield curve (Mandell *et al.*, 2001) (note, these fits are heavily influenced by the enhanced BSE yields in zones four and five). Z_{eff}, referred to as the effective atomic number, a fitting parameter for BSE yield has no direct relation to atomic number (Levy *et al.*, 1985). The fitting parameters for the extended fit of the maximum value of the CP1 side of the samples BSE yield was found to be (0.45 ± 0.02) electrons/electron. Our measured energy for the CP1 side of the samples has a maximum BSE yield of (0.27 ± 0.01) keV. The value of Z_{eff} for the one parameter NASCAP fit to the BSE yield curve of the SRS Solar Sail sample of $Z_{eff} = 13.0 \pm 0.5$. The NASCAP fit is not a good fit, but it is shown here to highlight the inadequacy of the model for BSE used in the modeling code.

The eccentricities of this curve are speculated on in Section 4.1.2.1 and are not repeated here as they are intimately tied to the charging induced behavior of the SE's. The green line in FIG. 4.9 is an estimate of at the BSE yield without charging effects. The three parameter fit plotted in this figure is usually a good fit, but it is distorted here because it is not able to account for the SE→BSE shift in zones four and five.

4.1.2.3 Determination of Crossover Energies

Determination of the two crossover energies E_1 and E_2 is a key point in the understanding of the charging behavior of a material, as seen in the previous section. These two points provide
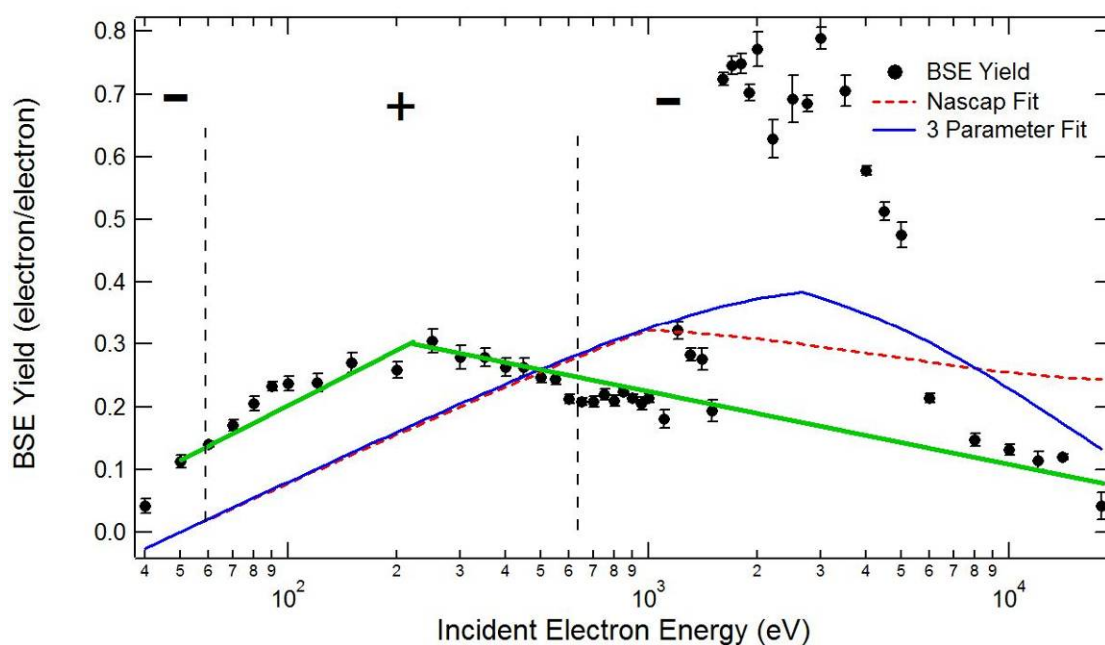
FIG. 4.9. Backscattered electron emission yield curve for CP1.
The plot includes the NASCAP one parameter fit and an extended three parameter fit to the BSE yield curve.

fixed points for all the fits that may be preformed. As such it is important to use several methods

of determination to bolster our confidence in crossover values. This section describes several

independent methods for finding the crossover energies.

The crossover energies have been determined using four methods (Abbott and Dennison,

2005). Values for the first and second crossover energies are compared in Table 4.1.

TABLE 4.1. Crossover energies determined by various methods

Method	CP1 Crossover Energy (eV)
Yield Curve	E_1: 61±2 E_2: 650±20
Null Current	E_1: 54±1 E_2: 660±20
Spectral shift	E_1: 65±5 E_2: NA
BSE-to-SE Ratio	E_2: 600±30
Best Estimate	E_1: 60±5 E_2: 640±20

Yield Curve Method: The first method simply interpolates the yield curve data to determine where the total yield is unity. This can be seen in FIG. 4.7a as the green line crosses the horizontal dashed line indicating a yield of one.

Null Sample Current Method: The second method takes advantage of the fact that when a crossover is reached, the charge entering and leaving the material exactly balance and the sample current is zero. Since it is difficult to take high-resolution measurements in energy, a linear regression of the energy verses sample current gives us the intercept point.

Spectral Shift Method: The third method determines the onset energies of sample charging as indicated by shifts in the sample SE peak in the electron emission spectra. Specifically, the crossover energy is found as the energy midway between an unshifted (or more correctly, slightly left shifted peak due to smaller positive charging) emission spectrum for which the grid and sample SE peaks are not separated and a shifted (or more correctly, a largely right shifted peak due to larger negative charging) emission spectrum. This effect can be seen in data presented in Section 4.1.2.4.

SE-to-BSE Ratio Method: A fourth method provides crude determination of the second crossover energy. Above the second crossover energy, the sample charges negatively and SE are imparted extra energy as they leave the charged sample surface. When the surface has charged to perhaps -45 V, the low-energy SE electron in the peak of the emission spectrum have more than 50 eV and are counted as BSE electrons rather than SE electron. This produces a sharp jump in the BSE yield and concomitant decreases in the SE yield above the second crossover energy. This method only works for insulators. The resolution of the SE-to-BSE ratio method is limited by the necessity to shift the majority of the SE with energies near the SE peak to more than 40 eV to enhance the BSE yield over the SE yield. Depending on many material parameters such as dark current conductivity and RIC, -50 V may be reached quickly after the crossover, or if charge is bled off quickly the potential may never exceed -50 V. For this reason this method is the crudest

and provides only a limiting estimate for the second crossover. That is to say that the second crossover will never be higher than the jump in the SE→BSE ratio.

4.1.2.4 Electron Emission Spectra

Measurements of the electron-induced electron emission spectra were made using a low-energy electron gun operating in the continuous mode at incident energies of 30 eV to 600 eV with a beam current of ~ 5 nA, a ~1 mm diameter beam spot and a beam current density of ~50 pA/cm^2. Full-range electron-induced emission spectrum, including the low-energy SE peak and the high-energy elastic peak, are shown in FIG. 4.10. The positions of the high-energy elastic peaks are in good agreement with the incident beam energy. The elastic peak shape is dominated by the instrumental broadening of the peak. All elastic peaks are well fit with Gaussians with average FWHM of (3.8 ± 0.3) eV. The Gaussian FWHM corresponds to the instrumental resolution, largely from the hemispherical grid retarding field analyzer, in particular from the non-uniformity of the retarding grids. Note that the asymmetric shape of the elastic peak, with a larger FWHM at lower energies than higher energies, is predicted by the theory of Doniach and Sunjic (1970). Kite provides a detailed discussion of the origins and shape of the SE, quasielastic and elastic peak features over a range of electron emission energies and angles (Kite, 2007). Plots of the electron-induced emission yield curve are shown in FIG. 4.10 and FIG. 4.11, which also show a four parameter fit to the SE peak based on the Chung and Everhart model discussed in Section 2.2 (Chung and Everhart, 1974) and tabulated in TABLE. 4.2. Some of the fits shown in this section may be distorted as the SE peak originating from the inner grid was not subtracted from the data prior to fitting the data. The average measured low-energy secondary electron emission peak position for uncharged CP1 side of the samples are (3.4 ± 0.4) eV. The average measured FWHM was (6.2 ± 0.6) eV. The average work function of the sample is measured as (7±1) eV using the electron-induced emission spectrum. A prediction of the Chung and Everhart model is that the peak energy is one third of the work function (Chung and Everhart, 1974). Since
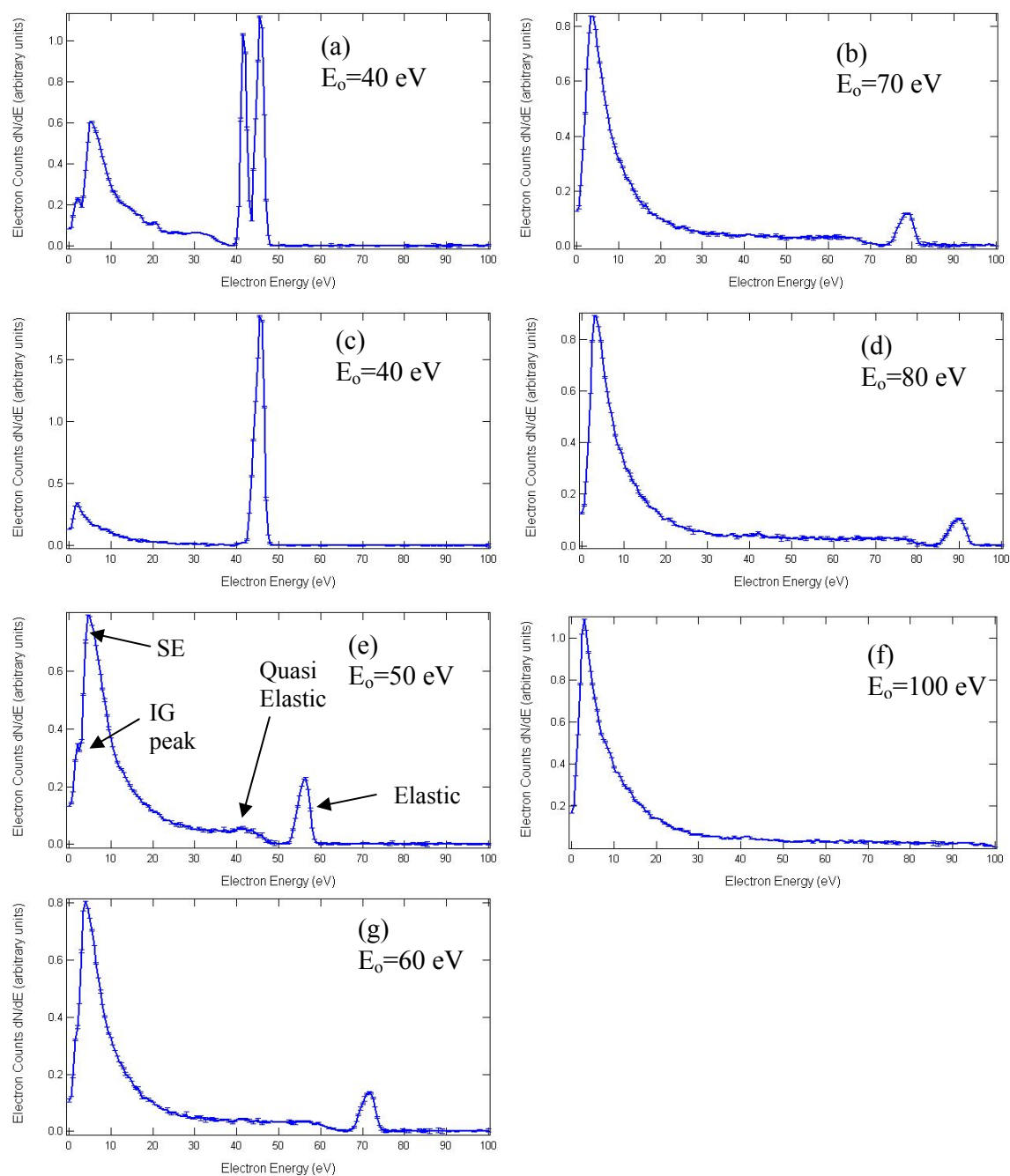
FIG. 4.10. Full-range emission spectrum from CP1.
(e) Incident beam energy is 70 eV. SE peak and the high energy elastic and quasi elastic peak. Also note the low energy peak from detector grid secondary electron emission.
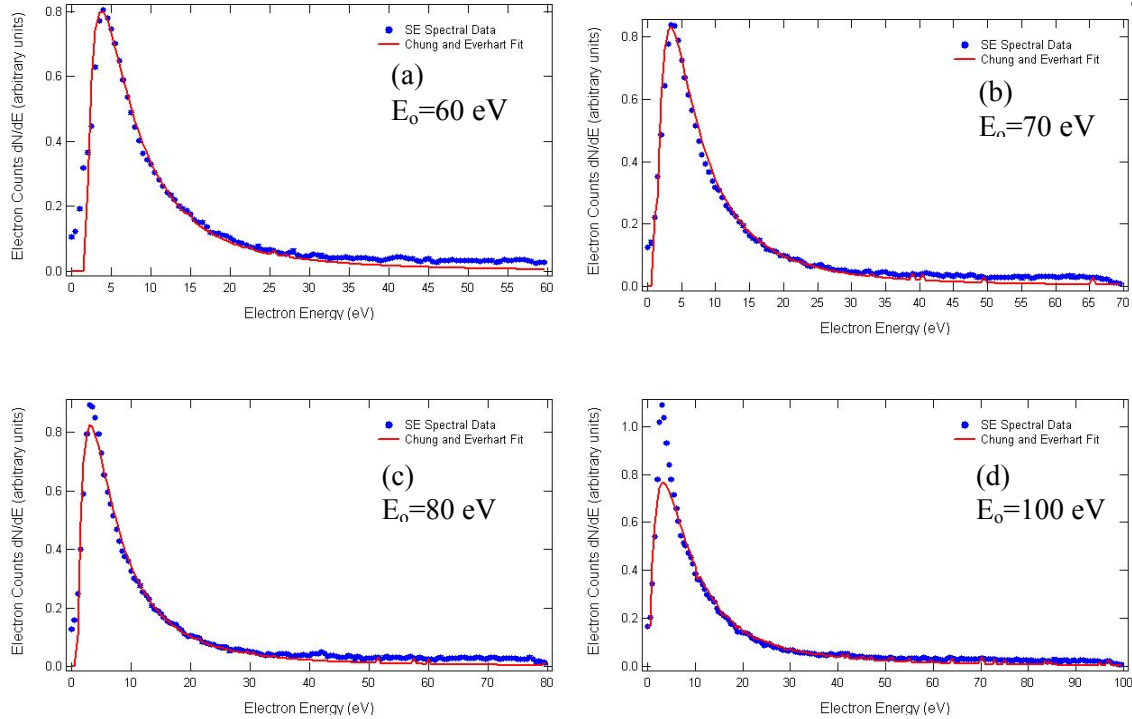
FIG. 4.11. Details of electron emission spectra on CP1 with a Chung fit to the SE peak. No other fits were preformed because the inner grid peak interferes with fitting algorithm and will need to be subtracted out for a better fit.

we do not have a measurement of the work function of CP1 we can compare to the work function

of Kapton HN, a good estimation this is 4.36 eV. If this is an accurate surrogate value for CP1,

the prediction by Chung is not true as the ratio of peak position (3.4 eV) to work function (4.36

eV) is 78 %. However it is easy to imagine that the work function of CP1 is much higher than that

of Kapton based solely on the fact that CP1 is transparent in the visible range and Kapton has an

orange color. This would imply that the work function for CP1 is higher and might be near the

10.2 eV required for the peak position to be 33% of its value. Also, note the low-energy peak

from detector grid secondary electron emission. This peak has lower intensity than the main SE

peak. Further, the grid peak does not move with changing sample charge (or bias) as does the

larger sample SE peak. Thus, the grid peak acts nicely as a fiducial mark, to which the charge

induced shifts of the sample SE peak may be referenced. Separation of these two peaks is

indicative of sample charging and can be used to determine the crossover energies (see Section 4.1.2.4). We do not see the elastic BSE peak being affected by the surface potential, because the incident electrons lose (gain) energy as they near a negative (positive) surface potential. Once elastically scattered, they will gain (lose) the same amount of energy from the electric field on the way out. Inner grid/sample peak separation is observed at incident energies of 60 eV and below, consistent with negative charging below the E_1 crossover energy of 54 eV to 62 eV as determined by other methods (see TABLE 4.1). At the lowest incident energy, 40 eV, we observed unexpected emission spectra, as shown in FIG. 4.10a-b. The dual peaks may be evidence of sever negative charging, 40 eV is well below E_1 and the sample would develop a negative charge. No SE peak shifts are observed for incident energies from 70 eV to 100 eV because the sample is charged positively and this does not affect sample peak position, only the peak magnitude as discussed in Section 3.1.3. In FIG. 4.10e the inner grid, SE, quasi elastic and elastic peaks are all indentified. Other typical features are also identified in Section 3.1.2 for reference. At incident energies of 200 eV to 600 eV there were significant peak shifts observed, on the order of +3 eV to +9 eV. It is important to note that these are shifts in peak position, not sample potential. Such negative charging is not typically expected in the regime between crossover energies where total yield is greater than unity. The creation of additional trap sited in the band structure of the material could lead to changes in the charging behavior. In Section 4.2.3 there is a body of data on damaged Kapton a discussion on how radiation damage may explain some of the results seen in that section.

TABLE 4.2. Fitting parameters for the secondary electron peak of electron emission

Material	Secondary Electron Peak Parameters				
	Energy (eV)	FWHM of SE Peak (eV)	Peak Position (eV)	Energy Shift (eV)	Work Function (eV)
	60	6.0 ± 0.5	4.00 ± 0.13	1.754± 0.006	6.104± 0.001
CP1	80	7.0 ± 0.5	3.25 ± 0.25	0.90± 0.01	6.710± 0.001
	100	5.5 ± 0.5	3.00 ± 0.13	0.269± 0.001	9.027± 0.002

4.1.2.5 Decay Curve

To study the effect of charge accumulation on the electron yield, an electron yield decay curve was measured for CP1, as shown in FIG. 4.12. An incident energy of 300 eV was used. Since this energy is near the maximum electron yield (see FIG. 4.7a) with an uncharged yield greater than unity, and between the crossover energies, the sample was expected to charge positively. As the sample charges to higher positive values, more emitted electrons are re-attracted to the surface, causing the yield to asymptotically approach unity. A series of 2000 ~5 μs wide pulses at ~5 s intervals, each containing ~500 fC/pulse or $3 \cdot 10^6$ electrons/pulse with a spot size of ~1.7 mm diameter and beam energy of 300 eV, were incident on the sample, without charge neutralization. This results in ~1 nC total incident charge, and given a total yield of ~1.6 at 300 eV we can estimate the total flux to be ~2 nC. Using Eq 3.19 from the DDLM, we calculate that the induced surface potential is ~12 V or ~8 MV/m. This voltage is sufficient to recapture 81% of the escaping SE, but nowhere near the 278 MV/m required for breakdown. For highly insulating materials, the charge accumulates rapidly and changes in the yield are evident for small charge accumulation, as low as 10^6 fC/m^2 (or equivalently, charge density of 10^{10} electrons/cm^3) (Hoffmann *et al.*, 2008). However, because CP1 has a somewhat lower resistivity, incident charge leaks through the material, partially dissipating the charge in the incident pulse in the time intervals between pulses.

Based on charge storage measurements of the conductivity of ~$(2 \pm 1) \cdot 10^{-19}$ (Ω-cm)$^{-1}$ and a relative dielectric constant of 2.8 ± 0.1, simple theory predicts that a charge decay time of $5 \cdot 10^8$ s or 16 years, using $\tau = \varepsilon_o \varepsilon_r / \sigma_{DC}$ (Green *et al.*, 2006a). This suggests that some mechanism other than the dark current conductivity may be responsible for the decay shown in FIG. 4.12, RIC being the most likely suspect. We can calculate the total dose of the entire experiment that lasted 2.8 hr using Eq (4.0) where J_{in} is the beam current density, E_o is the beam energy, ρ_d is the density (1460 kg/m^3), q_e is the charge on an electron, and R is the penetration depth.
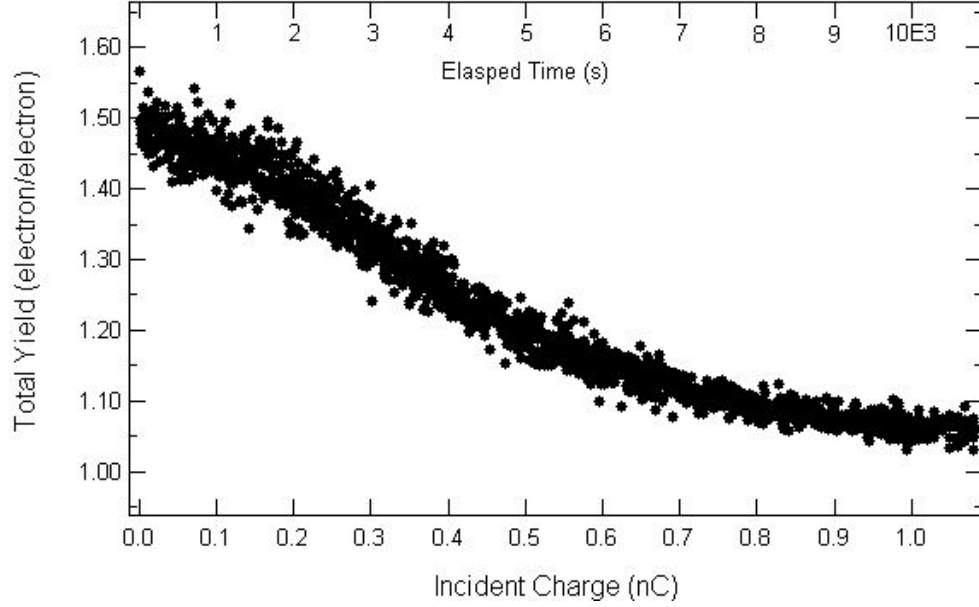
FIG. 4.12. Electron yield decay curve for CP1.
Data taken at 300 eV incident energy for a series of 2000 ~5 µs wide pulses at ~5 s intervals, each containing ~500 fC/pulse or $3 \cdot 10^6$ electrons/pulse with a spot size of ~1.7 mm diameter, on the SRS sample—CP1 side, without charge neutralization.

$$\dot{D} \equiv \frac{\partial D}{\partial t} = \frac{EoJ_{in}}{\rho R q_e} \quad . \tag{4.0}$$

We can then use the Eq. (4.1) to calculate the RIC ($\sigma_{ric)}$ and the charge decay time.

$$\sigma_{ric}(\dot{D}) = k_{ric} \dot{D}^{\Delta} \quad . \tag{4.1}$$

This allows us to see how these values compare to the dark current decay time and the duration of the experiment.

Delivering 500 fC in 5 µs gives yields a dose rate of $2.8 \cdot 10^7$ rad/s and a RIC value of $1.7 \cdot 10^{-10}$ $(\Omega \cdot cm)^{-1}$, nine orders of magnitude larger than σ_{dc}. This corresponds to a charge decay time of 2 ms, significantly shorter than the time scale of each pulse cycle. This means that each pulse is shorting out the internal charge distribution and allowing charge to recombine. This does

not, however, short the charged layers to ground and the RIC enhancement only affects the material between the surface and the penetration depth.

The values stated in the paragraph above do not take into account the fact that there is a finite amount of time required for the material to respond to the extra energy from the incident electron (typically the response time is on the order of a few tens of seconds) (Dennison *et al.*, 2008). To account for this in a pulsed system, it has been shown that as long as the duty cycle of the pulses (5 s) are less than the decay time (tens of seconds), we can approximate the RIC value by assuming the flux from the pulse is delivered over the full five seconds rather than 5 μs (Dennison *et al.*, 2008). This is reasonable to do in this case, but it provides an approximation only.

The pulse contains 500 fC/pulse and 5 μs long with 5 s between each pulse resulting in the beam delivering 100 fC/s. This gives a beam current density of 1.1 pA/cm^2, 28 Rad/s and using the parameters from Kapton HN (k_{ric}=6·10^{-18} (Rad·sec^{-1}·Ω-cm)$^{-1}$, Δ=1.0) RIC value of 1.7·10^{-16} (Ω·cm)$^{-1}$, about three orders of magnitude larger than σ_{dc}. This leads to a decay time of 1440 s and is 0.1% the decay time if RIC is not included. This decay time is 16% of the total time required to take the data. It seems reasonable that CP1 would slowly but eventually reach equilibrium potential and unity total yield. This idea will become key point in discussing high current beams on aluminum oxide in Section 4.3.3.

4.2 Low-Conductivity Low-Yield (Kapton HN)

Kapton HN is one of the most widely used materials in spacecraft construction; as such no discussion of material charging in relation to spacecraft would be complete without a thorough investigation of Kapton. It also provides us with an intermediate step in determining the full capabilities of the pulsed yield system. Kapton has very low conductivity and stores charge very well. It also provides an increased yield above that of CP1; the increased yield increases its charge susceptibility and provides a more challenging material.

In addition to its favorable material properties, Kapton has been very widely studied in the open literature and should provide a useful benchmark to determine accuracy and reliability of the pulsed yield system.

4.2.1 Material Characterization

This sample is a layered material comprised of a ~27.5 μm polyimide (PI) film with ~80 nm vapor deposited aluminum (VDA) on the back side. The film was manufactured by DuPont and purchased through Sheldahl. No compositional analysis was available from the sample manufacturer. The PI polymer repeat unit, or mer, for polyimide is in FIG. 4.13; it has an atomic composition of $C_{22}O_5N_2H_{10}$ (DuPont, 2010).

The aluminum as deposited is usually of high purity, but will become oxidized after deposition. Typical aluminum oxide (Al_2O_3) layers formed in atmosphere are on the order of ~2 nm (Boggio and Plumb, 1966). This is only perhaps 2-3% of the VDA layer.

The Al surface of the Kapton samples are attached to a Cu mounting slug using double sticky Cu tape with the Kapton side facing the beam. Microscopic images were taken using both an Intel QX3 low magnification microscope and an Olympus BX41 high magnification microscope. They were lit from the top to expose surface defects and from the bottom to show
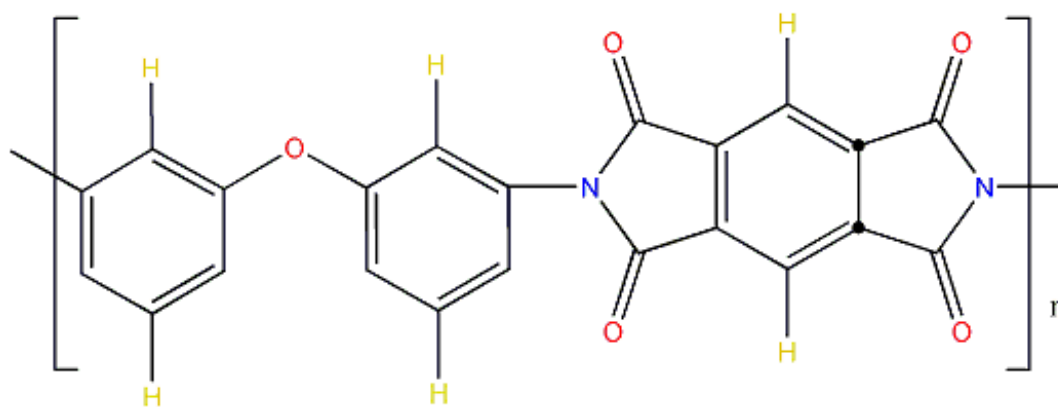
FIG. 4.13. Structure of Kapton[TM] mer $C_{22}O_5N_2H_{10}$.

defects in the VDA substrate. FIG. 4.14 shows the images taken from these microscopes. The most prominent features to note are the long scratches in both the VDA and the Kapton layer. Some of this damage is deep enough to totally remove the VDA layer. This is evidenced by the green backlighting showing through in both FIG. 4.14 and FIG. 4.15. These defects measure ~0.25 mm long and are spaced roughly 2 mm apart. It is estimated that as much as 1% of the VDA coating might be missing from this material. It should be noted that these materials were handled with extreme care during the cleaning and mounting procedure at USU.

It is believed that these defects originate from the manufacturer and that they are a consequence of the manufacturing process. It was a bit surprising to find this level of damage on spaceflight-ready materials direct from the manufacturer, but in the future it should be considered that all layered materials will have similar defects.

The defects shown here may not compromise the mechanical strength or the optical properties of the material, but they will have consequences for charging. With the grounded Al backing removed from the material, stored charge will be forced to travel greater distances to ground. One might imagine a scenario where localized charge gradients developed as a result of damage to the grounded VDA backing. This will likely be small, but should still be considered.

Using several NIST databases we have estimated electron penetration range as described in Section 4.1.1 (Wilson and Dennison, 2010).

4.2.2 Electron-induced Emission

All electron-induced emission data discussed in this section were taken with the pulsed yield system as described in Section 3.2. The electron emission of a material determines how quickly a material will charge. This, in competition with conductivity, is what defines the equilibrium voltage a material will eventually reach.

To measure points on the total, SE and BSE yield curves at a particular energy and electron flux density, a series of ~10 to 200 or more pulses at constant incident energy are
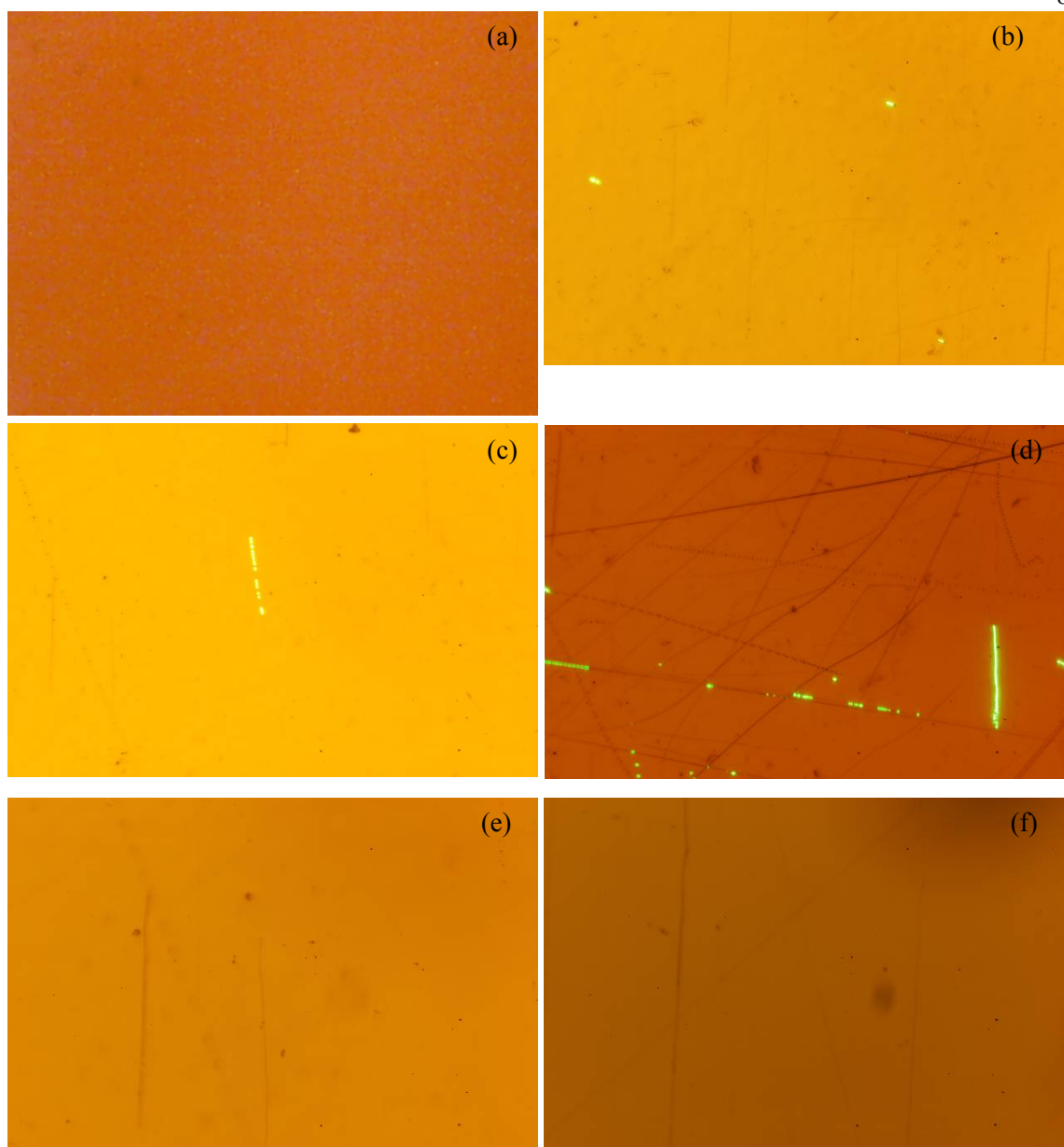
FIG. 4.14. Optical images of Kapton HN on VD films.
Films are backlit with green light to emphasize pinholes and cracks in the Olympus BX41 microscope images. (a) Images taken using the Intel QX3 microscope show an image size of 2.3 mm (h) x 3.1 mm (w) taken at 60x magnification. (b-d) Images taken using the Olympus BX41 microscope show an image size of area 0.64 mm (h) x 0.98 mm (w) taken at 150x magnification. (e) Images taken using the Olympus BX41 microscope show an image size of 0.32 mm (h) x 0.49 mm (w) taken at 300x magnification. (f) Images taken using the Olympus BX41 microscope show an image size of 0.13 mm (h) x 0.20 mm (w) taken at 750x magnification.
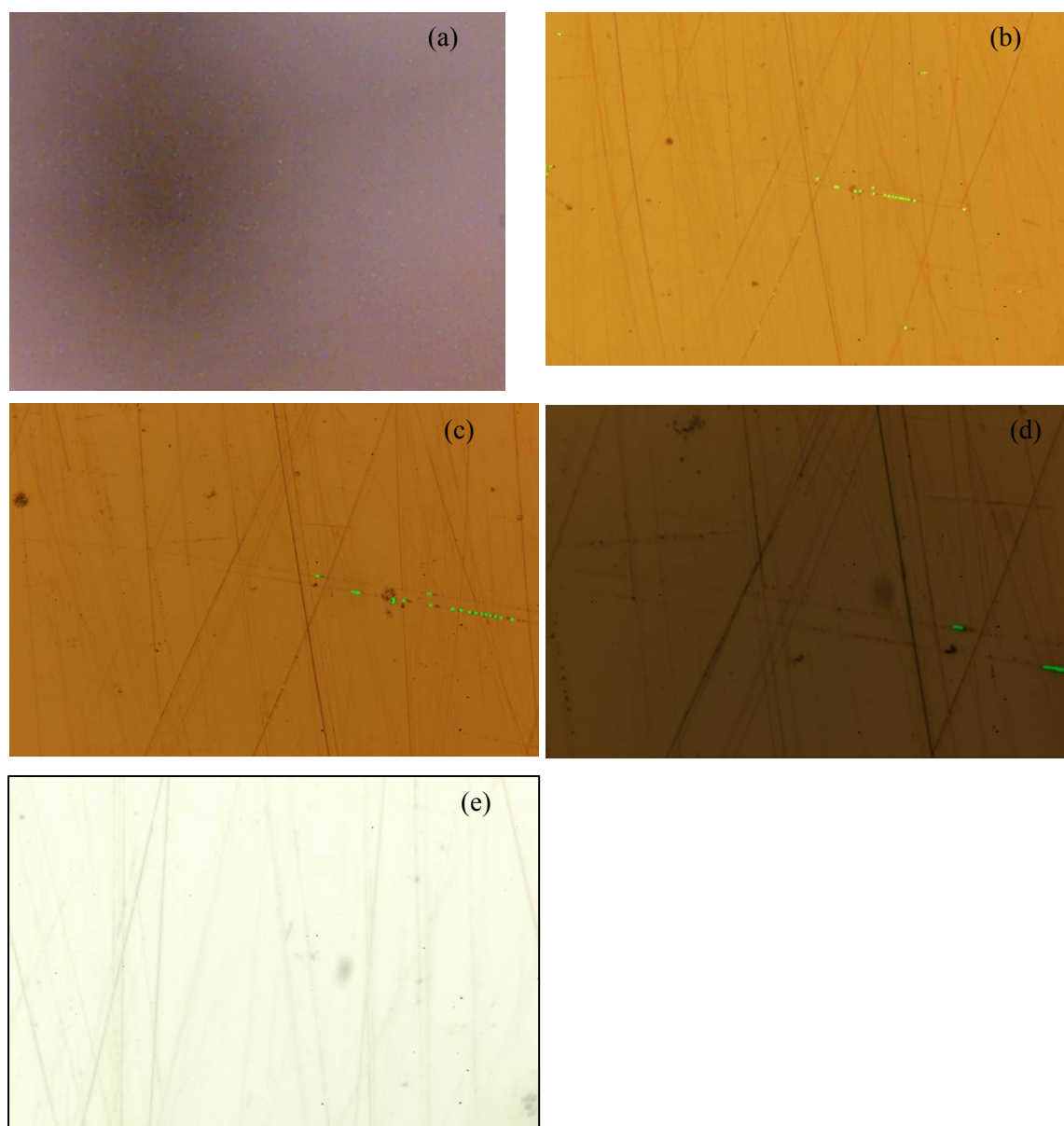
FIG. 4.15. Optical images of VDA side of Kapton HN film.
Films are backlit with green light to emphasize pinholes and cracks in the Olympus microscope images. (a) Images taken using the Intel QX3 microscope show an image size of 2.3 mm (h) x 3.1 mm (w) taken at 60x magnification. (b) Images taken using the Olympus BX41 microscope show an image size of area 0.64 mm (h) x 0.98 mm (w) taken at 150x magnification. (c) Images taken using the Olympus BX41 microscope show an image size of 0.32 mm (h) x 0.49 mm (w) taken at 300x magnification. (d) Images taken using the Olympus BX41 microscope show an image size of 0.13 mm (h) x 0.20 mm (w) taken at 750x magnification. (e) Images taken using the Olympus BX41 microscope show an image of size of 64 μm (h) x 100 μm (w) taken at 1500x magnification.

measured with ~5 sec of neutralization between each pulse using low-energy electron flooding. Similar series of pulses at fixed incident energy, taken without neutralization, constitute so-called electron yield decay curves. SE emission spectral data are also presented taken with a DC beam for Kapton HN. These processes have been described in detail in Section 3.1.

4.2.2.1 SE Yield

The total, SE and BSE stimulated electron yield are shown in FIG. 4.16. These data are exceptionally smooth and represent the cleanest insulator data ever taken on the pulsed MPG system. An attempt was made to compare these data with data presented in the literature, but no comparable data could be found. This suggests that these data are the only data available for electron yield on Kapton HN. This could be due to the extreme difficulty in measuring electron yields of high-resistivity materials, owing to their charging susceptibility.

The total and BSE yields for Kapton HN with curve discretized into several distinct areas (zone 1-5) and points (A-C) are shown in FIG. 4.17. As was done in Section 4.1.2.1 with CP1 measurements, we take each zone in turn and apply what we know about penetration range, internal charge distribution and how that charge will affect the yield. This allows us to start to speculate about the deviation of the measured (charged) yield from the ideal uncharged (green curve in FIG. 4.16a) yield.

We start by identifying the zones and points of interest in FIG. 4.17. In zone 1 below $E_o < E_I = 31$ eV SE yield is not affected by charge. At these energies the IMFP of the SE is greater than the incident electron IMFP. Also, below 50 eV BSE cease to be defined and $\sigma = \delta$. In this energy range the DDLM is not an accurate model. At point A (namely $E_I = 31 \pm 5$ eV) there is no net charging by definition. Here E_I is less than the minimum in the IMFP curves in FIG. 4.17 so DDLM is again inapplicable. Zone 2 spans from above E_I to below E_2 and makes up the section of the total yield curve that results in positive charging. As such, the measured total yield curve could be depressed due to positive sample charging and the subsequent reattraction of some SE's,
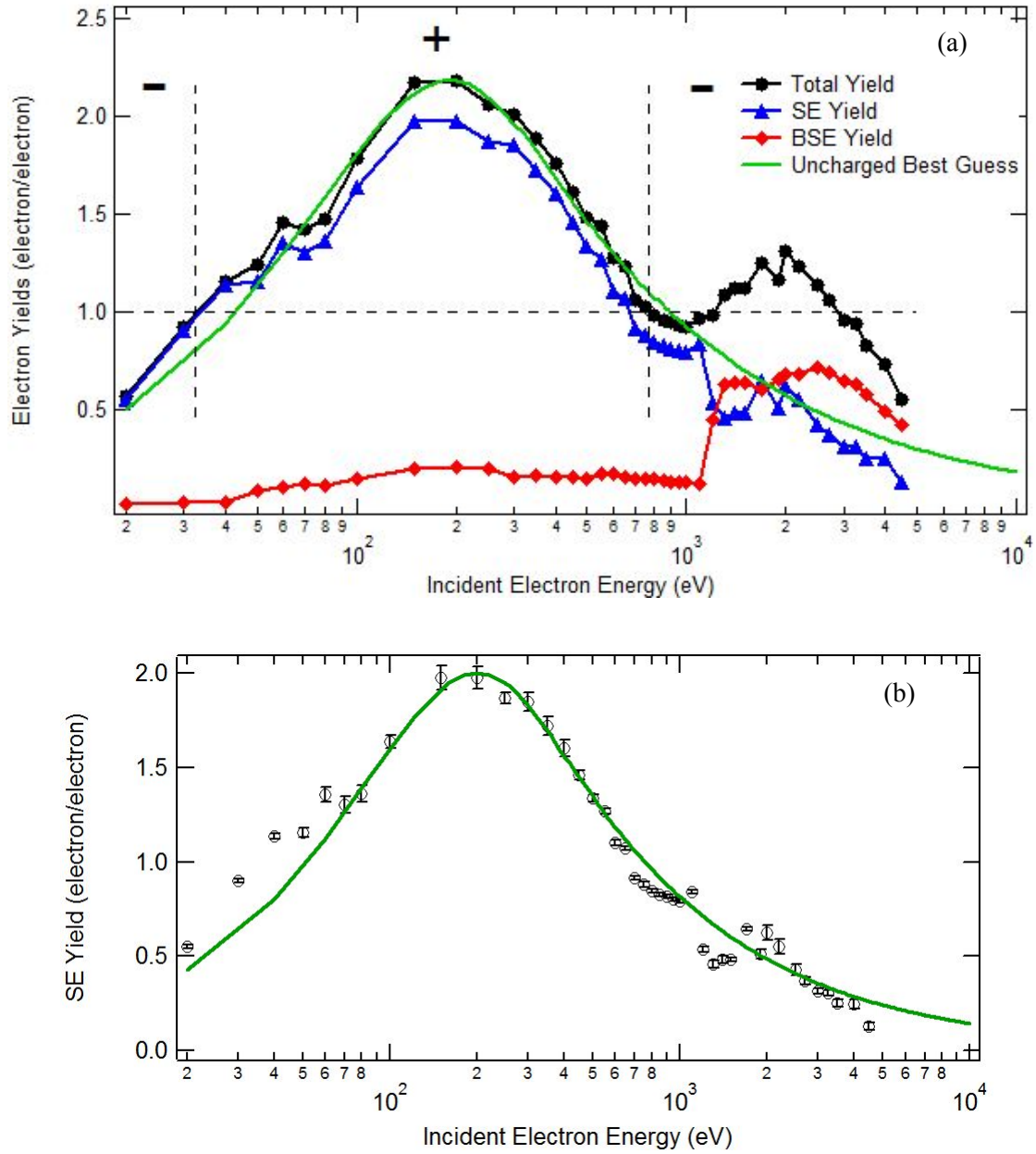
FIG. 4.16. Electron yield curves for Kapton HN.
(a) Total, SE and BSE yields as a function of incident electron energy on Kapton HN. (b) Electron-induced SE yield curves. Electron yield as a function of incident electron energy, with NASCAP 5 parameter fits. Note the logarithmic energy scale.
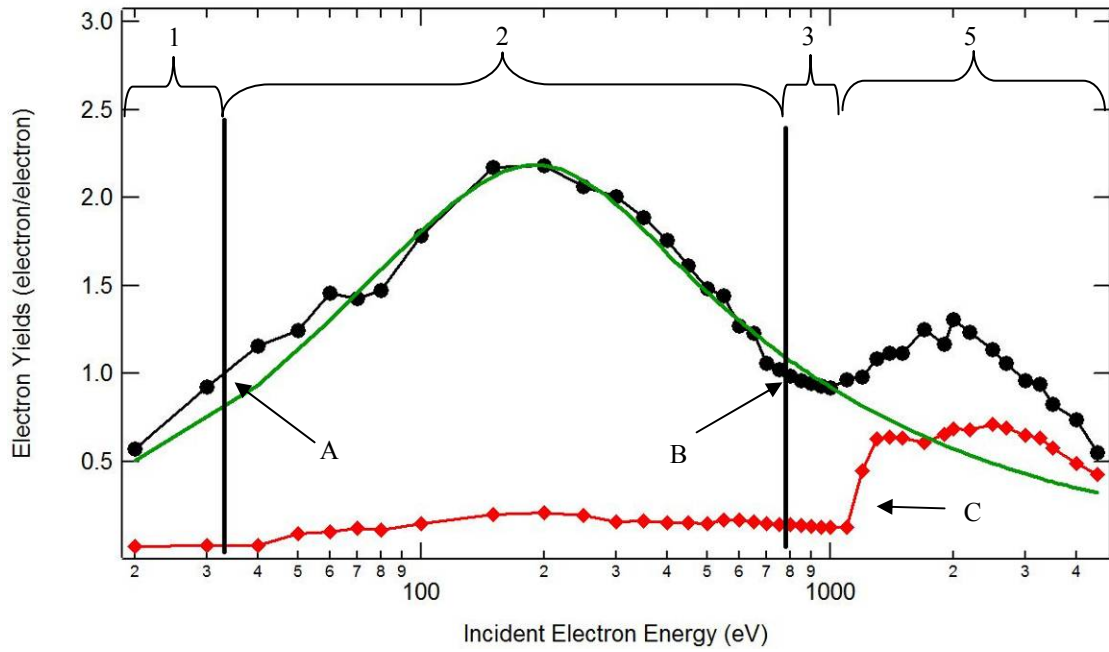
FIG. 4.17. Total and BSE yield from Kapton HN showing discrete charging zones.
Black dots indicate the total yield and the red diamond is the BSE yield. Zones and points of interest are marked

but we see little or no evidence of this in the Kapton HN data. The BSE yield in the section is unaffected by the relatively small positive surface potential. Point B (namely E_2=775±10 eV) is accurate as there is no net charge accumulating on the sample and $\sigma=1$. The BSE yield at this point is also accurate. Zone 3 for $E_2<E_o<\sim1000$ eV follows the idealized green curve despite ineffective charge neutralization of negative charge accumulation; no increase in σ above the green line is seen. It might be that the internal electric field in Kapton is insufficient to excite electrons from (presumably deeper) traps in Kapton HN, in contrast to what was seen in CP1 (see Section 4.1.2.1). At about 1100 eV, at point C, there is a large jump up in the BSE yield and a nearly commensurate drop in the SE yield. This occurs as the peak in the electron emission spectrum (nominally at ~4 eV) is accelerated to greater than 50 eV by a large negative surface potential. That is, SE from the depletion region are now being measure as extra BSE as they meet the criteria of having energies over 50 eV. There is no evidence of zone 4 in this material as there

is no decrease in SE below the SE to BSE shift. In zone 5 in the range of 1100 eV <E<4000 eV

total yield is above the true yield as extra SE's from the depletion region (surface side of the

negative deposition layer at the penetration depth R) that are accelerated out due to the large

electric field formed by the negative layer at R. Near the end of zone 5 total and BSE yields begin

to return to the idealized uncharged green curve indicating that the yield is close to returning to its

uncharged value we would see in zone 6 but did not quite get there. This could be due to a

physical breakdown in the material, that is to say the surface voltage V_s exceeds the voltage for

electrostatic breakdown V_{esd} typically 278 MV/m or ~278 V for Kapton HN. Higher energy data

must be taken to confirm that the measured yield is indeed reconverging on the true yield curve.

Values obtained for the SE yield parameters for Kapton HN have not been measured

independently by other groups, but these data are in good agreement with those in Thomson

(2004). The best fit to the SE yield curve was provided by the NASCAP five parameter SE yield

model. For this model, values for the five parameters are as follows; δ_{max}=(2.00 ± 0.01)

electrons/electron, E_{max} = (0.20 ± 0.01) keV, n_1 = (1.7 ± 0.1) and n_2 = (0.47 ± 0.01), b_2/b_1 = (4.84

± 0.02).

4.2.2.2 BSE Yield

Measurements of the BSE yield were made using the pulsed system, due to initial

problems with surface charging of the samples. Figure 4.18 shows the BSE yield as a function of

incident electron energy, with energy on a log scale. The plot includes the NASCAP one

parameter fit and an extended three parameter fit to the BSE yield curve (Levy *et al.*, 1985;

Mandell *et al.*, 2001). Values for these fitting parameters are listed in Table 4.3.

The fitting parameters for the extended fit of the maximum value of the Kapton HN BSE

yield was found to be (0.22 ± 0.02) electrons/electron at the incident electron energy of

(0.20±0.01) keV. The green line in FIG. 4.18 is an estimate of the BSE yield without charging
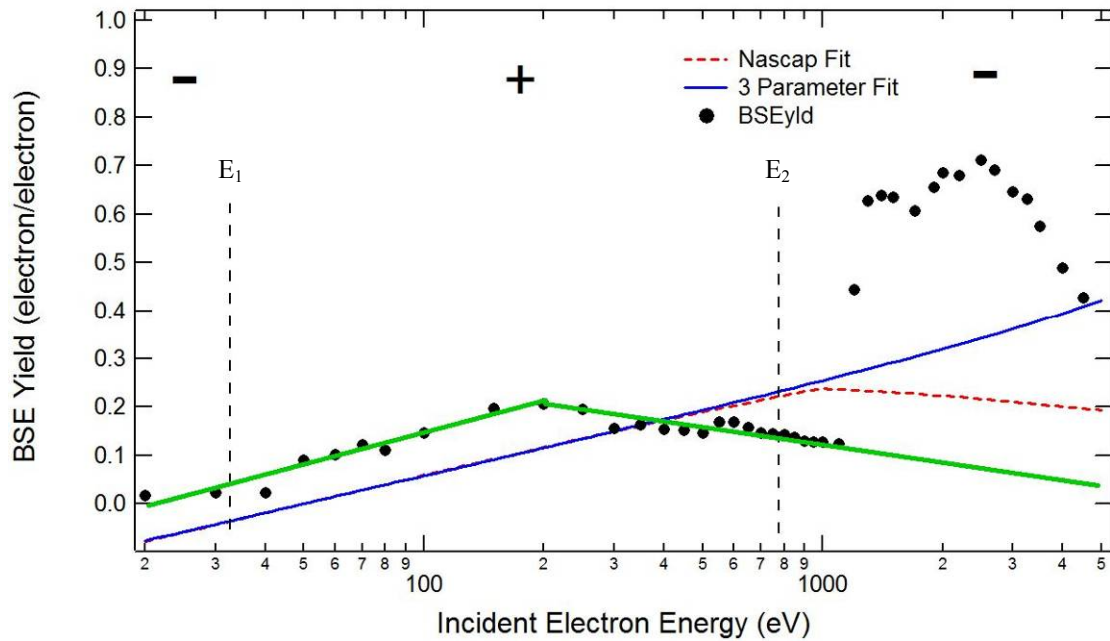
FIG. 4.18. Backscattered electron emission yield curves for Kapton HN.
The plots include both the NASCAP one parameter fit and an extended three parameter fit to the
BSE yield curve. Note the logarithmic energy scale.

effects. The three parameter and NASCAP fits are plotted in this figure are usually a good fit, but

it is distorted here because it is not able to account for the SE→BSE shift.

The larger shifts in BSE yields observed at ~1100±50 eV occurs when the charge on the

sample builds up to over ~45 V and the SE in the main peak of the SE emission spectrum acquire

enough energy to be measured as BSE. The fact that this occurs almost 300 eV above E_2 can be

attributed to either the very small charge fluence used in the pulsed yield measurements, to the

relatively rapid decay of charge (see Section 2) possibly from RIC, or a combination of the two

effects. A full discussion of this effect cannot be had outside the context of SE and total yield. As

such, please refer to Section 5.1.2.1 for a full explanation of this phenomenon and it

consequences.

4.2.2.3 Electron Emission Spectra

Measurements of the electron-induced electron emission spectra were made using a low-energy electron gun operating in the continuous mode at incident energies of 60 eV to 100 eV with a beam current of ~ 5 nA and a ~1 mm diameter beam spot and a beam current density of ~50 pA/cm^2. Limited spectra were taken on this material, but what is shown here is a good indication of the general behavior of Kapton in the region of 60 eV$\leq E_o \leq$100 eV. As shown in FIG. 4.19, a second electron emission peak begins to emerge at $E_o \leq$ 90 eV, this is an indication that E_1 has been crossed and that the sample is charging to negative potentials at 90 eV incident energies and below. Using the inner grid peak as a bench mark, the sample potential can be estimated at -12V at maximum with E_o=80 eV. One might expect the sample to continue to charge negatively as the beam becomes lower in energy, but at this point V_s is a substantial fraction (15 %) of the incident energy. This results in a significant slowing of the PE's and their possible deflection. Limited data were taken on this material, so it was not possible to develop a full analysis using emission spectra. In particular, spectra at energies near E_2 might help determine its value. E_1, as determined by the yield curve, gives a value of 33±5 eV and the spectral method gives a value of $\leq$ 90 eV. This inconsistency is due to the fundamental differences in the measurements, namely, the pulsed nature of the yield system and the DC beam used when taking spectra. Given this, the agreement for the value of E_1 is rather good.

4.2.2.4 Decay Curve

To study the effect of charge accumulation on the electron yield, an electron yield decay curve was measured for Kapton HN, as shown in FIG. 4.20. An incident energy of 400 eV was used. Since this energy is near the maximum electron yield of 200±25 eV, and between the crossover energies, with an uncharged yield greater than unity, the sample is expected to charge positively.
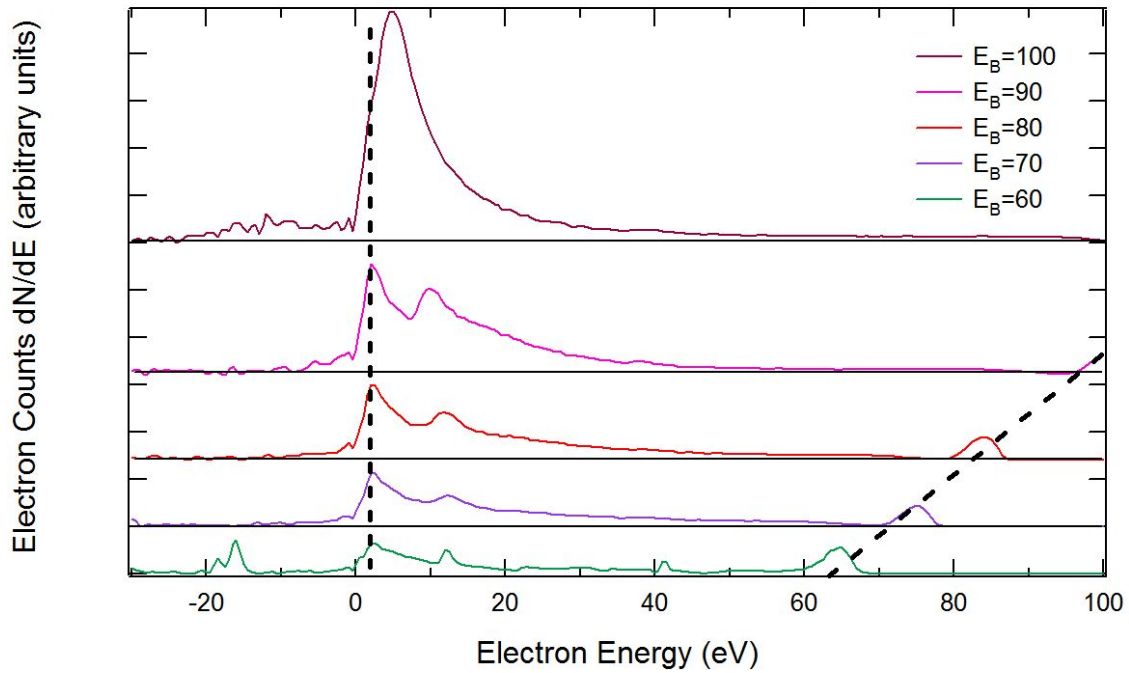
FIG. 4.19. Electron emission spectrum of Kapton.
Data acquired at incident energies of 60 eV (bottom), 70 eV, 80eV, 90eV, 100 eV (top). Here E_1 is assumed to be around 95 eV and as E_b decreases the sample begins to charge negatively as evidenced by the emergence of the sample peak and its shift to the right as the negative potential increases.

As the sample charges to higher positive values, more emitted electrons are reattracted to the surface, which is expected to cause the yield to asymptotically approach unity. In FIG. 4.20a, there is certainly an asymptotic limit, but it does not have a value of one; rather, it has a value of σ=1.08. Data in FIG. 4.20a were taken after many measurements of the total yield had been taken with all discharge methods (discussed in Section 3.2.1) were employed. This suggests that after a full day of measurements, there remains some deep space charge that our discharge methods do not adequately dissipate.

To test this theory, a second curve was taken (as shown in Fig. 4.20b) that shows the same curve after the material had been heated to 60° C for 6 hr and then allowed to cool to room temperature. Heating the material increases its bulk conductivity and enhances the material's ability to dissipate charge (Brunson, 2009). This phenomenon is discussed in greater detail in
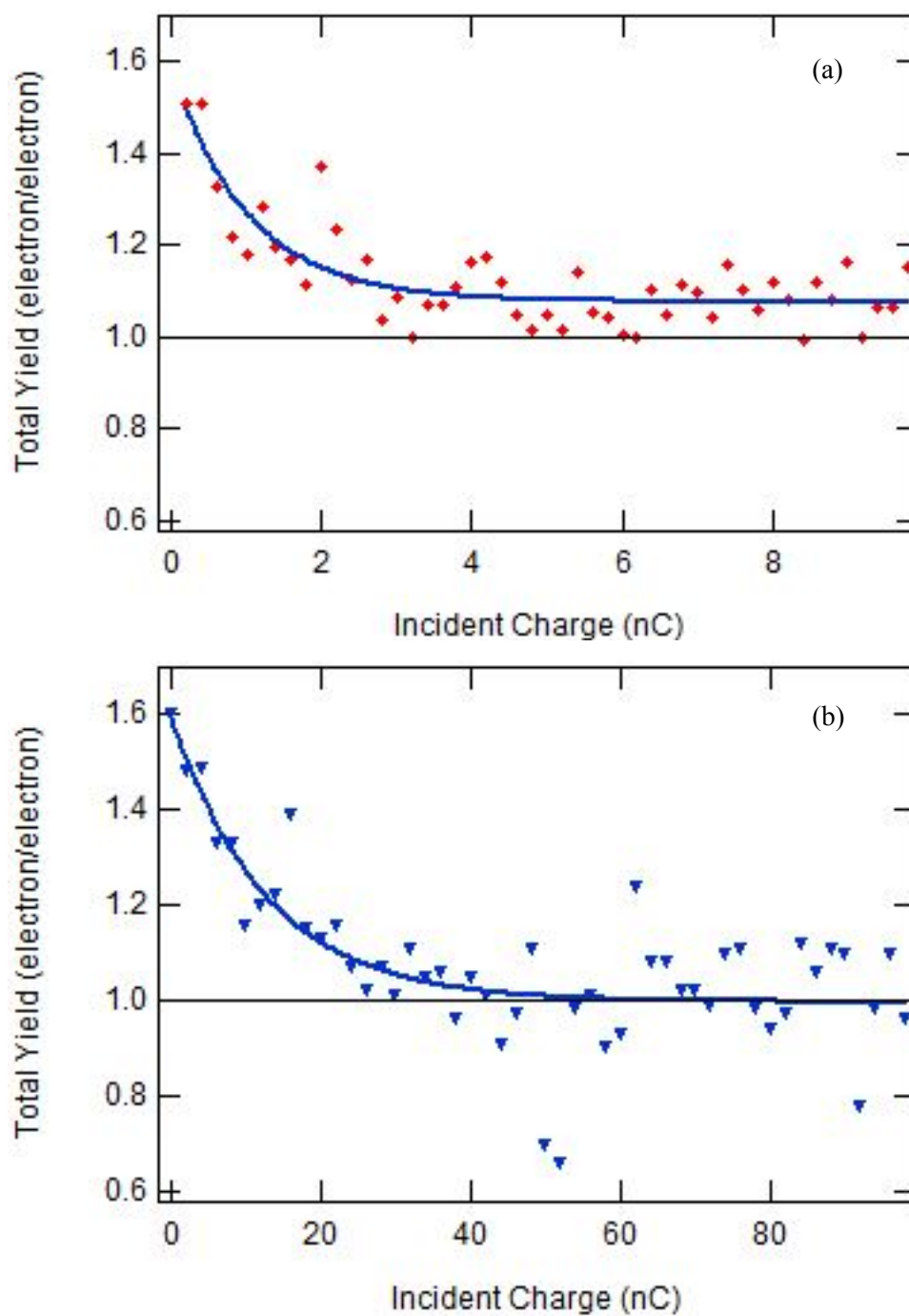
FIG. 4.20. Decay curves taken for Kapton HN at 400 eV incident electron energy.
(a) Decay curve charged very quickly and did not approach unity. (b) Data after being subjected to prolonged charge/discharge cycles.

Section 4.3.2.2. Shown in FIG. 4.20b is an asymptotic approach to unity, as is expected for a sample with little or no stored space charge. Also note that it takes ~40 nC to reach the yield limit of one, a more expected value base on DDLM estimates of a surface potential of 20 V from Eq. (2.19), whereas the FIG. 4.20a takes only ~4 nC (DDLM estimated value of 2 V) to reach its elevated limit.

It is not entirely clear why the unheated decay curve does not obtain a limit of one. Other yield data that were taken on the sample prior to this curve in FIG. 4.20a all had a yield greater than one and should have resulted in net positive charging. If the discharge methods where fully ineffectual, there would have only been a flat curve at the asymptotic yield limit. Such results might be due to internal (deep dielectric) charge layering in the material that has not been taken into account in this discussion. One can speculate that this internal charge, results from the high-energy irradiation used in the yield test pulses, just prior to when the discharge from the flood gun begins. Flooding will only eliminate the near-surface positive charge region leaving some implanted negative charge behind at a greater depth R. Since the majority of the charge is positive only a small amount of negative charge is left behind and it would take many pulse/discharge cycles to reach a significant charging level. This is a hand waving argument; direct measurements of the surface potential proposed in Section 5.1 will determine the validity of this hypothesis.

Until such time as this phenomenon has been fully understood, we have shown here that heating the material is effective at dissipating charging. As such, the sample is heated for 6 hr to ~333 K each night after every full day's measurements.

4.2.2.5 Dose Decay Curve

Up until this point, it has been assumed in all the data analyzed that the ~10^6 electrons used in the probe pulse is not large enough to cause significant charging. Measurements taken to support this assumption used the following method. Fifteen pulses at a single incident energy between the crossover energies were taken and a mean and standard deviation of the yield were

determined. All dissipation techniques where employed and the total yield did not decay as in a decay curve. The first set of pulses were tuned at the lowest possible incident flux of 20 fC per 5μs pulse and a 1.7 mm diameter spot size. This corresponds to a charge density of ~1.2 pC/cm^2 - pulse. During a ~5 μs pulse this is an average current density of ~230 nA/cm^2 or a particle flux density of ~$1.5 \cdot 10^{12}$ electrons/cm^2·s and a dose rate of ~$4 \cdot 10^6$ rad/s in the sample region between the surface and range (assuming a range of ~9 nm at 200 eV incident energy).

This is an unrealistically high dose rate, however, as it does not include the material response time to the energy injected into the sample surface layer during the short ~5 μs pulse. This response time is evident in the time it took a sample to come to equilibrium after a beam was turned on in RIC experiments (Dennison *et al.*, 2007). The RIC decay time was typically ~100 s for a Kapton sample to exponentially approach equilibrium. It is well known that pulsed beam used in accelerators with repetition rates of $\geq 10^2$ cycles/s can be accurately approximately by effective dose rate equal to the average dose over the full cycle (Dennison *et al.*, 2009b). What is not well known is at what extended cycle time this approach breaks down.

A lower bound on the dose rate in charge decay experiments can be calculated assuming the energy from a single pulse is spread over the full repetition period of typically ~5 sec, which is small compared to the RIC decay time. Under this assumption, the average current density is $2.3 \cdot 10^{-13}$ A/cm^2, the particle flux is ~$1.5 \cdot 10^6$ electrons/cm^2·s, the dose rate is ~4 rad/s (assuming R=9 nm at 200 eV), the RIC is 10^{13} (Ω·cm)$^{-1}$ and the RIC decay time is ~3 s. It is important to recognize that charge dissipation at this lower bound is still completely dominated by RIC effects in Kapton and that the decay time is comparable to the pulse cycle time of 10's to 100's of pulse cycles. An interesting and important test of these conjectures would be to repeat experiments such as shown in FIG. 4.20, with different effective dose ratios, longer and shorter times between pulses and pulse widths, and with higher and lower beam current density and energy.

Once finished, the incident flux was increased slightly by turning up the electron gun filament. After 30 min to allow the gun to stabilize and come to thermal equilibrium, another set of data were taken. This sequence was repeated until the electrometers reached saturation at ~700 fC/pulse. These data are shown in FIG. 4.21a at two different energies, 200 and 600 eV. The arrow in FIG. 4.21a indicates the dose used in the yield curve taken in Section 4.2.2.1 shown in FIG. 4.16. The yield at 200 eV from the yield curve is 2.2 ± 0.1 at a dose of ~100 fC; this is in good agreement with the yield of 2.1 ± 0.2 from the 200 eV decay curve at ~100 fC. The agreement is also very good for the 600 eV incident beam with a pulsed yield value of 1.5 ± 0.1 and a decay curve value of 1.5 ± 0.2

If the pulse were not causing significant charging, we would expect a plateau on the left low fluence side of the dose decay curve. This is obviously not the case and suggests that if the pulse could be lowed further the yield would continue to climb. The expected dose decay curve is expected to have a shape as determined by the SE emission curve calculations as described in Section 2 and shown in FIG. 4.21b. Unfortunately, it is not possible to lower the incident pulse because of the noise of system. This was the first indication that the other methods described in Section 3 were needed.

4.2.2.6 Dose Yields

The dose decay curves described in the previous section indicate that the yield will change as a function of incident flux in the probe beam. To verify that this is true, yield curves were taken at several incident fluxes: 110 ± 50 fC/pulse, 370 ± 30 fC/pulse, and 1.0 ± 0.05 pC/pulse, all with ~5 μs pulses. For this to be effective, it was important that the incident spot size be constant throughout the full energy range of the gun. This required new settings for the Staib gun, at every incident energy, so the spot size would remain set at an arbitrary 1.7 ± 0.1 mm FWHM. Refer to Section 4.2.4 for details regarding the measurements of the spot size and the subsequent gun calibration. The flux density for 110 ± 50 fC/pulse is 5 ± 2 pC/cm^2 with a 40%
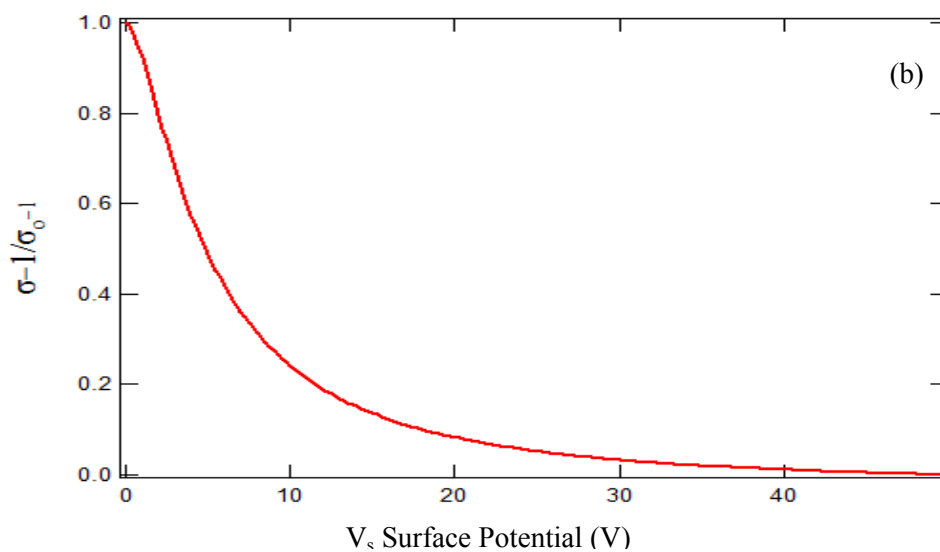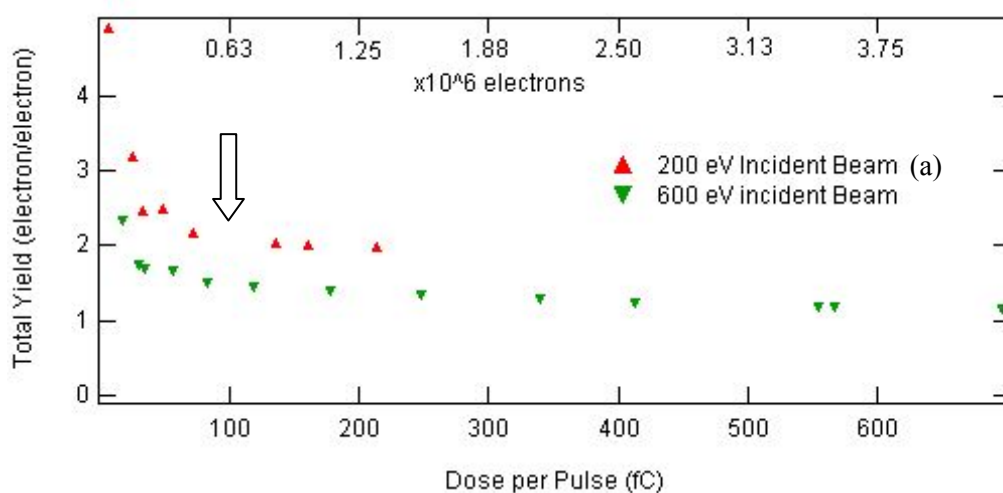
FIG. 4.21. Decay curve and fractional SE recapture of Kapton HN.
(a) Dose decay curve was taken on Kapton HN^{TM} by adjusting the number of electrons contained in the incident pulse, keeping all other parameters constant. In this range, a change of only ~4x10^4 el/mm^2 produces a ~40% increase in the yield. Dose decay curves are shown for both 200 eV (red) and 600 eV (green) incident energies. (b) SE decay model derived from model for SE emission spectra.

error. With the electron gun set to 370±30 fC/pulse, the flux density is 16±1 pC/cm^2 with a 6%

error. At 1.0±0.05 pC/pulse the flux density is 44±2 pC/cm^2 with a 5% error. The error in these

measurements is completely dominated by the error in the flux measurement; the error in the

FWHM is trivial by comparison.

The yield curve results of the measurements taken at 110±50 fC/pulse incident fluence

are shown in FIG. 4.22a. These data were taken at the lowest fluence and show a σ_{max} of 3.9±0.1.

The plot in FIG. 4.22b shows data taken at an intermediate flux of 370±30 fC/pulse and a

suppressed σ_{max} of 2.2±0.1. Only a partial yield curve was taken at the maximum flux of 110±50

fC/pulse, but the curve (FIG.4.23a) shows a maximum total yield of ~2, a further suppression of

the yield from the low flux. The SE yield from each of these three curves plotted together in

FIG.4.23b shows the suppression of the yield as the flux in the probe pulse is increased from low

to high (shown as top to bottom curves, respectively). It is interesting to note that the pulse flux

appears to dramatically affect the yield in the positive charging region. between the crossover

energies (Zone 2), but seems to have little effect on the negative charging zones 1 and 3. This is

most likely due to our inability to dissipate negative charge. As a result the charge accumulates

over many pulses to a steady state and the flux of the individual pulse is not as important. For

example, if, at the low flux, it takes 10 pulses to reach equilibrium, then, at the high flux it would

take only one pulse to reach equilibrium. This makes little difference as the yields are averaged

over 30 pulses and the difference would primarily appear as an increase in the statistical error.

There are also BSE yields data from all three runs plotted together for comparison in FIG.

4.24b. It is not expected that incident energies between the crossovers (positive charging) will

affect the BSE yield because any energy gained from the electric field is lost as the BSE leaves

the sample. However, it can be seen that there is a modest change for energies between 200 eV

and 700 eV and between ~1100 eV and 5000 eV. The data for the lowest and highest fluxes,

(black dots and the blue triangle), respectively, are very similar, but differ from the mid-range run
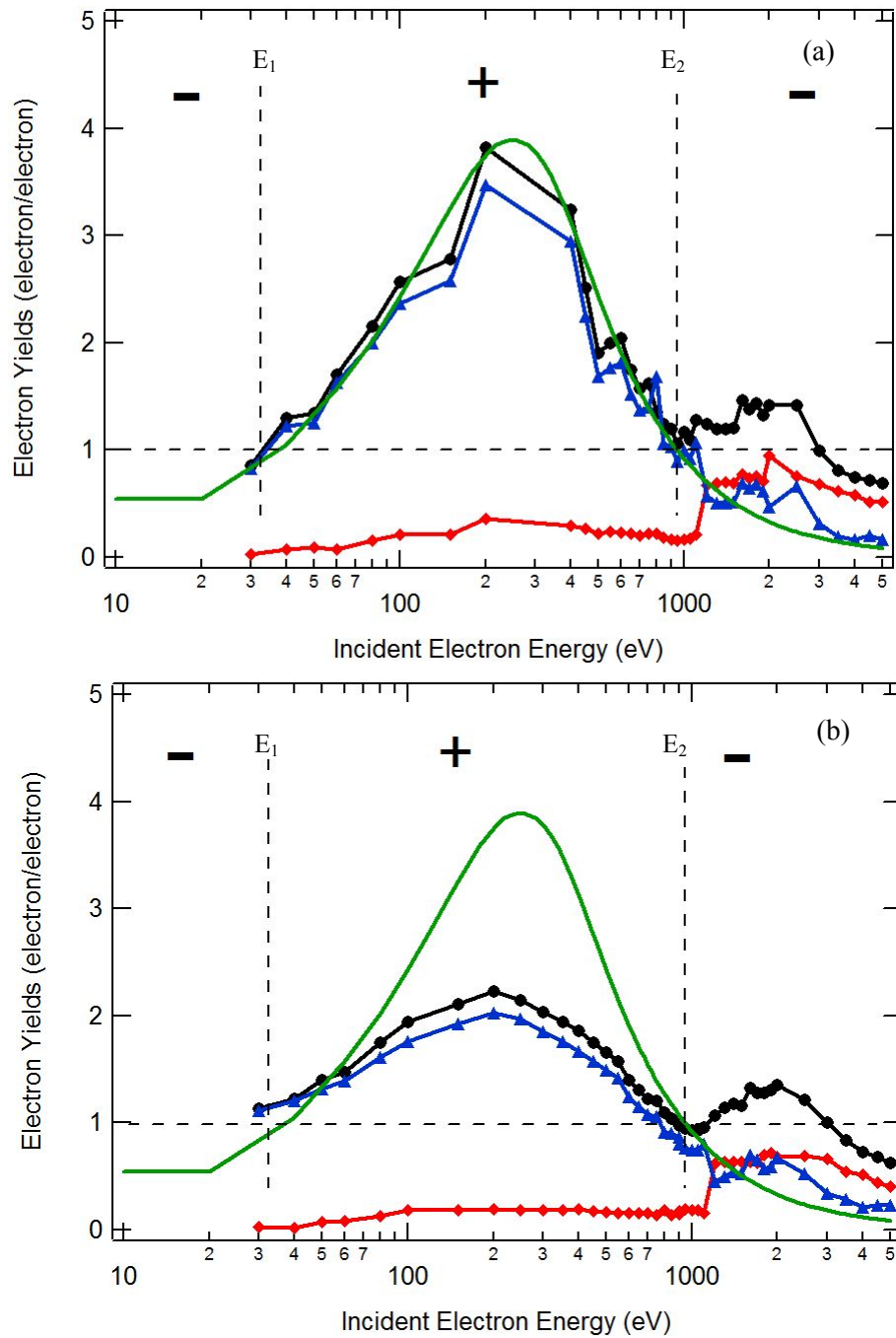
FIG. 4.22. Yields of Kapton at 2 fluxes.
(a) Yield curves taken on Kapton HN with an incident flux of 110±50 fC/pulse. (b) show the Yield curves taken with an incident flux of 370±30 fC/pulse. All other parameters were kept constant and only the incident flux was changed. These fluxes were maintained over the entire energy spectrum. Black dots indicate total yield. Blue triangles indicate SE yield. Red dots indicate BSE yield.
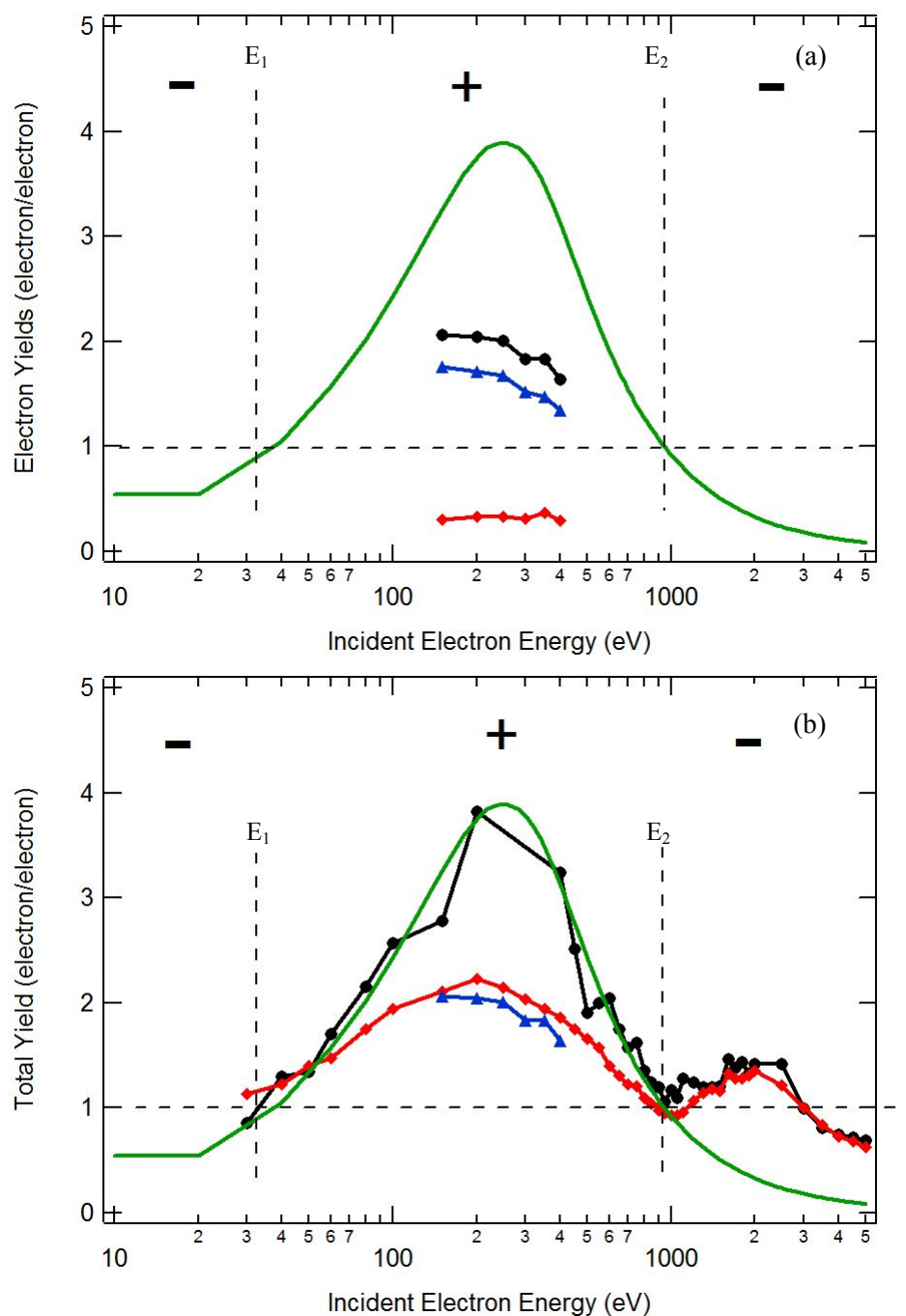
FIG.4.23. Total yield as a function of dose comparison.
(a) Partial yield curves taken on Kapton HN with an incident flux of 1.0±0.05 pC/pulse. A full spectrum of yields was not able to be taken at this flux. (b) Comparison of the total yield curves over the energies at various fluxes. Black dots are yield taken at 110±50 fC/pulse, red diamonds are 370±30 fC/pulse, and blue diamonds are at a flux of 1.0±0.05 pC/pulse. Black dots indicate total yield. Blue triangles indicate SE yield. Red dots indicate BSE yield.
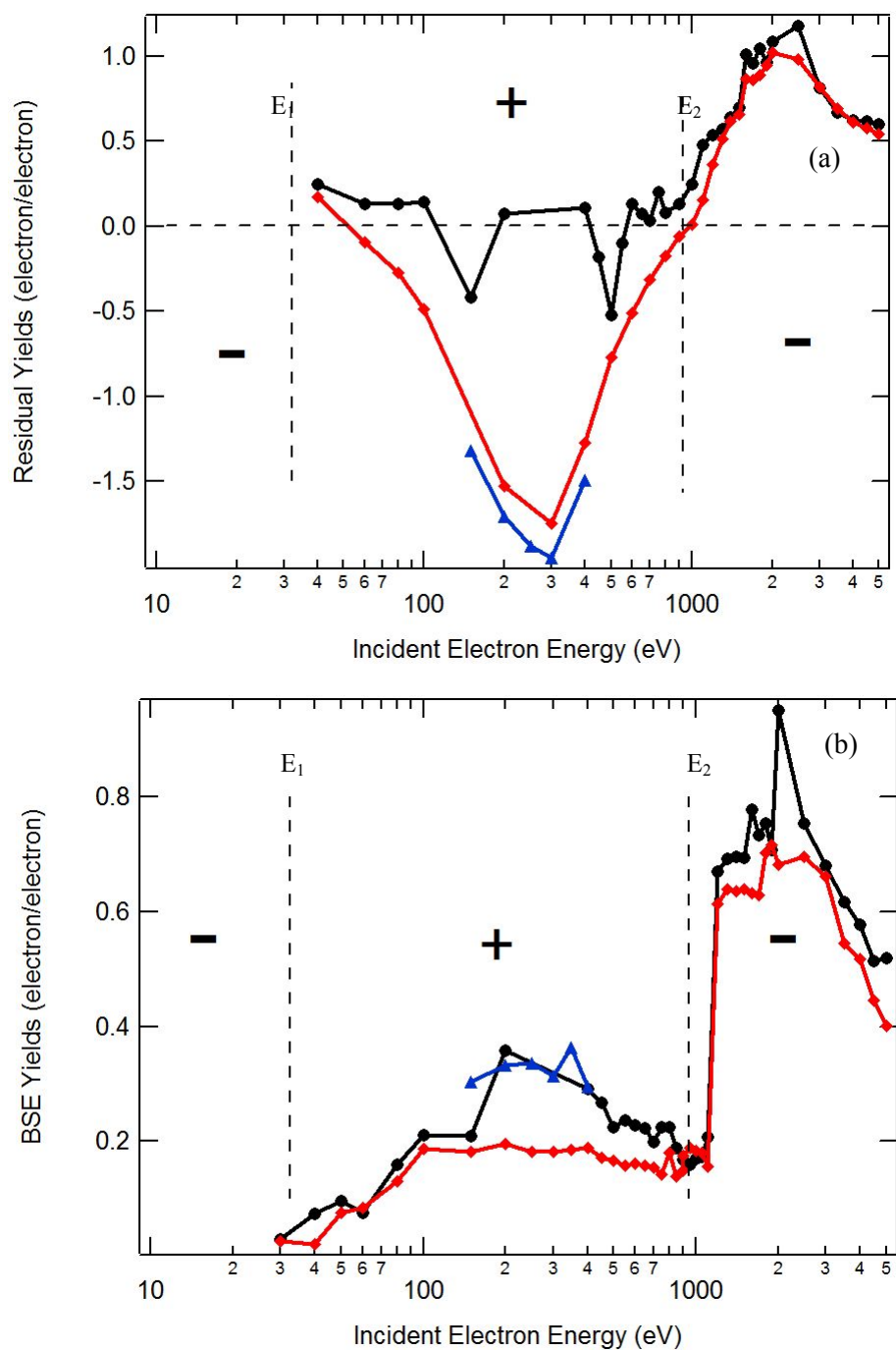
FIG. 4.24. Residual of uncharged curves and BSE yields.
(a) Difference in total yield from the green idealized (green curve) for all three fluxes. (b) Comparison of the BSE yield curves at various fluxes. Black dots are yield taken at 1.0±0.05 pC/pulse, red diamonds are 370±30 fC/pulse, and blue diamonds are at a flux of 1.0±0.05 pC/pulse. Black dots indicate total yield. Blue triangles indicate SE yield. Red dots indicate BSE yield.

(red diamond). It is unclear why the highest and lowest fluxes are in such good agreement, but the intermediate run is not. This may be an anomalous result and would need to be repeated to verify the result. It is interesting to note that the highest and lowest flux yield curves show the same jump in the BSE to SE ratio at ~1100 eV. As stated in the paragraph above, this is most likely due to our inability to dissipate negative charge. As a result the charge accumulates over many pulses to a steady state and the flux of the pulse is not as important.

4.2.3 Irradiated Kapton HN

During the course of this investigation, many mistakes have been made, but not all of them bad. The measurements taken on Kapton up to this point have been on one sample with special care taken to do the most destructive tests last. The following has been determined to be the order which the tests were performed. Yields with energies $E_1 < E_b < E_2$ are preformed first, followed by $E_b < E_1$, then decay curves. These were followed chronologically by the test deemed most destructive; yields with energies $E_b > E_2$ and finally DC spectra. These tests were done last because it was assumed that the material undergoes permanent structural changes as a result of the high electric fields these measurements induce. The data presented in this section were taken on the same Kapton sample after all of measurements were taken in Section 4.2.2. As such, the sample had undergone significant radiation damage and possibly electrostatic breakdown. This is not meant to be a complete treatment of the subject, and does not represent all the data in this archive. This is simply intended to document the fact that a wealth of data exists and needs further analysis in the future. Sim presents some related theoretical treatments of the effects of trap production due to irradiation on electron emission, conductivity, surface voltage decay and electro static discharge (Sim, 2010).

4.2.3.1 Electron Yield

It is very difficult to quantify this discussion without a clear understanding of the sample history so that we might put clear bounds on the total electron dose and internal potential this sample has been subjected to. To be clear, all the data from Sections 4.2.2.1-4.2.2.6 was taken on the same sample as the data presented in this section. There was a one week period between when these data were taken and when the data from the previous section were taken. As a minimum, the Kapton HN sample had been subject to 10^9 C of electron fluence at energies ranging from 30 eV to 5 keV during the course of the pulse yield measurements. This irradiation is inconsequential, given that the sample was subject to a 1 nA DC beam for ~4 hr (~1 μC) at energies up to 650 eV while taking emission spectra. This later punishment is assumed to have caused material breakdown.

The most obvious difference seen in the damaged and undamaged yield curves in FIG. 4.25 is that the point at which the BSE yield jumps up due to SE being accelerated above 50 V is significantly lower. This point occurs at ~800 eV in the irradiated sample as opposed to ~1100 eV in the undamaged sample (FIG. 4.25a).

One explanation for this might be that there is deep dielectric charging in the sample. Given the bulk dark current conductivity of Kapton (in the range of 10^{-19} to 10^{-20} $(\Omega\text{-cm})^{-1}$) it can take weeks to months for this type of charge to dissipate (Dennison, 2008). The sample was taken out of the chamber after its initial set of measurements and exposed to air for a week before being reintroduced into the vacuum chamber. In light of this, it's not clear if the sample would have been able to retain its charge in the humid, high pressure environment, both of which act to accelerate charge dissipation. However, electret materials such as Kapton and Teflon are known to store charge for long periods of time (Dennison *et al.*, 2003a). Thus, the idea of residual charge may or may not explain the quicker buildup of negative potential seen in the irradiated sample.
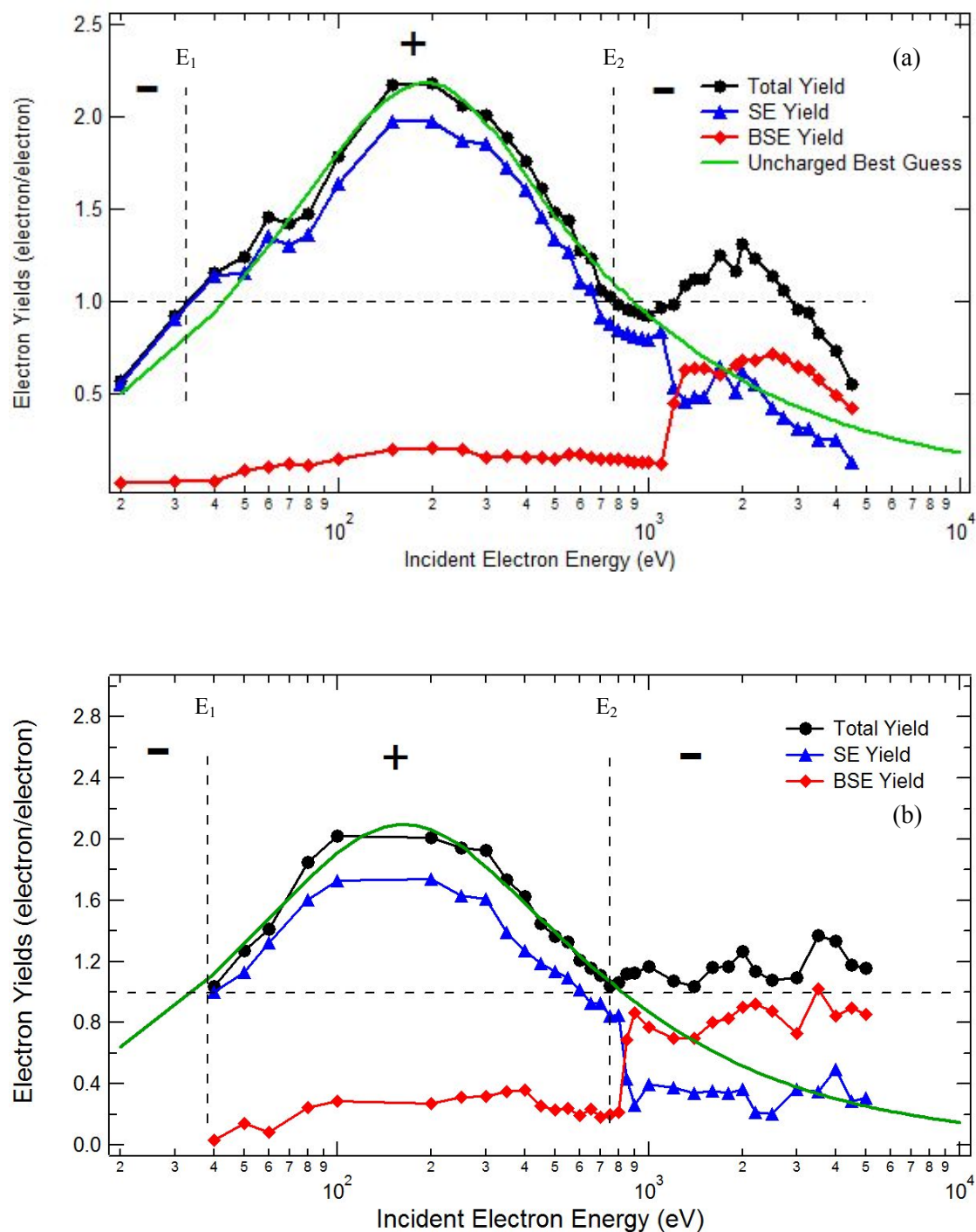
FIG. 4.25. Electron yields of irradiated Kapton HN.
(a) Plot of undamaged Kapton. (b) Data from the same sample, but after it has been abused by a full suite of measurements. There are significant changes in the material. Most notably the BSE→SE shift occurs at ~800 eV in the irradiated sample and ~1100 eV in the unirradiated.

Another explanation is that high electron fluence used in the spectral measurements caused damage to the sample, by generating additional traps states in the material due to radiation damage. Exposure from the 1 nA DC beam at E_o=650 eV for ~4 hr produces a accumulated dose of 10^7 rads in the surface layer down to the penetration depth of R=800 nm. Radiation damage studies have shown that polymers such as Kapton show measurable structural damage at doses above 10^8 rad. Fredrickson (Fredrickson and Dennison, 2003) has speculated that radiation damage, in the form of defect generation, may become evident in electron transport at lower fluxes, as low as 10^7 rad.

If the high radiation exposure from spectral measurements prior to acquisition of data in FIG. 4.25b created significantly more defect trap states, built up space charge would be more efficient and more space charge could be stored. Higher efficiency in creating space charge would shift the SE→BSE transition to lower energies. Indeed, this transition in FIG. 4.25b is shifted to ~800 eV, just slightly above E_2=750±20 eV.

This does not provide a complete treatment of the topic, but does offer some tantalizing clues to the effects that radiation damage might have on sample charging. More analysis is required to make definitive quantitative statements.

4.2.3.2 Electron Emission Spectra

It has been shown that secondary electron emission spectra are an effective method of determining negative surface potential. In an effort to prove that deep charging is responsible for the differences seen in the yields of irradiated and unirradiated Kapton HN a series of emission spectra were taken to see if any shift could be seen in the SE emission peak.

The data shown in FIG. 4.26a are a series of emission spectra taken at 200 eV and plotted in chronological order from top to bottom. A spectrum uses a DC ~1 nA beam and takes roughly 10 minutes to complete, this is ~10^5 and 0.6 μC. When the first measurements finished, the next spectral measurement was started immediately. In this fashion, all seven spectra shown in FIG.

4.26a, were taken, and show the typical peak from the inner grid centered at 2 eV. The top curve

in FIG. 4.26a also shows a SE emission peak centered at 13 eV that is presumed to originate from

the sample. This would indicate a negative sample potential of roughly -11 V using the arguments

for surface potential detailed in Section 4.1.3. This is not expected, as the incident electron energy

should have a total yield of ~2 giving it a positive surface potential. If there is a deep negative

charge in the material from previous measurements, one would expect that potential to quickly

become positive when bombarded with primary electrons of energy $E_1 < E_b < E_2$. This idea is based

on internal charge recombination and the liberation of excess electrons as SE's. In reality, the

opposite seemed to occur. Not only did the SE peak remain after several minutes, but it becomes

more negative in subsequent spectra. In the third plot, after approximately 20 minutes of

continues exposure, the sample seems to stabilize at a constant surface potential of -28 V.

This phenomenon may be explained by the idea that it is not the surface potential that

defines the spectral shift in the SE emission curve. One needs to remember that when an insulator

builds up a potential, it is not a simple slab-like internal charge distribution. It is, in fact a

complex layering of charges defined by the DDLM. The net effect of these layers defines the

magnitude of surface potential, but it is important not to forget that the internal distribution is not

so simple.

With this in mind, the problem of the unexpected shifts in the spectrum for irradiated

Kapton HN may be due to the origin of the SE rather than the surface potential. That is to say,

that the local potential in the layer where the SE was produced is the potential barrier it must

overcome to escape the material. The net electric field is not the relevant parameter, but rather the

field at the SE origin that will define its emission energy spectrum. One possible explanation for

the negative shifting SE emission peak at an energy that would normally produce a positive

potential, is that the DC beam used for emission spectra is exciting SE's from a negatively
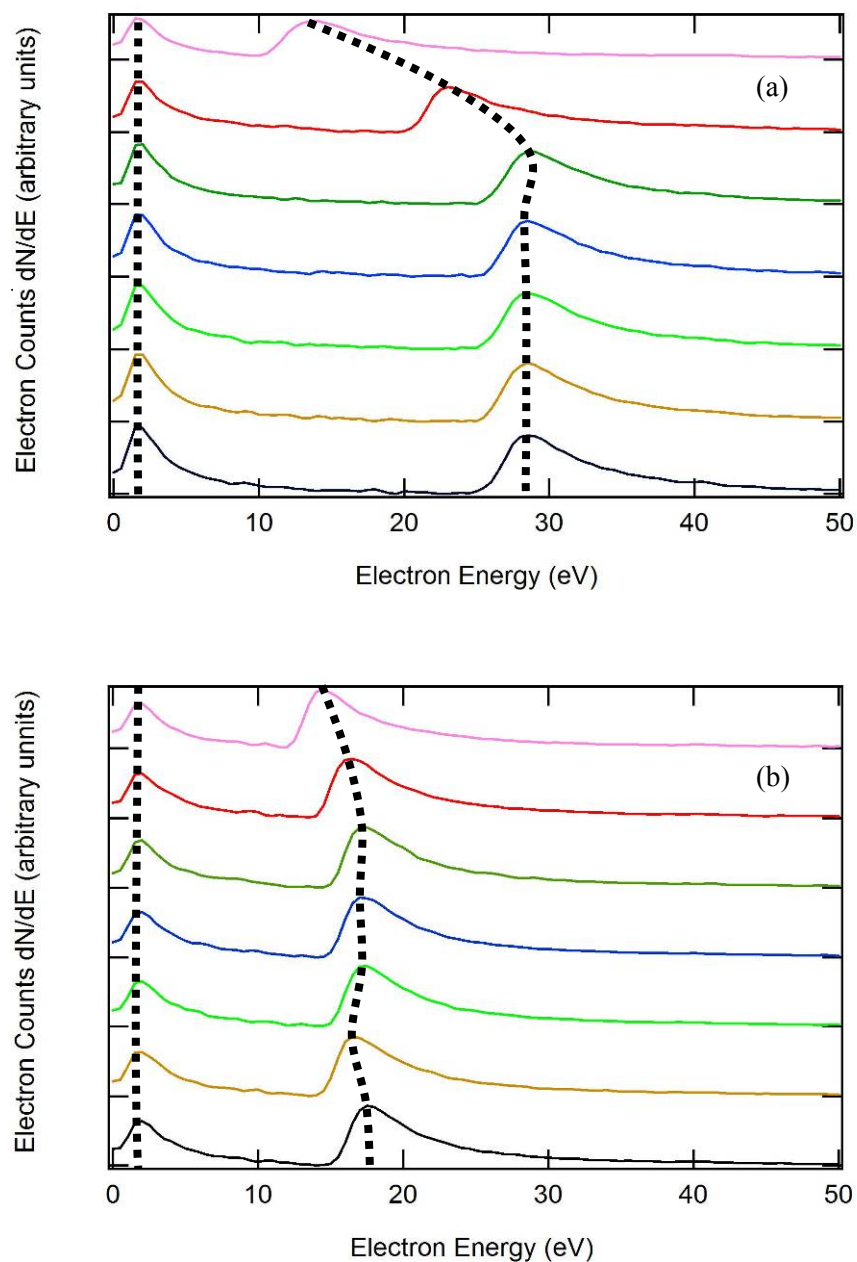
FIG. 4.26. Electron emission spectra from irradiated Kapton HN
(a) Seven consecutive 200 eV SE emission spectra taken with a DC beam on Kapton HN. Note that there should be no evidence of negative charging like the second peak seen here as $E_1<E_b<E_2$. Also, the DC beam used should cause the material to come to an equilibrium state in a few seconds, not the tens of minutes required to measure the spectrum. (b) Seven consecutive 350 eV SE emission spectra taken with a DC beam.

charged region left over from previous measurements. Over time, the beam would deposit electrons at the penetration depth R and possibly enhance the effect.

After the plots shown in FIG. 4.26a were taken at 200 eV, the gun was retuned for 350 eV incident energy and a similar set of spectra were taken. A similar, but less pronounced, trend in the data taken at 200 eV can be seen in the SE emission peak evolution in FIG. 4.26b. The first plot shows a sample peak at 15 eV and an inferred surface potential of -13 V, then over time settling at an energy of 18 eV and potential of -16 V. In this case, the shifting of the SE peak is not as dramatic as 200 eV incident energy. This may be because 200 eV is closer to δ_{max} and therefore quicker to charge. It may also be that the space charge has approached a saturation limit. Saturation might result from filling most available defects.

One more set of spectra (shown in FIG. 4.27b) was taken at 950 eV, an energy greater than E_2 and in the negative charging regime. These data do not show a sample peak that is distinct from the inner grid peak. This is due to the fact that the sample has been charged to a value greater than the 50 V discriminating voltage used in this test. No SE's from the sample would be discriminated as they all have a kinetic energy greater than the discriminating E-field. This conclusion has been reached by careful examination of the total electron yield seen in FIG. 4.16b. It can be seen that the sample reaches approximately -50 V with incident electron energies of $\geq$ 800 eV as seen by the SE$\rightarrow$BSE jump. Thus, at an incident energy of 950 eV, as used in these spectra, one would expect a surface voltage accumulation of >50 eV and a concurrent shift in the Kapton SE peak to an off-scale value.

There is a small anomalous peak seen at 41 eV. This has been seen in several spectra including Au, and is assumed to be an artifact of the detector system (see Section 3.1.2). If this is true, it will be possible to determine its origin by systematically applying a bias to each element in the detector and watch for this peak to shift. This has not been done, but should be included in future work on detector characterization.
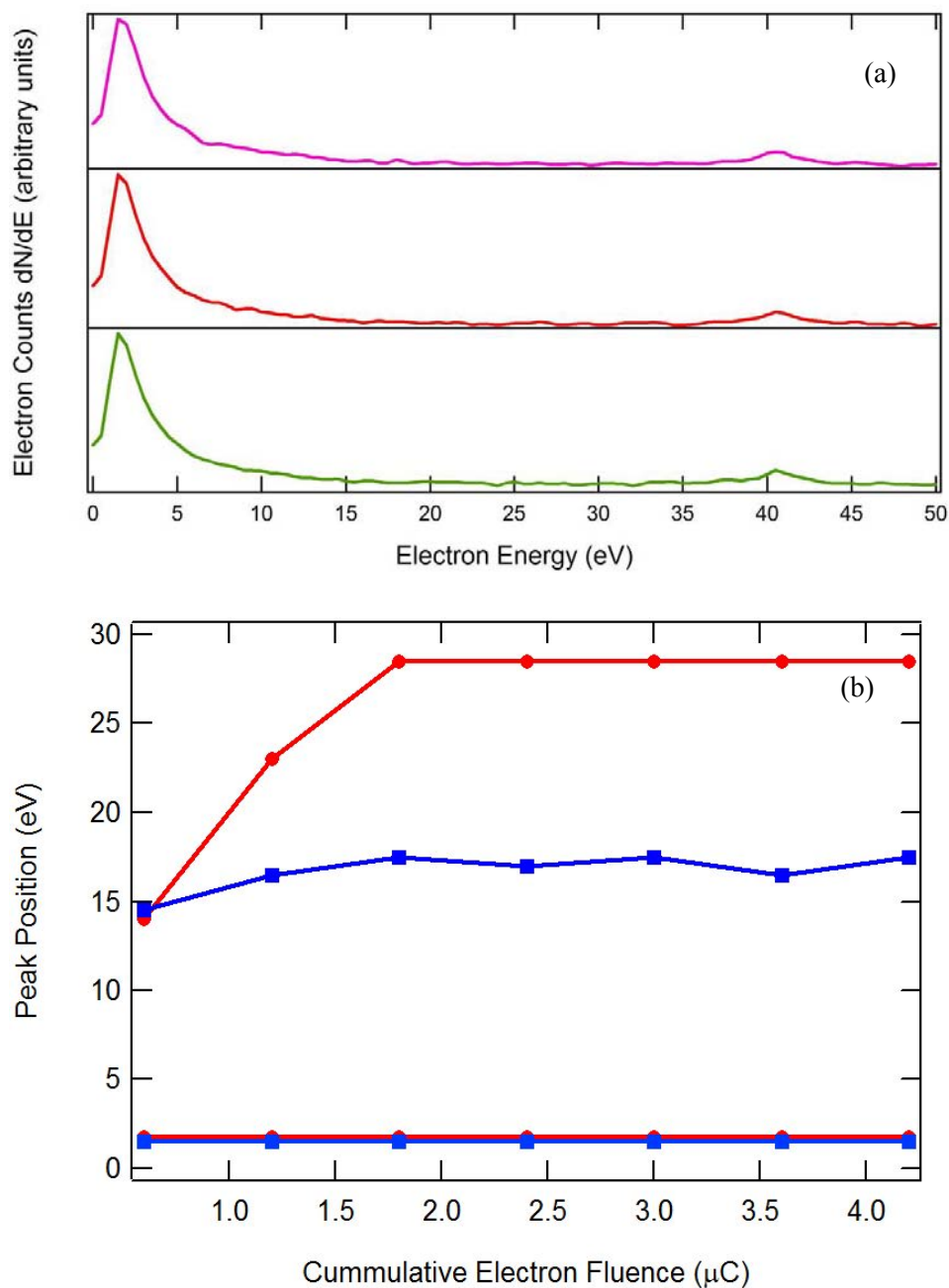
FIG. 4.27. Emission peak position and emission spectrum from Kapton HN.
(a) Three consecutive measurements of the secondary electron emission spectrum taken at an incident energy of 950 eV. Note the absence of a sample peak that would indicate the development of a negative surface potential. (b) Plots of the sample and inner grid peak position for each consecutive spectra. The red data is the sample peak position at 200 eV incident beam. The blue data shows the sample and inner grid peak position of the spectra taken at 350 eV incident beam.

Many questions have been raised by these data of irradiated Kapton HN that are not easily explained in the framework of this thesis. These data have been presented to bring to light its existence and to underscore the dynamic nature of these types of measurements. The weak link in the efforts to model and predict spacecraft charging is the material properties. But it has been shown here that these properties can change after relatively little damage. The work discussed in this section is not a completed treatment of the topic of material aging and the effect it might have on charging, but there are several important ideas that have been brought to light. First is that the relevant potential to consider when determining SE peak positions in electron emission spectra is not the net surface potential, but the local potential at the SE origin. The field traversed by an SE between its origin and the surface determine its exit energy seen in emission spectra. Second is that as defect trap states are created in the material by radiation damage, the ability of the material to trap and store charge is affected. As more traps are created, the ability of the material to accumulate negative charge is enhanced while, at the same time, its ability to leak charge away is also modified.

4.3 Low-Conductivity High-Yield (Polycrystalline Aluminum Oxide)

Polycrystalline aluminum oxide is a ceramic and is widely used in spacecraft design. It is durable, light, and very hard. It can be used for electrical isolation, as well as coatings for large areas, to increase durability and thermal control. The material studied here is a bulk polycrystalline aluminum oxide ceramic coating that is a candidate to be used as thermal control in a wide range of environments (Donegan *et al.*, 2010). This study may have implications for a broader class of materials as very thin layers of aluminum oxide coat many spacecraft superstructure as anodized aluminum. It can also be found in optical elements, such as sapphire lenses.

For the purposes of this study polycrystalline aluminum oxide provides, from the charging perspective, the most challenging material. This material has an extremely low

conductivity, and can store charge for several days, and has an extremely high total yield. The combination of these two material properties make polycrystalline aluminum oxide exceptionally good at gathering and storing charge, and provides conditions that will test the capabilities of the instrumentation and methods developed herein.

4.3.1 Material Characterization

The sample tested was a 1.07±0.02 mm thick bulk polycrystalline aluminum oxide material, attached to a Cu slug using double sided Cu tape. No specific details of the material properties, source, or preparation are available. We expect that the sample is a mixture of α-alumina and γ-alumina made by heating aluminum hydroxide and oxyhydroxide. The alumina is believed to be Type II material. The materials were deposited either by plasma spray deposition or chemical vapor deposition to the desired thickness. Information about this process and the resulting ceramic microstructure can be found elsewhere (Donegan, Sample *et al.*, 2010). This material is known to have high electrical conductivity at room temperature ($3 \cdot 10^{-16}$ (Ω-cm)$^{-1}$) and density of $3.83 \pm 0.03 \cdot 10^3$ kg/m^3 (Shugg, 1970; Morrell, 1987; Hayward, 2009). This material is known to have an electrostatic breakdown strength at room temperature of 27.4 ± 0.9 MV/m (Shugg, 1970; Morrell, 1987; Yoshimura and Bowen, 2006).

We do not know many of the properties of this specific material because information regarding the crystalline structure is scarce due to the proprietary nature of manufacturing. This material was developed as a thermal spacecraft coating. There are a few forms of aluminum oxide (Al_2O_3), with corundum, α-alumina or α-Al_2O_3 being the most common. The structure of corundum can be viewed as a hexagonal, close-packed array of oxygen atoms with $^2/_3$ of the octahedral sites occupied by Al^{3+} ions. Thus, the Al^{3+} ions are bonded to six oxygen atoms in a distorted octahedron. Each such octahedron shares a face with one on the upper and one on the lower layers. The distortion is caused by repulsion between Al^{3+} ions in octahedral sharing the

faces. Other compounds with this structure include Cr_2O_3, α-Fe_2O_3, Ti_2O_3 and V_2O_3. The crystal structure of aluminum oxide is shown in FIG. 4.28.

Corundum is dense (density of $3.97g/cm^3$), hard (9 out of 10 on the Mohs' scale, next only to diamond), high melting (melting point 2288 K), and insoluble in water. Crystals of corundum are usually prismatic or barrel shaped bounded by steep pyramids. γ-alumina is formed when aluminum hydroxide [$Al(OH)_3$] or oxy-hydroxide [$AlO(OH)$] is heated. The structure is very similar to α-Al_2O_3, differing largely in the position of the unfilled Al sites. Under close scrutiny, γ-alumina is found to have a rhombohedra structure. A rhombohedra or trigonal lattice has all sides equal, with all angles equal but not a right angle. Further details of the crystal structure, and particularly the structure of the Al vacancies is found in Bartnikas (1987).

Aluminum oxide is responsible for metallic aluminum's resistance to weathering. Metallic aluminum is very reactive with atmospheric oxygen, and a thin layer of aluminum oxide quickly forms on any exposed aluminum surface. This layer protects the metal from further oxidation. The thickness and properties of this oxide layer can be enhanced using a process called anodizing. Anodizing is a process used to protect aluminum from abrasion and corrosion and to allow it to be dyed in a wide range of colors. The process derives its name from the fact that the part to be treated forms the anode portion of an electrical circuit in this electrolytic process. A layer of aluminum oxide is created on the surface of the aluminum from the action of the current being passed through the part, which is bathed in an acid solution. This aids in the formation of the oxide layer. This oxide layer increases both the hardness and the corrosion resistance of the aluminum. The aluminum oxide coating is grown from and into the surface of the aluminum. Because of this (unlike coatings), it is not prone to peeling or cracking. It also possesses excellent thermal and electrical insulation qualities. The oxide forms as microscopic hexagonal pipe crystals of corundum, with each having a central hexagonal pore (which is also the reason that an anodized part can take on color in the dying process). The primary source of contamination in the
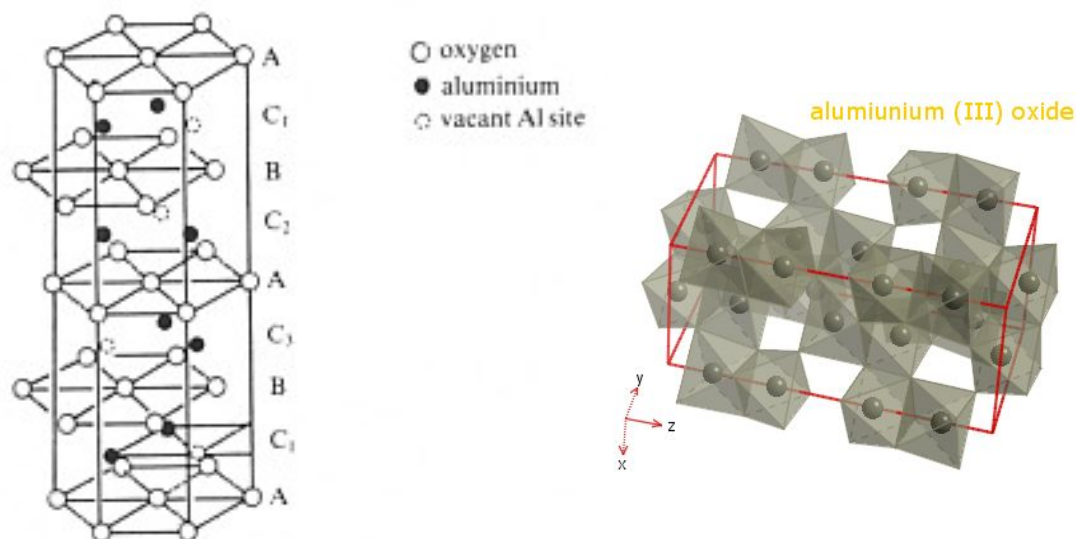
FIG. 4.28. Crystal structure of alumina.
(α-Al2O3) is a hexagonal closed packed structure. The aluminum sites (layers C1, C2, C3) which are only two-thirds full, are sited between the hexagonal layers of oxygen atoms (A,B).

various types of alumina is the presence of silicate compounds. These can occur either as substitutions of Si for Al in the Al_2O_3 lattice or as inclusions of SiO_x material. Further details of the crystal structure, and particularly the structure of the Al vacancies is found in Bartnikas (1987).

Radiation-induced conductivity in polycrystalline aluminum oxide can be expressed as temperature-dependent functions of k_{ric} and $\varDelta$ over a range of ~290 K to ~1200 K can be derived from four curves of Al_2O_3 presented in Klaffky et $al.$ (1980). $\varDelta$ is ~1 below ~600 K, decreases to ~0.74 at 810 K, and asymptotically approaches 0.5 at higher temperatures. K_{ric} has a minimum value of $1.1 \cdot 10^{-16}$ $(\Omega\text{-cm-Rad/s})^{-1}$ at ~630 K, increases roughly exponential lead to $1.2 \cdot 10^{-14}$ $(\Omega\text{-cm-Rad/s})^{-1}$ at 1220 K, and increases roughly exponentially to $4.8 \cdot 10^{-16}$ $(\Omega\text{-cm-Rad/s})^{-1}$ at 290 K with decreasing temperature. The observed temperature dependence of k_{ric} and $\varDelta$ is consistent with predictions (Corbridge et $al.$, 2008; Donegan et $al.$, 2010) based on the Rose-Fowler multiple trapping model (Rose, 1951; Fowler, 1956).

An attempt was made to image this material under the microscope, but no useable images were obtained. The material is pure white and is very diffusive, so any images had no discernable features.

By using the same method described in Section 4.1.1, the penetration depth or range R was determined for this material and can be seen in FIG. 4.29.

4.3.2 Electron Emission

Since Al_2O_3 has a combination of low conductivity ($\sim 10^{-16}$ $(\Omega\text{-cm})^{-1}$) and high total yield (~ 7) it is very prone to charging (Donegan, Sample *et al.*, 2010). As a result, several different methods were attempted to measure the uncharged yield. These methods include low fluence pulsed yields at room temperature and again at an elevated temperature in an attempt to increase the DC conductivity and dissipate the charge (Ashcroft and Mermin, 1976; Wintle, 1983). Finally the composite electron yield method was employed using multiple electron yield decay curves and the model described in Section 3 (Hoffmann *et al.*, 2008).

4.3.2.1 Traditional Pulsed Electron Yield

The effects of charging on the yield curves of Al_2O_3 evident in FIG. 4.30 largely follow the scenarios for zones 1 thru 4 described in Section 4.1.2 and 4.2.2. In zone 1 the yield is elevated to near unity due to negative charging, though the effect is not large. Pronounced effects of charging of Al_2O_3 in the pulsed yield are evident by the depressed yield observed between incident energies of ~ 200 eV to ~ 1100 eV, in the central part of zone 2. As the total yield increases, so does the number of SE's produced, thus charging the material more rapidly. Each incident pulse used to measure the yield curve in FIG. 4.30 contained roughly $4 \cdot 10^{-13}$ C and is near the minimum pulse flux the system can measure. This pulse does not appear to induce significant charging until a yield of 4.6 is reached. At this point, the pulse begins to induce a few volts positive surface potential and a significant number of secondary electrons begin to be
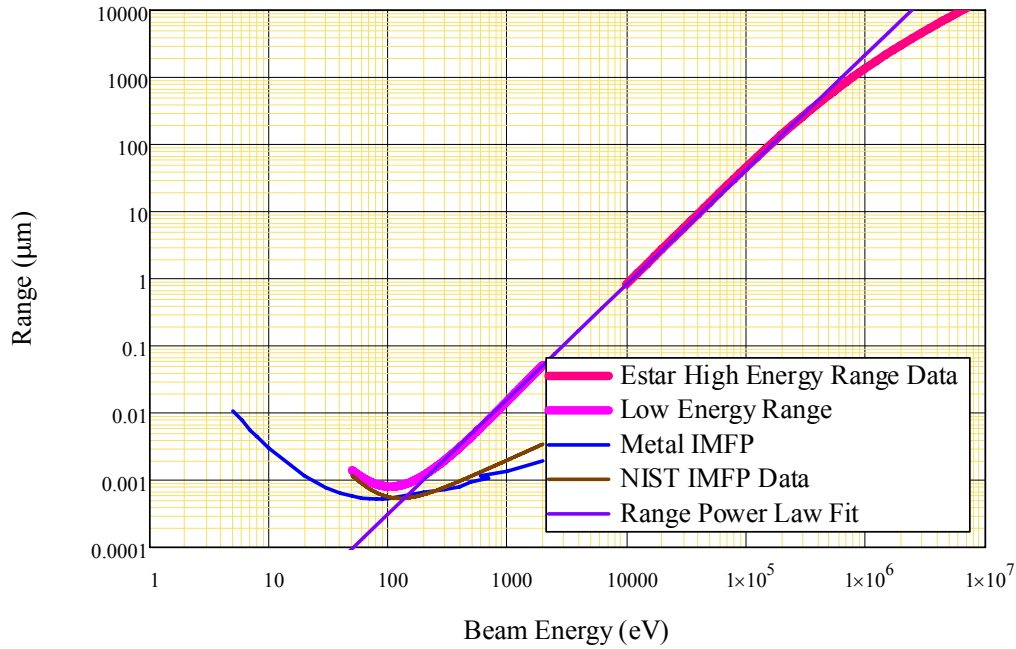
FIG. 4.29. Electron penetration depth of polycrystalline Al_2O_3.

reattracted to the surface and the yield is pushed to unity. This continues as the incident electrons increase in energy until they approach the second crossover energy E_2=3290±50 eV. As the total yield drops below 4.6 the measured yield comes back to our idealized uncharged green curve in FIG. 4.30. But on closer inspection at ~1100 eV, the effects of charging might be evident at much lower incident energies and, consequently, a much lower total yield. There is a slight irregularity in the total yield at an incident energy of ~90 eV and a total yield of ~1.9. This might be an indication of the onset of significant charging at incident energies only slightly greater than E_1=74±8 eV. This is all speculative, but it can be said that at total yield σ<4.6, the effects of charging are, at worst, less pronounced, and at best, insignificant.

The yield in zone 3 at energies E_2<E_o<$5E_2$ (up to ~15 keV) are seen to be above the idealized green curve, which may be indicative of additional SE being accelerated out of the electron depletion region (as was observed for CP1 but not for Kapton HN) showed no unusual behavior. In fact, it should be noted that the no jump in the BSE was seen, indicating that the sample surface voltage never exceeded -50 V. But upon inspection of the last point in the FIG.
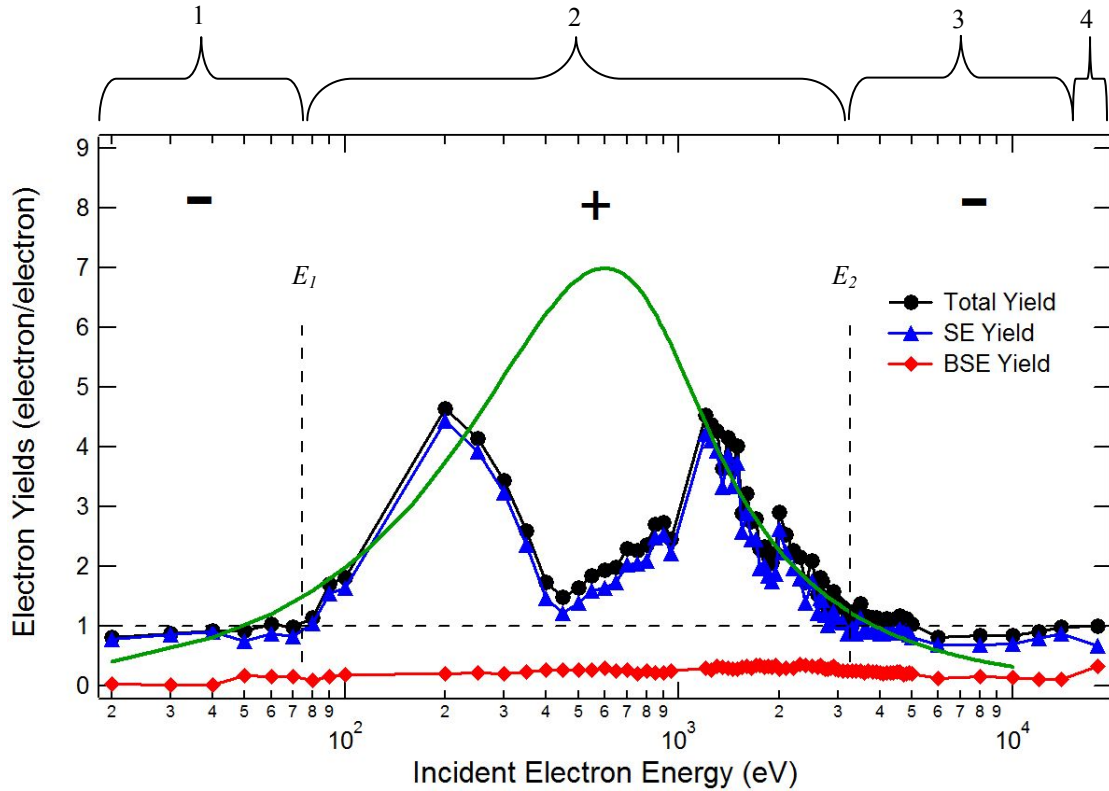
FIG. 4.30. Complete room temperature (296 K) yield curve taken on polycrystalline Al_2O_3.

4.30, there is some indication that the incident energy of 18 keV is close to the boundary of zones 3 and 4 where the potential necessary to cause the SE→BSE shift has almost been reached, as discussed in Section 4.1.2.3. To confirm this it would be necessary to use a probe pulse of greater energy than is currently possible in the analysis chamber.

In short, this traditional yield measurement has shown that this material exhibits extreme charging in the positive charging area between the crossover energies, but more manageable charging signatures in the negative charging areas. These data indicate that this material might make a good candidate composite yield method described in Section 2, but as this method is very time intensive, an effort was first made to overcome these charging problems by modifying the conductivity of the material so that it might dissipate the charge faster. These efforts are described in the next section.

4.3.2.2 Heated Electron Yield

It is clear that the traditional pulsed methods are incapable of accurately measuring the yield of a material with a yield as high as polycrystalline aluminum oxide. Since the extent of charging is dictated by both the yield and the conductivity, heating the sample should reduce charging by thermally enhancing the conductivity. Several available data sets of the dark current conductivity $\sigma_{DC}(T)$ of Al_2O_3 as a function of temperature (Shugg, 1970; Morrell, 1987) showed a roughly exponential increase in conductivity with increasing T. These combined data sets were fit with an Arrhenius function (Donegan, Sample $et~al.$, 2010) of the form

$$\sigma_{DC}(T) = \sigma_o^{DC} e^{-E_a/k_B T}$$

(4.1)

as predicted by standard theories of thermally assisted conductivity of semiconductors and insulators at higher temperatures (Ashcroft and Mermin, 1976; Wintle, 1983). In such models, $\sigma_{dc}=3 \cdot 10^{-16}$ (Ω-cm)$^{-1}$ at 296 K sets the magnitude of the conductivity and E_o=0.75 eV is an activation energy for electrons excited from localized trap states into the conduction band. The fit was scaled so that it has the manufacturer's conductivity value at room temperature T for the specified type of Al_2O_3 studies here (Hayward, 2009). This conductivity versus temperature fit can be seen in FIG. 4.31. There are two relevant time scales that need to be considered in the understanding of these data. The first is the time scale between each sequential incident pulse of the probe beam (typically 5 s). If no discharge methods were employed, then the voltage induced from each pulse would need to dissipate to ground through intrinsic conduction mechanisms (DC and RIC). The required conductivity for this to occur is $\sim 10^{14}$ (Ω-cm)$^{-1}$, which would be achieved with a material temperature of 314 K. With conductivity in this range, we can be assured that all the charge build up from the probe pulse will not affect the yield from subsequent pulses. In the case of polycrystalline aluminum oxide, we see considerable charging in the positive charging
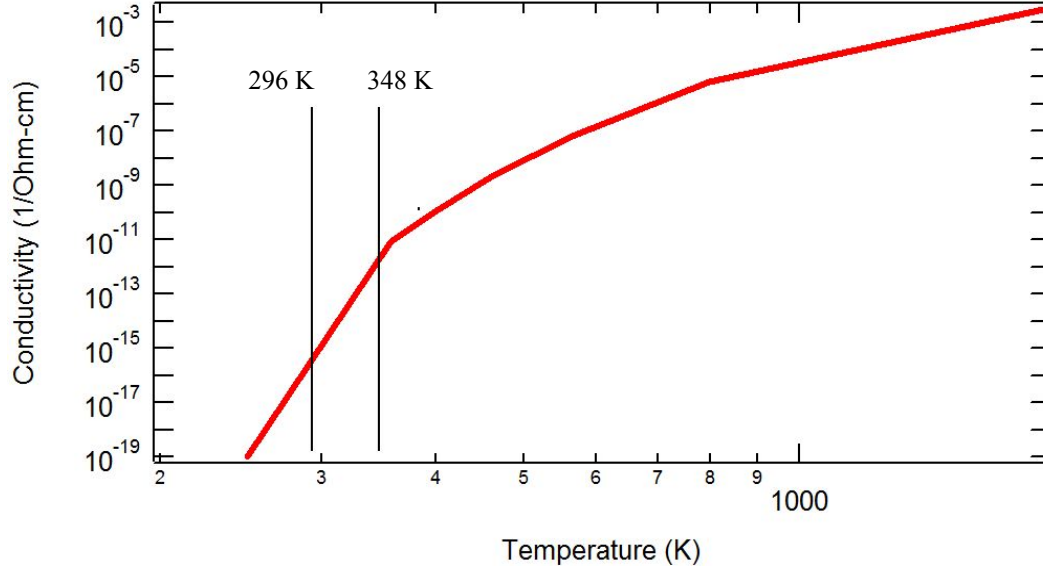
FIG. 4.31. Conductivity of aluminum oxide as a function temperature.
The vertical lines indicate the two temperatures relevant to this study.

regime between the crossover energies in both the heated and room temperature yield measurements, suggesting a lower conductivity.

We have shown in Section 3.2.1 that in this regime, low-energy electron flooding is effective at dissipating the residual charge after the pulse so that charge does not accumulate from pulse to pulse. From this we can now surmise that the incident pulse is inducing significant charging as seen in Section 4.2.2.6. That is to say that the first part of the pulse is charging the material to a voltage significant enough to reattract the electrons generated by the latter part of the pulse. Because of this, the other relevant time scale to consider is that of the incident pulse itself of 5 μs. For this, a conductivity of $\sim 10^{-11}$ $(\Omega\text{-cm})^{-1}$ would be required. In polycrystalline aluminum oxide we can expect the DC conductivity to reach this value at a temperature of ~361 K. At present, the analysis chamber is not capable of attaining this high of a temperature. The data shown in FIG. 4.32a show the yield taken at 296 K, $3 \cdot 10^{-16}$ $(\Omega\text{-cm})^{-1}$ and a corresponding decay time of ~10 min. This is longer than both relevant time scales but due to our discharge techniques only the charge induced by the pulse is changing the yield. FIG. 4.32a shows the yield measured

at 348 K and a conductivity of $9 \cdot 10^{-12}(\Omega\text{-cm})^{-1}$ and a corresponding decay time in the tenth of a second time scale.

The total yields from both the room temperature and that of the elevated sample are plotted together in FIG. 4.32b to show any differences. Elevating material temperature to alleviate charging problems assumes that the only way sample heating will affect the yield is through modification of the DC resistivity and subsequently the acquired surface potential. However, we know this not to be true. It is not well understood how temperature will affect the generation of SE's in the bulk of the material or how increased thermal energy might change the probability that SE's will escape the surface and contribute to the yield. We can guess that there is an effect and that it could be significant as it is in the temperature dependence of DC conductivity. We also know that RIC is temperature dependant (Rose, 1951; Fowler, 1956; Dennison *et al.*, 2008), so it is not unreasonable to assume that temperature will change charging by directly affecting SE production and escape, or that it will change it indirectly through conduction mechanisms.

The heated yield curve does reflect some relief from charging as seen in FIG. 4.32b. There has been a shift in the crossover energies from $E_1=74\pm8$ eV and $E_2=3290\pm50$ eV at 296 K to $E_1=30\pm10$ eV and $E_2=4000\pm100$ eV at 348 K. This is consistent with the idea that the entire curve is being pulled toward unity as the potential increases. We also note that the heated curve displays an increased yield at ~200 eV from a total yield of 4.6 for low temperature, to 5.5 for elevated temperature. Also, the dip between the total yield peaks at ~400 is not as close to unity as in the cooler curve. This is an indication that the potential has lessened to some extent, or that the high temperature yield has increased in magnitude.

Lastly, zone three yields remain near unity for both temperatures. However. With the increase in E_2 at elevated temperature, zone three shifts to higher energies. In the curve taken at 296 K the last point in the plot at 18 keV indicated that the material may be close to the zone
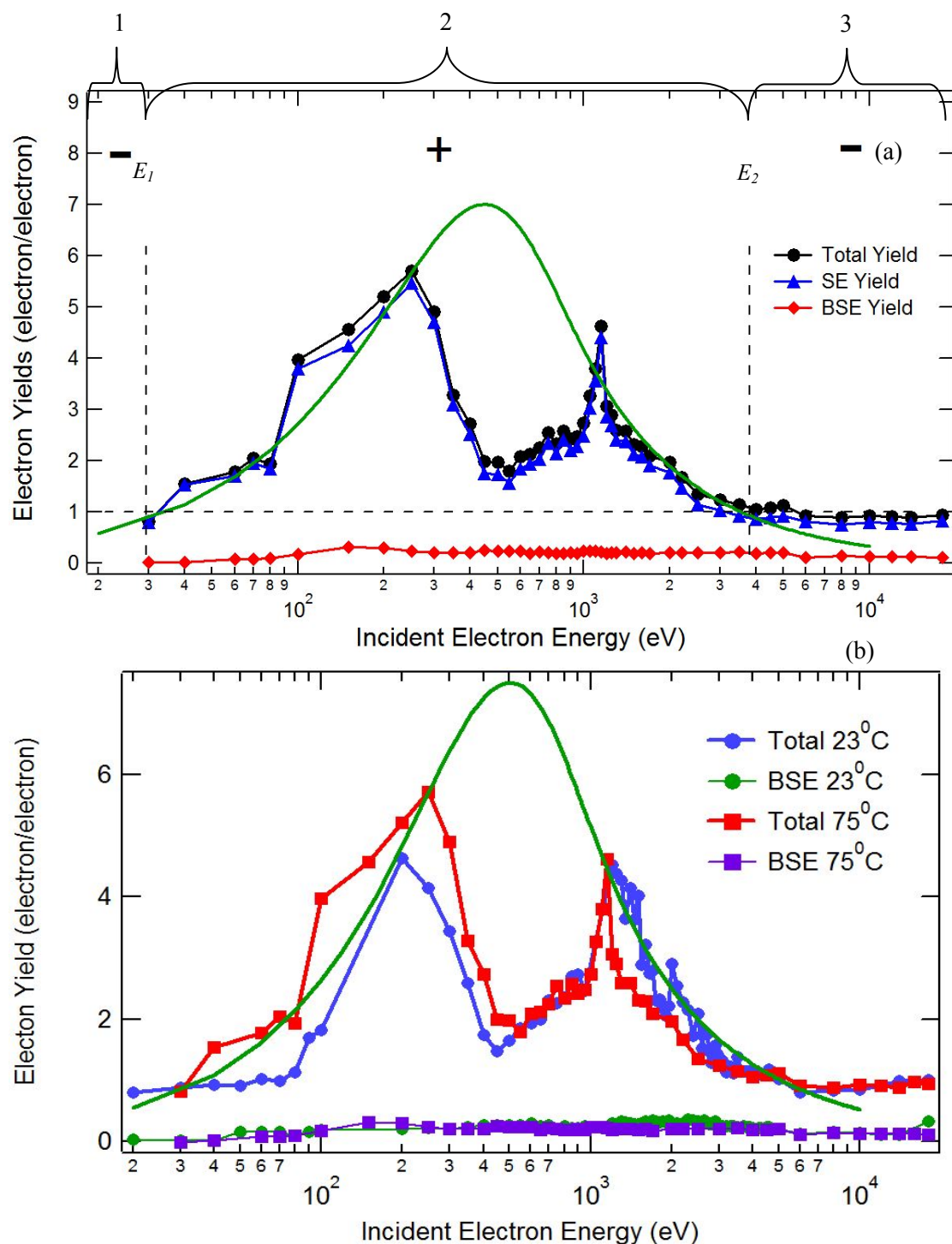
FIG. 4.32. High temperature yields of alumina.
(a) Complete yield curve taken on polycrystalline aluminum oxide while sample was maintained at an elevated temperature 348 K. (b) Comparison of the yields from polycrystalline aluminum oxide at 348 K (total yield red; BSE yield purple) and at 296 K (total yield blue; BSE yield green).

three to zone four transition and the critical -50 V required for the SE→BSE shift discussed in

Section 4.1.2 and 4.2.2. The curve taken at 348 K shows no such indication suggesting the

SE→BSE shift has moved energies above the measured energy range.

Despite the encouraging results heating has had on mitigating charging effects to the

total, SE, and BSE yield for polycrystalline aluminum oxide it has not eliminated the problem

fully. A material with a lower intrinsic total yield may be able to benefit fully from heating, but

for this material other techniques must be employed.

4.3.2.3 Composite Electron Yield

Measuring the yield for a minimally charged insulator may be possible if the noise in the

system can be sufficiently reduced to allow lower flux probe pulses, or if the material was heated

to a sufficient temperature to increase conductivity to $\sim 10^{-12} \, (\Omega\text{-cm})^{-1}$ so imbedded charge would

easily dissipate to ground. As an alternative we have employed a method for turning charging to

our advantage. In Chapter 2, a method was developed to determine the dependence of the yield on

surface potential (Hoffmann *et al.*, 2008). Equation (2.17) provides a model to calculate surface

potential from the accumulated incident charge density. Equations (2.17) and (2.19), with V_s as an

implicit variable, allow calculation of yield as a function of cumulative charge, that is, the yield

decay curves. In practice, the lower integration limit in Eq. (2.13) needs to reflect the average

residual charge accumulated on the surface during the first pulse. This now provides an

expression for the yield as a function of surface potential.

Decay curves were measured over a spectrum of 21 incident energies ranging from 200

eV to 5000 eV and fit with Eq. (2.17). This method of yield measurement is invalid at energies

below 200 eV because we can no longer make the assumption that the BSE are not affected by

surface potential. All assumptions made for this model are outlined in Section 2.4. We can then

predict yield curves as a function of incident flux (or equivalently surface voltage by use of the

DDLM) by determining the yield at a specific cumulative incident charge resulting from the fits

to the measured decay curves. One of these decay curves taken at 200 eV and its fit is shown in FIG. 4.33a; it is representative of all 21 energies for which data exists. In order to fit the decay curve data we must use the parameters obtained from fitting the Chung and Everheart model to a measured SE emission spectra. To provide a thorough treatment of this method, one would measure the SE emission spectrum at the same energies as each decay curve. This would provide a measured data for each decay fit. In the interest of time, we have relied on the measurements taken in Section 3.1.3 that show that surface potential does not affect the shape of the emission peak, but only shifts it. Since the shape of the emission spectrum is what is relevant to this method, we can use only one representative spectrum and use it for all decay curves. In our case, we used the data from FIG. 4.36g taken with an incident beam E_o=98±1 eV. This was chosen because it was a clean measurement and near the first crossover energy so any unforeseen charging effects would be minimized.

It may be possible to further simplify the process by not only assuming that the SE emission curve is unaffected by charging but that the yield decay curve is modified in a predictable way. This is equivalent to assuming that each material has a universal yield decay curve. This would be accomplished by measuring the yield and the surface voltage around E_1 and E_2 to create a universal yield decay curve that can be scaled to the measured surface voltage. This would need to be augmented by spot checking the yield decay curve, but would ultimately make it unnecessary to take yield decay curves over the full yield curve.

Doing this allows the extrapolation of the yield to an incident flux approaching zero. This extrapolation is shown in the green data in FIG. 4.33b plotted with the blue data taken with the pulse system at room temperature. This method alleviates the charging problems encountered between the crossover energies in the positive charging regime as is shown FIG. 4.33b. This extrapolation predicts the maximum total yield σ_{max} of 6.4 at an incident energy of E_{max}=500±50 eV. It should also be noted that this method is in good agreement with pulse yield method at
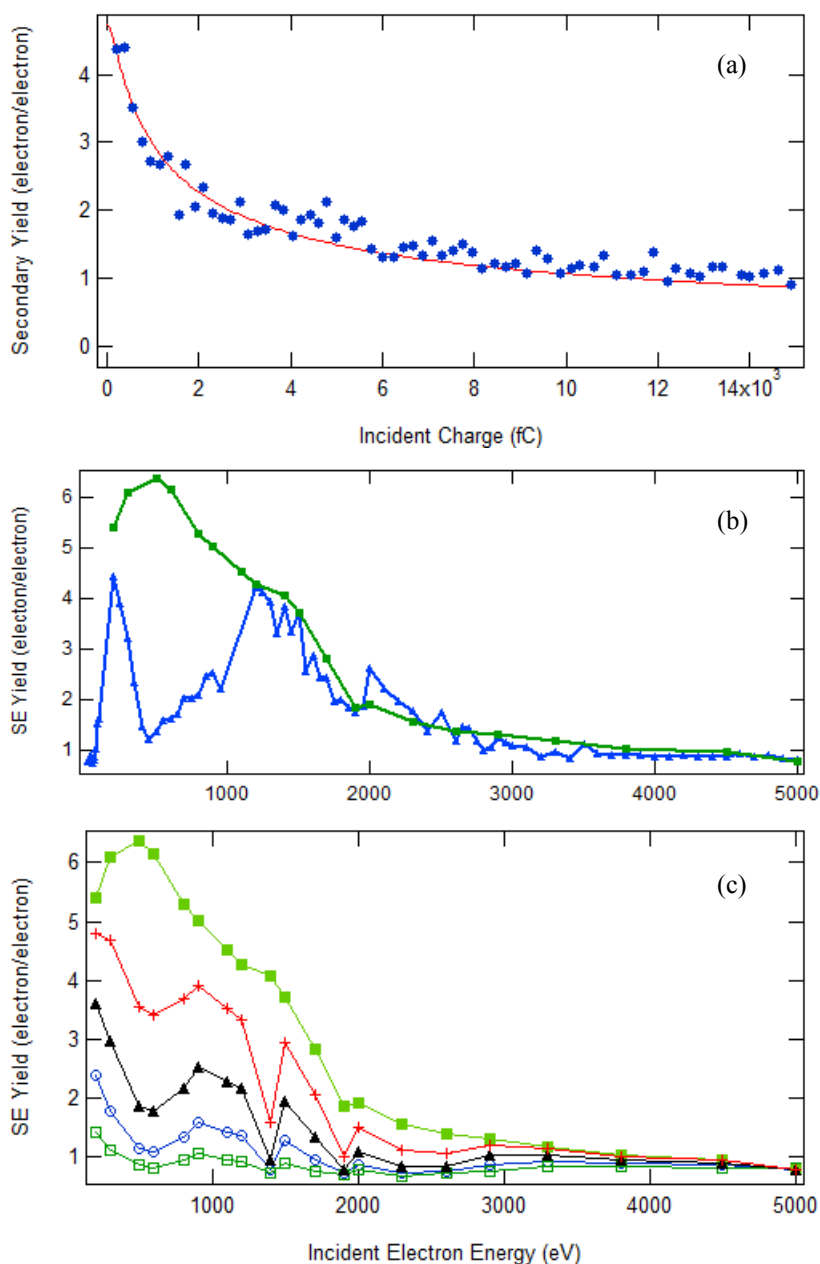
FIG. 4.33. Yield decay curve and composite electron yield for polycrystalline Al$_2$O$_3$.
(a) Yield decay curve taken on alumina at 200 eV. The red line is the fit developed in Section 3 based on Eq. 2.17 and Eq. 2.19. (b) Blue data are total yield from the pulse system discussed in Section 4.3.2.1. Green data are the results of many decay curves fit with the results of Section 3 and extrapolated to 0 C incident flux(c) These data show the calculated curves for several surface potentials. The green (solid square) curve shows the yield curve at 0 V surface potential. Red (plus) curve shows a 2 V potential, black (triangle) curve is 5 V, blue (circle) curve is 10 V and green (square) curve is 20 V. Note the emergence of the dual-peak behavior as the surface potential increases, and the approach to a yield curve of unity at higher potentials.

energies that show little charging E_o>1200 eV. This is a good indication that the composite yield curve method described here and in Section 2 is correctly predicting the total yield.

While this method is very time intensive, it can provide a great wealth of information. We can extrapolate these decay curve fits back to a zero surface potential to generate the intrinsic yield curve shown in green on FIG. 4.33b. When compared to the traditional yield curve measurements (blue data in FIG. 4.33b) described in Section 4.3.2.1, this seems to have resolved the charging difficulties, predict a much higher σ_{max}, and eliminates the double peak behavior.

In addition, FIG. 4.33c shows the yield curves predicted at several representative surface potentials. We see that, as the potential increases, we start to see the emergence of the dual-peak behavior observed in the traditional low-fluence pulsed method of yield measurement. From this we can determine that the surface voltage induced during the traditional pulse yield method was ~5 V. We also note that at higher surface potentials the yield curve approaches unity at all incident energies (see FIG. 4.33c). This is consistent with total SE recapture due to accumulated positive surface potential, and supports the model in this limiting case.

It is shown in FIG. 4.34a the difference between the yield that has been predicted for a 0 V surface potential and the predictions for 2 V, 5 V, 10 V and 20 V. The greatest difference is seen in the prediction for 20 V and has a maximum of 5.5±0.2 at an energy of 500±50 eV. The fractional difference of the 0 V yield and the other predictions is shown in FIG. 4.34b. It too shows that the greatest difference is in the prediction of a 20 V surface potential and is 86% at 500±50 eV. Both of the plots in FIG. 4.34b show a convergence of results after the second crossover energy E_2=3290±50 eV. This supports the position of the crossover energy by showing that the yield stops responding to the surface potential. This is because there is no charging at E_2 and at higher energies the negative potential of the material does not significantly modify the yield.
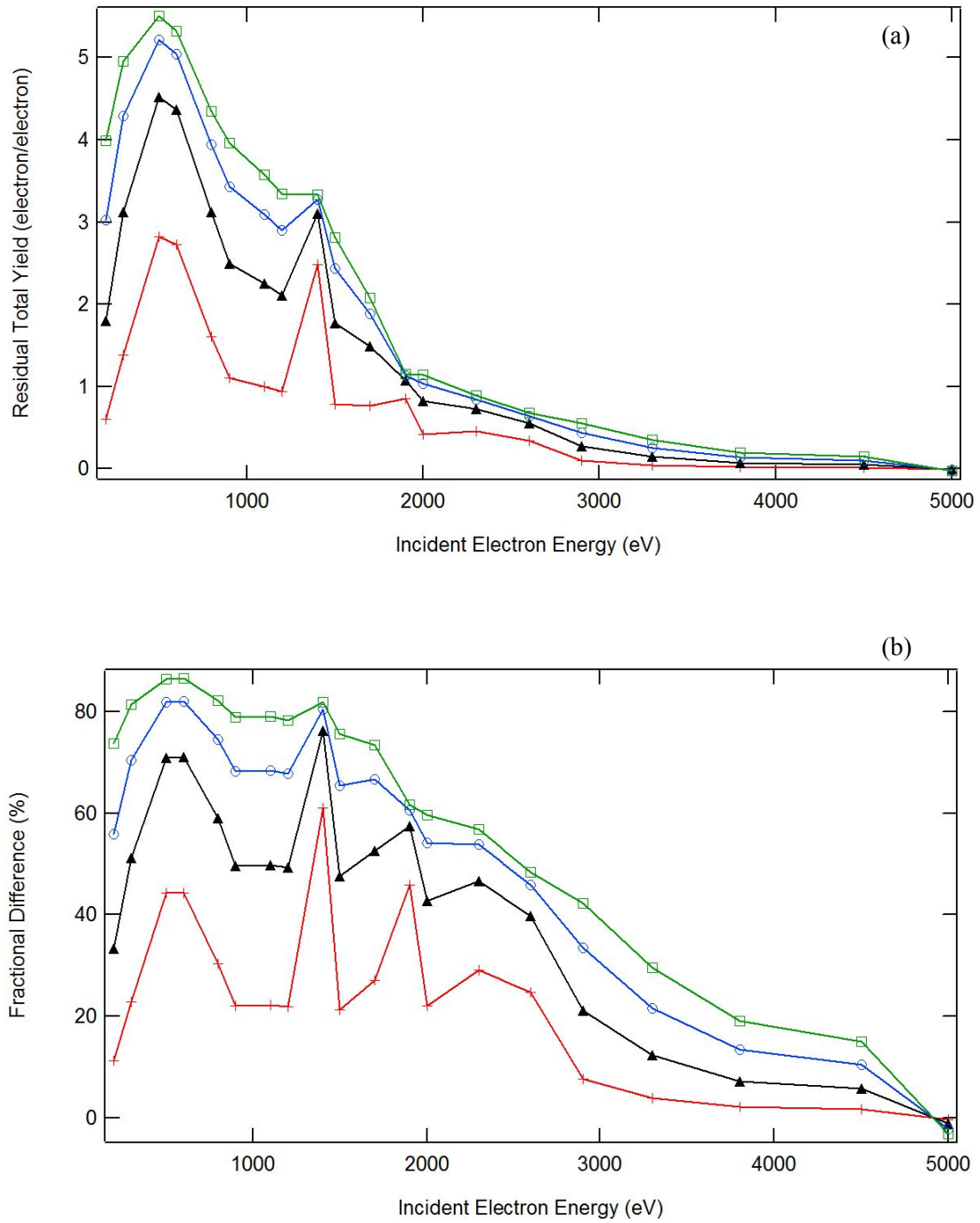
FIG. 4.34. Residual plots of uncharged composite SE yield and voltage modified yield.
(a) Difference between SE yield extrapolated to V_s =0 V and the extrapolation to 2 V (red) 5 V
(black), 10 V (blue) and 20 V (Green). (b) Fractional difference of the yield extrapolated to V_s=0
V and the extrapolation to 2 V (red), 5 V (black), 10 V (blue), and 20 V (Green).

4.3.2.4 Electron Emission Spectra

Electron emission spectra were taken to provide further insight into the charging behavior of Al_2O_3. Data were taken with a DC beam at incident energies ranging from 30 eV to 3500 eV and represent energies in both the positive and negative charging regime as seen in the pulsed yield curves in FIG. 4.30. It is important to recall from Section 3.1.2 that the resolution of the incident electron gun is limited to the tenths place on the controller display, so at incident energies <100 eV the BSE peak can be measured as part of the emission spectra and is accurate. At incident energies >100 eV, the BSE peak is not measured and must be inferred from the controller and has an error of ±5 eV.

E_1 is estimated to be 74±8 eV and the E_2 is approximately 3290±50 eV. If the incident energy used to measure the emission spectrum falls between these energies, we would expect to see positive charging; all other energies should produce negative charging. There is no evidence given in the emission spectra to indicate positive charging, there should only be the sample and backscatter peak visible (the backscatter peak will only be visible if the incident beam is <100eV). Negative charging will manifest as dual low-energy peaks; one peak from the sample and the other from the inner grid. For a full discussion of electron emission spectrum see Section 3.1.2.

As can be seen from the data in FIG. 4.35, the typical charging behavior is not observed in this material. These spectra were taken at an incident energy $<E_1$ and should induce a negative surface potential. This would be evident by the presence of dual low-energy peaks like those seen in Section 3.1.2, with one static peak at about 2 eV originating from the inner grid. If the material is negatively charged (as we would expect it to be in FIG. 4.35a-d) there would be another peak a few eV to the right of the inner grid peak, as seen in FIG. 3.5. This second peak originates from the sample, and its position in relation to the inner grid peak gives the negative surface potential. The fact that we do not see this peak from the sample could mean one of three things. First, the

sample peak could be shifted to energies >-100 eV, and would require a surface potential <-100 V to be observable. We estimate the first crossover energy to be 74±8 eV so 4.3.7c at E_o=58±1 eV should be the first to show negative charging. It would be surprising to find that a material could charge to > -100 V within just ~10 eV of the crossover energy. However given the extreme yields measured from this material, this explanation gains credibility.

Second, the sample is charging positively and the sample peak and the inner grid peak are both components of peak 1 in FIG. 4.35a. If this were true, the material would be charged positively in a region with a total yield σ<1. While the phenomenon of potential reversal is unusual, it is not without precedent in the literature for Al_2O_3 (Melchinger and Hofmann, 1995; Cazaux, 1999). These referenced studies were conducted using a DC beam similar to the electron emission spectra described in this section. These works are applicable to measurements using a DC beam that charges the material to an equilibrium state as was done with the spectral measurements presented here.

Third, in Section 4.2.3 we presented the idea that it is not the surface potential that dictates the emission energy of a SE. Rather it is the electric field at the point of SE generation that is important. These measurements were taken with a DC beam, the sample had reached it equilibrium voltage, and all of the internal charge distributions had been firmly established. Therefore, the chronology of measurement would be important in understanding this explanation; unfortunately this information could not be extracted from the available data here. However, one could imagine a scenario where the beam establishes an internal distribution that would cause the results seen in FIG. 4.35. This is the most likely explanation of these results, but would require extensive study to support this theory.

These figures show that the sample is charging positive or that it is charging negatively very quickly. We do not see the emergence of the dual peak until FIG. 4.36h taken at 100 eV. This incident energy is in the place on the yield curve ($E_1<E_o<E_2$) that would suggest positive
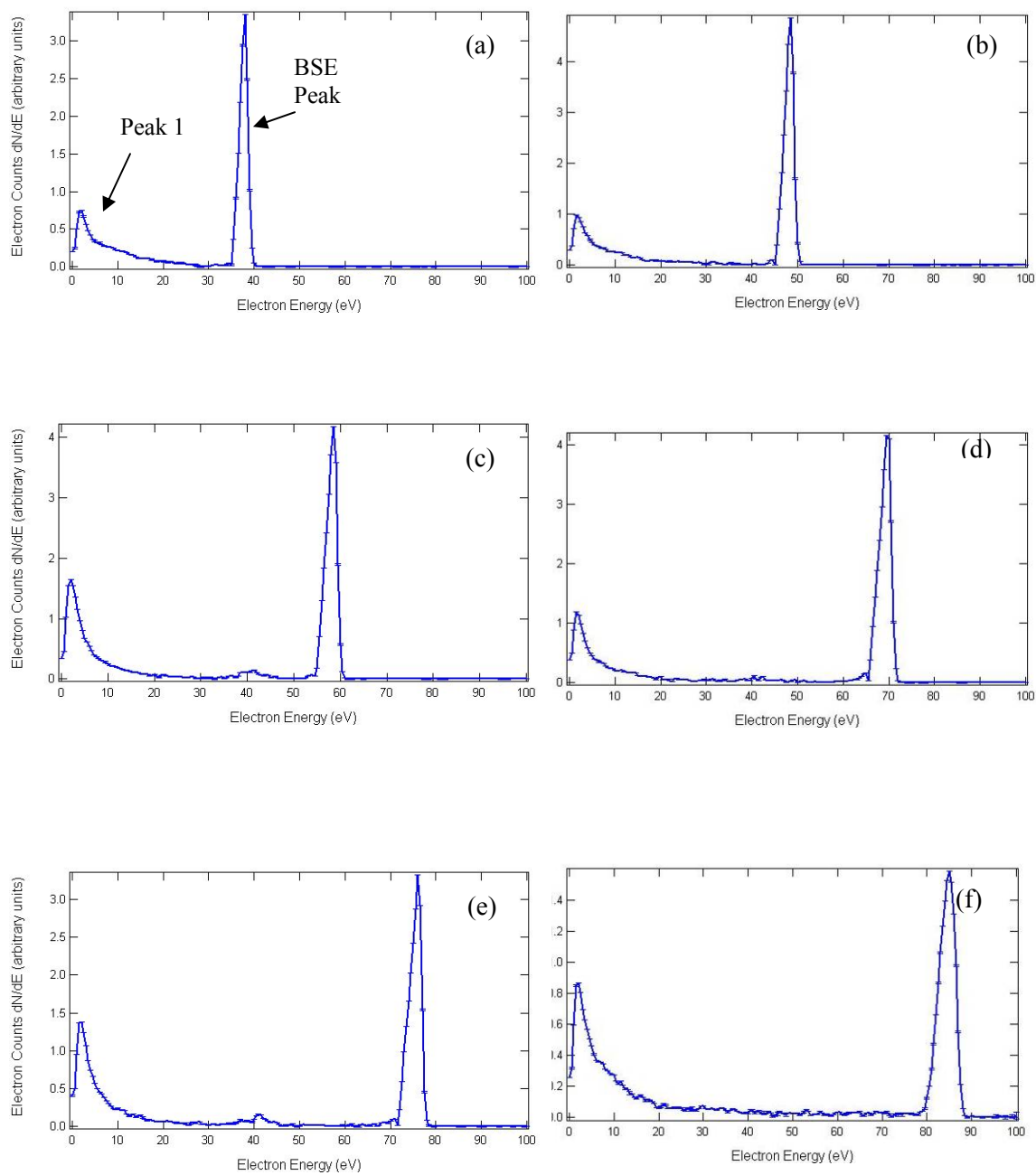
FIG. 4.35. Electron emission spectra of polycrystalline Al_2O_3.
(a) E_b=38±1 eV, (b) E_b=49±1 eV, (c) E_b =58±1 eV, (d) E_b=70±1 eV, (e) E_b=76±1 eV, (f) E_b=85±1 eV.
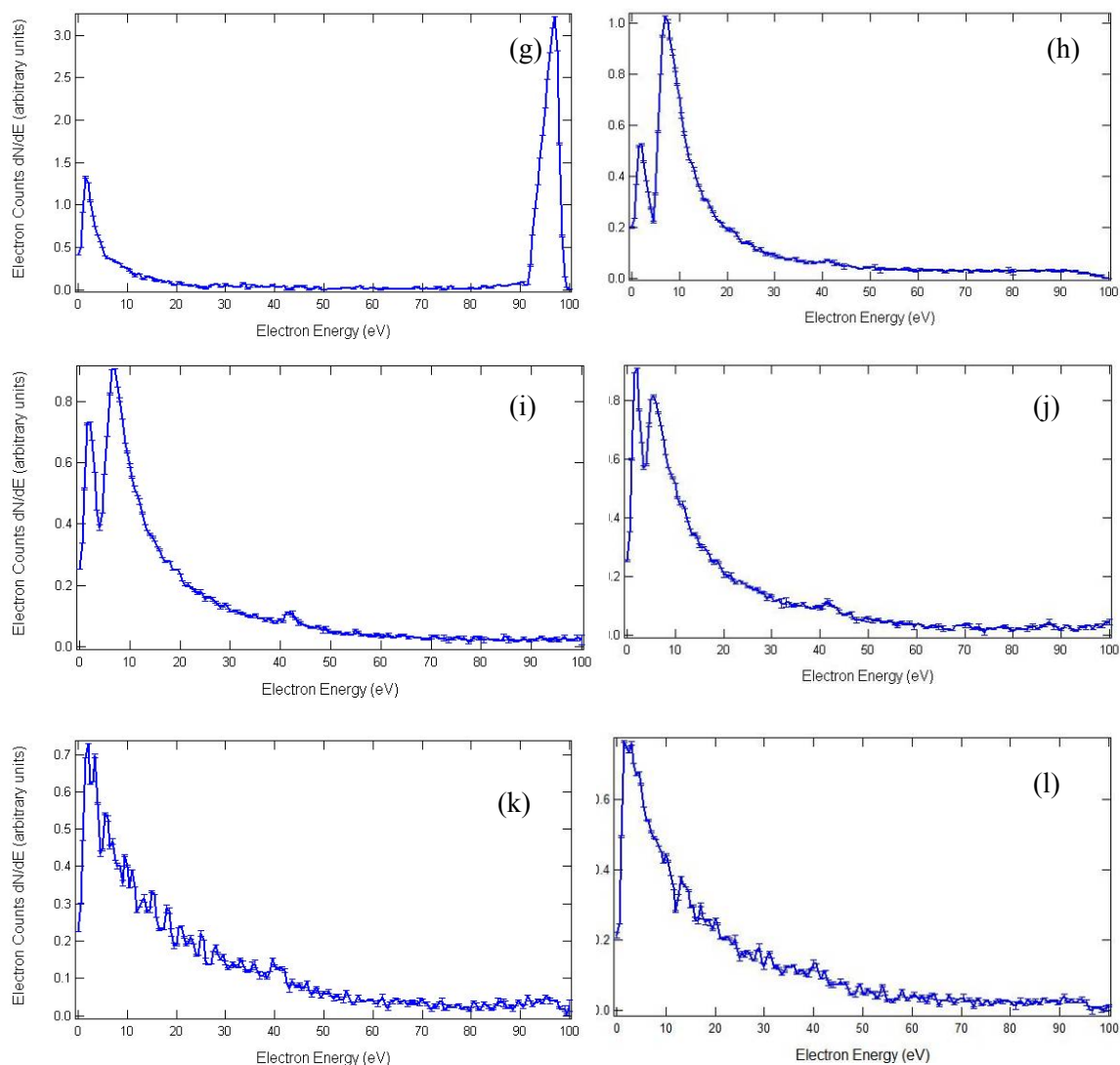
FIG. 4.36. Continued electron emission spectra of polycrystalline Al_2O_3.
(g) E_b=96 eV, (h) E_b=105±5 eV,(i) E_b=205±5 eV,(j) E_b=505±5 eV, (k) E_b= 3005±5 eV, (l) E_b= 3505±5 eV.

charging; dual peaks here are unexpected. This reversal in charging behavior continues as the incident energy increases, as seen in FIG. 4.36h-j. Further, in FIG. 4.36k-l the sample peak is lost again. All in all, this sequence is exactly opposite from what we would expect to see at these energies, and is consistent with both the second and third theories provided in the paragraph above.

This, along with the irradiated Kapton data presented in Section 4.2.3, could be an indication of some significant findings. These behaviors have not been noted in the spacecraft charging community and could provide significant insight into the dynamic nature of materials and how they accumulate and store charge over time. These data and connection to the literature is not meant to be definitive, and much work remains to be done before these thoughts can be verified. For the time being, we make the assumption that the pulse yield charges the sample in the conventional way, the methods used in the sections describing the pulse yields are valid, and the anomalies seen in this section are caused by the use of a DC beam.

4.3.3 Comparison to Literature

Two important questions are raised by this study that will be pursed in future work. First, we note that some previous studies of the electron yield curves of high-yield, high-resistivity insulators using very high-fluence beams (many orders of magnitude higher than our study) have measured yield curves similar to our intrinsic yield curves, rather than double peak or unity yield curves characteristic of a highly charged sample (Dawson, 1966; Osawa *et al.*, 2003; Whetten, 2004). A comparison of the pulse yield, composite yield and that of Lucalox are shown in FIG. 4.37. Lucalox is manufactured by General Electric and is the trade name for a high density, 99.9% pure polycrystalline aluminum oxide ceramic used in high-temperature applications such as arc lighting (Whetten, 2004). The method of manufacture is proprietary and there is little information regarding the specifics of these materials in general. There is also little known about the test conditions for red literature data presented for comparison in FIG. 4.37. Although the paper that this data comes from is very vague, we can make some assumptions about test conditions. Often studies, such as those describing Lucalox, use highly focused rastered beams from AES or SEM systems, with beam diameters <1 μm and fluxes 10^4-10^6 times higher than our studies. There is also some reference to the sample being at an elevated temperature,
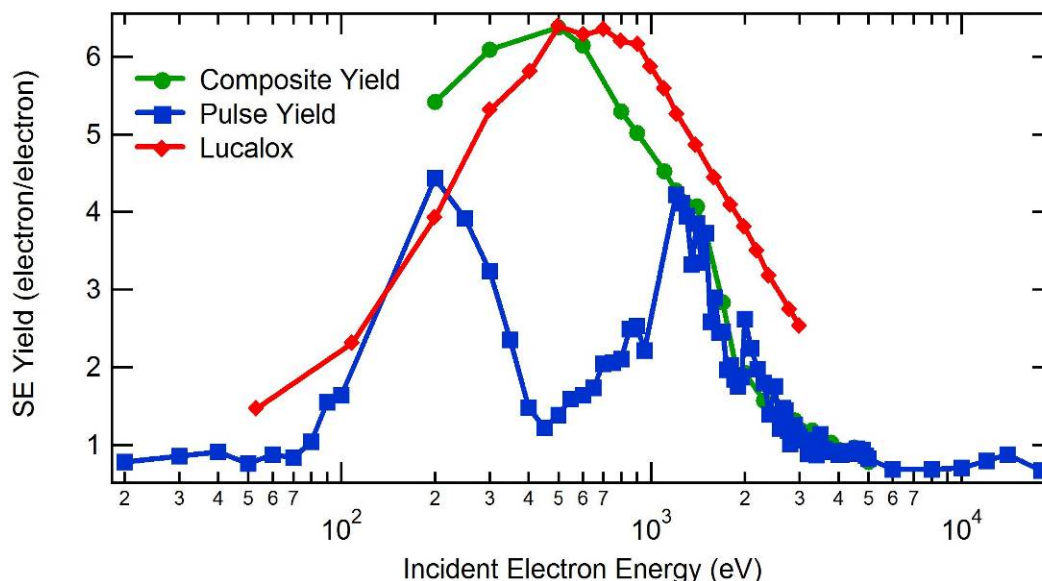
FIG. 4.37. Yield on Al_2O_3 taken with three different methods.
The blue squares are from measurements using the traditional pulse yield system. The green dots are a result of the composite yield extrapolated to 0 V surface potential. The red diamond shows the data taken from the literature on Lucalox. Note the good agreement in the yields of Lucalox and the composite curve. Further there is good agreement in all three yields at 200 eV $>E_b$ >1100 eV.

possibly as high as 1500 K. This would be consistent with the principle use of Lucalox in high temperature lighting application.

We speculate that the local sample resistivity of the insulator may be greatly reduced due to radiation induced conductivity (RIC) or elevated sample temperature, leading to charge dissipation within the sample. We have already shown that sample temperature can alleviate material charging in Section 4.3.2.2. So heating might be an explanation of the Lucalox results; however the paper is very vague on this point and there may be no heating at all. In addition to the thermally assisted conduction mechanisms for dark current conductivity, electrons can be excited into the conduction band by high-energy incident radiation and then thermally move in and out of trap states near the conduction band edge as they travel in the conduction band under the influence of an applied electric field (Rose, 1951; Fowler, 1956; Dennison *et al.*, 2008; Sim,

2010). This insulator conduction mechanism is referred to as radiation induced conductivity (RIC) and has been introduced in Section 4.1.2.5. We note that RIC persists for some time after the beam is turned off, so that this explanation could also be applicable to pulsed or rastered probe beams.

For a Kapton HN sample, a rastered 1 keV incident energy with an estimated penetration depth of 30 nm, at a 10 A-mm^{-2} effective beam density produces an average absorbed dose rate of 10^5 Gy and a radiation induced conductivity of 10^{-10} Ω^{-1}-cm^{-1} (with 10^{-2} s decay time), 10^9 times larger than the zero dose rate dark current conductivity (Dennison *et al.*, 2009a). In Kapton HN radiation induced conductivity persisted above 10% of the equilibrium dose rate value for >100 s (Dennison *et al.*, 2007; Dennison *et al.*, 2008).

With limited RIC data available for polycrystalline aluminum oxide, performing the same type of analysis as stated above is difficult. There are parameters available for k_{ric} and Δ (k_{ric}=6·10^{-9} (Rad·sec^{-1}·Ω-cm)$^{-1}$, Δ=1.0) in the literature (Donegan *et al.*, 2010). Assuming a 10 A-mm^{-2}, as above and a penetration depth R of 11 nm we can calculate a dose rate of 2·10^{14} Gy-s^{-1} by using Eq. (4.0). Now using Eq. (4.1), we calculate an equilibrium RIC value of 1·10^{-8} (Ω-cm)$^{-1}$. This relatively high conductivity means that in the context of our work this type of modification essentially makes the material a conductor.

This would explain why the measurements shown for Lucalox and other material show no evidence of charging despite the intense probe beam used to make the measurement. The beam is essentially discharging the material as the measurement is made by pushing a significant number of conduction electron into the conduction band where they can dissipate to ground. It remains to be seen if this method of discharge gives an intrinsic yield of a material, but it can be said that it is not representative of what will be encountered in terms of spacecraft charging. Spacecraft will never encounter fluxes at the level seen in this discussion, so application of this method to spacecraft modeling is not valid. It should also be noted that RIC, enhancements

should be considered in all ground-based spacecraft charging tests (Dennison *et al.*, 2009c). Since the dose rate is relatively low and the missions are long, accelerated testing is often used to test spacecraft materials. That is to say that because of RIC one cannot increase the electron flux in the test to avoid the long exposure times seen in space because doing so causes RIC to be a more significant factor than it otherwise might be.

This explanation is closely related to a study of Green and Dennison of the measurements of resistivity by the charge storage method for an intense, rastered proton beam (Green and Dennison, 2008). In this study RIC is used to explain results of surface potential measurements. These measurements are made by irradiating a material with a proton beam and measuring the surface potential over time to determine material conductivity. The results of these tests are explained by using RIC to model the redistribution of internal charge. This redistribution is defined by the DC and RIC conductivities and has been used in the arguments in the paragraph above.

CHAPTER 5

SUMMARY AND CONCLUSIONS

The primary focus of this thesis has been to experimentally study the electron-induced electron emission and overall charging properties of common dielectric materials. This study has precipitated the development of state-of- the-art equipment and measurement techniques. Of key importance to this work are the high precision measurements of minimally charged insulator electron yields and the development of predictions of how these yields are modified by accumulated surface potential. A model has been developed to describe surface potential and its relation to the total yield by combining other models for electron emission spectra and internal charge distribution (Hoffmann *et al.*, 2008). This combination has allowed us to extrapolate to the uncharged yield on materials that would not otherwise be measurable. We have also introduced the idea that no discussion of the intrinsic yield is complete without consideration of the materials DC and RIC conductivity (Frederickson and Dennison, 2003; Compton *et al.*, 2004; Dennison *et al.*, 2008). Furthermore, separate continuous beam electron emission spectra have been taken to understand the interplay of surface charging and secondary electron re-capture mechanisms.

The key advances in this research were: (i) development of state-of-the-art methods and instrumentation for measuring electron yields and emission spectra from insulating materials, particularly for low-fluence pulsed-beam techniques, (ii) development of a quantitative physics based model that accurately predicts total electron yield as a function of surface potential and incident flux, (iii) inclusion of conduction mechanisms in understanding charging behavior as they relate to total electron yield modifications.

These capabilities have offered vast improvements in capability when compared to previous electron emission studies reported in the literature (Dawson, 1966; Willis and Skinner, 1973; Thomson, 2004). The measurement of absolute total, secondary electron, and backscatter electron emission properties of insulators and conductors provide important new data for the

spacecraft charging modeling codes (Levy *et al.*, 1985). This work also has broader implications, which include scanning electron microscopy, surface spectroscopy methods, particle detectors, plasma fusion devices, dielectric arcing, and flat panel displays (Seiler, 1983; Schwoebel and Brodie, 1995; Shih *et al.*, 1997b; Auday *et al.*, 2000; Belhaj *et al.*, 2000; Reimer, 2000).

To underscore the importance of yield in the modeling of spacecraft charging, FIG. 5.1 shows the equilibrium voltage, V_{eq}, that develops on a simple spacecraft (a flat sheet) as a function of the total yield of the material this hypothetical spacecraft is composed of (Kapton HN). This is accomplished by modeling the Kapton sheet in the Spacecraft Charging Handbook (the current software used by NASA to predict surface potential) (Mandell *et al.*, 2001) and changing the material parameter σ_{max} only in a manner similar to that in Chang (2000b). It is modeled in a low-Earth orbit with average environmental conditions and in eclipse without the effects of photoyield. It is easy to see in FIG. 5.1 that a modest error of <10 % in the determination of the total yield can lead to a dramatic shift in the predicted equilibrium surface voltage from +10 V to -10,000 V. This type of miscalculation could have several consequences. If, due to a yield error, the model predicts -10,000 V surface potential, then there would be considerable cost and effort wasted to fix a problem that does not exist. On the other hand, if the model predicted +10 V equilibrium potential, the craft could have a significant problem that would not be addressed until the craft is in orbit, and by then, mitigation options would be limited. These scenarios are extreme, but must be considered. In the end, it all comes down to accurate measurement of the materials involved.

All of this work has been done for use in understanding spacecraft charging and specifically for incorporation in spacecraft modeling codes. The measurements that have provided material properties in the past have been sparse, unrepeated and in the case of many extreme insulators, little more than an educated guess (Levy *et al.*, 1985). This study has provided
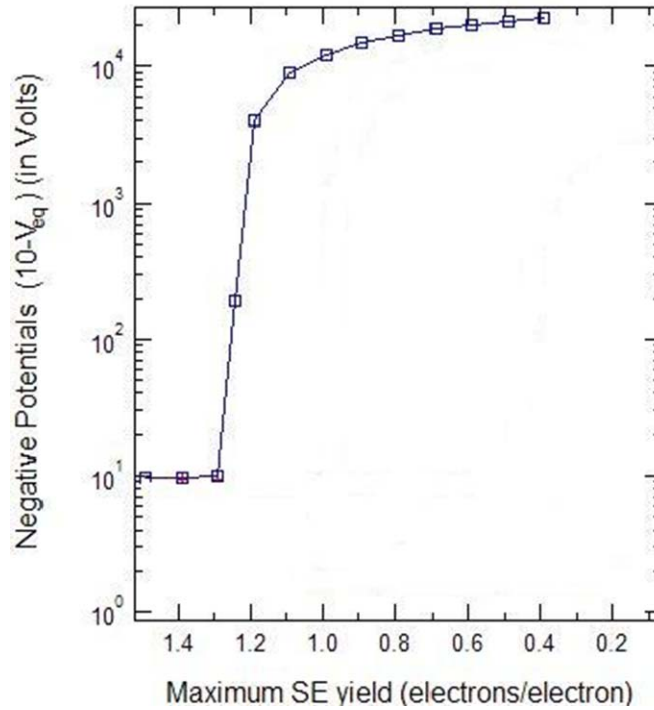
FIG. 5.1. Equilibrium surface potential of a Kapton sheet in orbit.
This is modeled in average environmental conditions as the maximum total yield σ_{max} of the material is changed. This was modeled in the Spacecraft Charging Handbook and show how modest error in yield determination can have dramatic effects on the predicted surface potential.

an instrument and methods that can give repeatable results for even the most charge susceptible materials. This was done through the development of theory that has been presented in the literature (Hoffmann *et al.*, 2008). It has been shown that these methods can provide accurate measurements for materials with total yields ~7 and a conductivity of ~10^{-19} (Ω-cm)$^{-1}$. At ~10^{-19} (Ω-cm)$^{-1}$ the charge decay time is much longer than the relevant time scale of a few seconds for these experiments; this allows us to extend the applicability of these methods to materials with resistivities $\rho \rightarrow \infty$. The yield of polycrystalline aluminum oxide as been measured with the decay curve method to have a maximum total yield σ~7 (Donegan *et al.*, 2010). There are materials that have a higher maximum total yield σ_{max} than aluminum oxide, such as diamond, which has a negative electron affinity and a theoretical maximum yield $\sigma_{max} \approx 40$ (Shih *et al.*, 1997b). The

factor that limits how large the maximum total yield can be is how few data points can be taken in a yield decay curve before the material is fully charged. We have shown that this method can provide more than enough decay curve data to apply the model and extrapolate the zero charge yield. If the yield were ~40 the fit could still be applied, it would just have five times fewer points. This would increase the uncertainty of the extrapolation, but would still provide a reasonable measurement.

The parameters of maximum total yield and conductivity dictate the charging susceptibility. This allows us to illustrate the demonstrated and predicted capabilities of the methods described in this work; they are shown in FIG. 5.2. In short, we have demonstrated a method's applicability to a wide variety of materials and have predicted that these methods can be used to measure materials with any degree of charging susceptibility from conductors (low-yield; high-conductivity) to diamond (high-yield; low-conductivity). It should also be me mentioned that the methods described herein are applicable over the entire range of both yield (from 0 to 40) and conductivity (from 0 $(\Omega\text{-cm})^{-1}$ to $\rightarrow\infty$ $(\Omega\text{-cm})^{-1}$). This range covers the entire known spectrum of these two materials properties. In addition, this work has also provided great insight into physics of material charging by providing a physics-based approach to determining the electron induced electron yield of insulating materials.

5.1 Summarization of Thesis Sections

Chapter 2 developed the theoretical models for electron emission and for the internal charge distribution resulting from electron irradiation of insulators, culminating in the analytic model of the electron yield from insulators as internal charge is accumulated.

In Section 2.1 a basic description of electron yields were presented, representative of nearly all conducting and insulating materials. This included definitions of total electron, secondary electron, and backscatter electron yields and how these yields can be measured
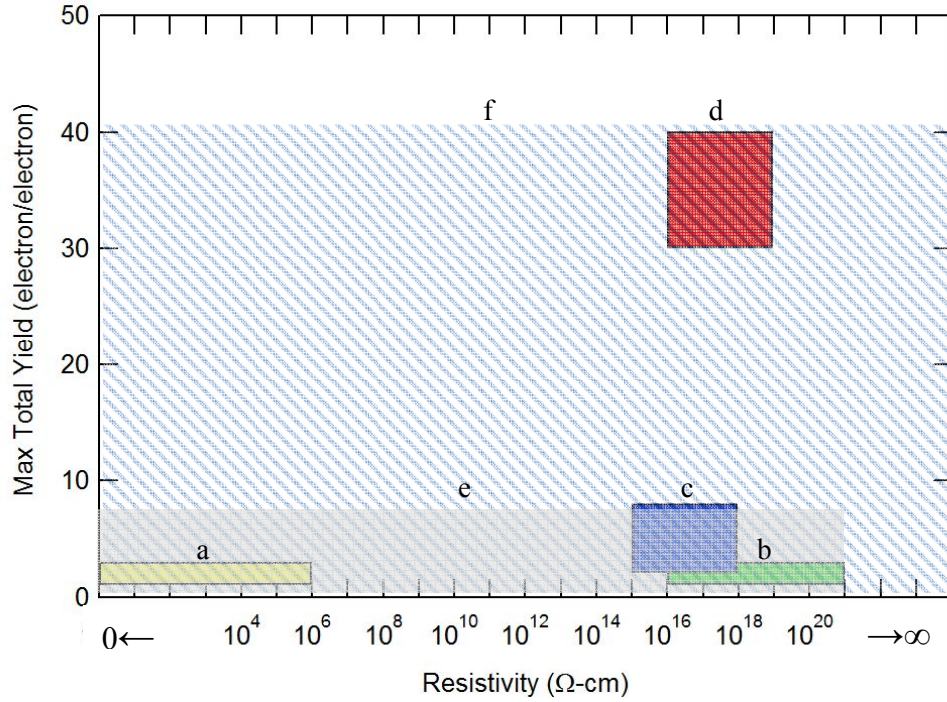
FIG. 5.2. Depiction of the range of measurable materials.
(a) Conductors and semiconductors. (b) Polymeric materials such as Kapton HN. (c) Metal oxide ceramic materials such as aluminum oxide. (d) Negative electron affinity materials such as diamond. (e) Range of material properties tested in this work. (f) Applicability of methods developed herein to all materials.

experimentally by summation of currents (Thomson, 2004). This section also qualitatively describes how surface potential affects total yield.

Section 2.2 describes the mechanisms involved in the energy distribution of secondary electrons, and provides a review of the physics-based Chung and Everhart (Chung and Everhart, 1974) model that describes secondary electron emission spectra of conductors. This model was then extended through the work of Thomson (2004; Baroody, 1950; Quinn, 1962) to be generally applicable to dielectric materials through the substitution of the insulator electron affinity χ, for the work function ϕ. Building on this foundation, the yield of a material was described in terms of the secondary electron emission spectrum, which naturally leads to the inclusion of surface potential in the general model.

The internal charge distribution that develops as a result of incident electron bombardment on insulators and the concominant surface potential were described in Section 2.3. This section reviewed a progression of increasingly sophisticated models of internal charge distribution. It started with a simple conductor with an internal charge distribution dictated by Gauss' law (Griffiths and Inglefield, 1999), and progressively built to the dual dynamic layer model (DDLM) that describes the complex layering of charge that results from electron beam radiation (Melchinger and Hofmann, 1995). This model allowed the prediction of surface potential as a function of incident flux, and provides a crucial element in the modified Chung-Everheart model to predict electron yield as surface potential develops and SE recapture is initiated. Confirmation of the predicted surface potential of polymeric insulators under electron beam bombardment, to be measured by Hodges (2010), will provide critical validation of this intermediate prediction of the theory developed in this thesis.

Section 2.4 combined the DDLM from Section 2.3 and the expression developed to predict electron yield as a function of surface potential from Section 2.2, to form an empirical model that predicts what fraction of SE will escape from a given surface potential and ultimately how the total yield reacts to an evolving positive surface potential. It is this comparison of this theory with our measurements of yield decay curves, electron emission spectra and electron yield curves as charge accumulates that are the central result of this thesis.

Chapter 3 provided a general description of the USU equipment and facilities used to measure electron emission properties of materials as they accumulated charge, and measurements used to evaluate the verisimilitude of the theories presented in Chapter 2. This section provided a description of all of the instrumental upgrades that have been implemented to study the effects of charge accumulation on emission and to describe the extensive validation measurements made to characterize these improvements. Of particular importance was the characterization of systematic

errors of <5% for conductors and <10% for insulators and the demonstration of yield measurements using pulses of <3 fC/mm^2.

Section 3.1 was devoted to DC (direct current, continuous beam) measurements and is presented here to validate the basic functionality of the detector after upgrades described in Chapter 3 (Nickles *et al.*, 2001; Thomson, 2004). The hemispherical grid retarding field analyzer was described in general terms and basic functionality of this detector and its efficiencies were discussed. The upgrade most relevant to this section was the electrical isolation of the inner grid to allow positive surface potential to be measured using the spectral shift method described in Section 3.1.3. A DC spectrum taken from a grounded clean polycrystalline gold sample was presented as a gold standard from which to gauge all other measurements. Spectra were measured with several known external biases placed on the gold sample. These demonstrated that the secondary electron peak measured in the emission spectra was linearly proportional to the applied sample bias. It was also shown that other features (inner grid and BSE peak) of the electron emission spectra showed no response to the applied electric field of the sample. This set of measurements was used as a surrogate for more complex measurements of induced sample potential on insulators, and validated the spectral shift method as a viable, albeit limited, method of determining sample potential.

With the basic operation of the hemispherical grid-retarding field analyzer established in the preceding sections, Section 3.2 addressed the more complex measurements using the pulsed yield system. The basic operation of this system was developed by Thomson (2004) and has not been changed. What has been changed is the versatility and overall capability of this instrument. By way of extensive instrument characterization, the range of the primary electron source was extended from to 30 eV to 5 keV and the beam spot size was normalized to a FWHM value of 1.7 mm over the entire range of the gun. This allowed the flux density of each incident pulse to be maintained throughout the entire energy range of the Staib gun (Staib Instruments, 2002).

Section 3.2.1 was devoted to the concept of charge neutralization. As incident electrons interact with the material during the course of yield measurements, the material will inevitably adopt a potential. This potential must be dissipated before further measurements can be made. This section described two neutralization methods, namely low-energy thermionic electron charge dissipation shown to be effective at dissipating positive charge accumulation, and photon flooding to induce the photoelectric effect and dissipate negative potential accumulation (Jbara *et al.*, 2001). It was shown that the flooding of low-energy electrons is very effective at dissipating positive surface potential. Unfortunately, due to time constraints, the effectiveness of photon flooding could not be fully explored. This validation is included as an item of future work in Section 5.2. Also included in Section 3.2.1 was a discussion of the instrumental upgrades that have been implemented in the hemispherical grid retarding field analyzer; most notably are inclusion of Faraday cups that can be used for beam positioning and beam characterization during emission measurements.

Section 3.2.3 described upgrades in measurement methods that have led to a reduction in systematic error from previous work. A timing diagram showed the basic sequence of the pulsed yield system with special attention given to the rejection of erroneous data. There was an intermittent noise source of unknown origin identified that corrupts ~15% of the pulsed yield data. A method was developed using LabVIEW and a four-channel digital storage oscilloscope to examine the signal before and after every pulse, and based on this information, reject the data if it exceeded the user defined acceptable limit. These improvements lead to a 60% improvement in systematic error in yield measurements over previous studies.

Also put forward in Section 3.2.3 was the idea that the pulse itself may be able to be used for yield determination; due to limited data, this technique was outlined, but not fully explored. Throughout the course of this thesis, each incident pulse was integrated with respect to time, giving a total flux typically on the order of the few fC. Since the electronics are fast enough to

capture the evolution of the yield within each 5 µs pulse with sufficient resolution, it might be possible to calculate the yield on a point-to-point basis. This would raise the overall sensitivity of the pulse-yield system by at least a factor of 10 and allow greater understanding of the material dynamics as it responds to incident charging pulse. This has not been done in this thesis, but is presented as an item of future work in Section 5.2.

With a theoretical framework developed and the instrument characterized and validated with both grounded and bias conductors, Chapter 4 presented data measured with the pulse yield system on three separate insulating materials. These materials were chosen because of their applicability to spacecraft construction, but more importantly because of the varying degrees of susceptibility to charge accumulation they possess. Therefore, to determine the effectiveness of the pulse yield system for measuring the minimally charged yield of an insulator, we considered a progression of more challenging materials. First, we examined CP1, a material similar to Kapton HN; CP1 has a low total yield (σ_{max}~1.4) and a low conductivity (~10^{-19} (Ω-cm)$^{-1}$) (Dever *et al.*, 2001; ManTech, 2010). With a bulk conductivity in this range, the charge decay time will be several days and will, therefore, dissipate any charge build up in that time frame but not in the few seconds each emission measurement requires. Next, the polyimide Kapton HN was examined (DuPont, 2010). This material has a slightly higher yield (σ_{max}~2.2), and has low conductivity (10^{-19} (Ω-cm)$^{-1}$), again leading to a decay time of several days. This material is a good test of our discharge methods and is representative of most of the materials of interest for space-based applications. Finally, we considered polycrystalline aluminum oxide with a high yield (σ_{max}=7) and low conductivity (~10^{-16} (Ω-cm)$^{-1}$). This material accumulates charge quickly and retains it for tens of minutes. This material provided tests of not only our discharge methods, but also of our minimum probe pulse current and ultimately our systematic noise floor.

Section 4.1 presents the data acquired from CP1 and starts in Section 4.2.1 with a detailed material characterization including optical reflectivity showing an absorption edge at about 4.8

eV, which provided an estimate of the direct bandgap. This section also included optical micrographs of the material showing extensive physical damage to the material, attributed to manufacturing process or handling of the sample prior to its arrival at USU. Lastly, an estimate was given of the penetration depth or range R for CP1.

Section 4.1.2 presented the electron yield of CP1 as measured with the pulse yield system. These data gave a maximum total yield of σ=1.4 at E_{max} =170 eV and showed little evidence of charging at beam energies $<E_2$. Above E_2 negative surface potential began to modify the yield with a dramatic shift taking place at ~1500 eV when the surface potential reached $\geq$-50 and secondary electrons received enough kinetic energy from the electric field of the sample that they begin to register as BSE's. Several methods for determining the crossover energies were employed for this material with our best estimates being E_1=60±5 eV and E_2=640±20 eV. Electron emission spectra were also presented, and by using the spectral shift method described in Section 3.1.2 the crossover values were validated. A key result in this section was described in FIG. 4.8b where the entire yield curve was sectioned into six distinct zones of incident energy and the behavior was explained. These explanations for the features seen in CP1 were subsequently applied to Kapton HN and aluminum oxide; they provide a qualitative description for the features observed in these two additional materials.

Section 4.1.2.5 presented decay curve data of the yield resulting from charge accumulation of numerous features in Section 3.2.1 taken for CP1 at an incident energy of 300 eV. The yield of this material is low at 300 eV (~1.4), but its conductivity (~2·10^{-19}(Ω-cm)$^{-1}$) should ensure that any accumulated charge would remain for a long period of time. The decay curve, however, suggested that this might not be the case; it should have reached an asymptotic limit of one in very short order (~40 nC), but did not, suggesting that bulk conductivity was dissipating the charge as the beam was depositing it. It was proposed that radiation induced conductivity (RIC) could modify the bulk conductivity enough to cause this phenomenon. In this

case, the radiation induced conductivity was estimated to be $\sim 2 \cdot 10^{-16}$ $(\Omega\text{-cm})^{-1}$ (about three orders of magnitude larger than the dark current conductivity) and would therefore make the charge decay comparable to the experimental duration. This was presented as a theory and would need further examination for verification.

Section 4.2 examined the moderate-yield, low-conductivity material Kapton HN and began with a thorough material characterization as described above for CP1. This material was found to be very similar to CP1 in that it, too, had extensive physical damage when viewed under a microscope. Also, as with CP1, there was little evidence of charging at incident energies < E_2=775 eV, but at energies greater than E_2 the material began to exhibit significant signs of charging. The most notable of these was when the material reached a negative surface potential of more than 50 V and secondary electrons gained enough energy to be registered as BSE's, the same phenomenon as was seen for CP1. For clarity, the yield curve was again sectioned into five zones and each zone was explained within the context of surface potential.

Decay curves for Kapton were shown in Section 4.2.2.4 and revealed that the charge dissipation techniques for positive potentials (discussed in the instrument characterization Section 3.2.1) might not be completely effective. Namely, after many hours of pulse yield measurements, the decay curves no longer approached an asymptotic limit of unity. His condition was found to be alleviated by increasing the bulk conductivity through sample heating to 333 K for 6 hr. Decay curves taken after this thermal annealing treatment resulted in an asymptotic approach to unity as it is to be expected.

This discovery led to further investigations in Section 4.2.2.5 of decay curves, including the so-called dose decay curves. In these experiments, the yield was measured as a function of incident flux and it was found that dramatic changes in the total yield (60%) could be seen with relatively small flux changes ($\sim$10 fC) (Hoffmann and Dennison, 2006). This effect was not just seen in decay curves, but was also measured across the whole spectrum of energies used to take

total yield measurements. These results were discussed in Section 4.2.2.6, where it was shown that changing the flux contained in every pulse could have a dramatic effect on the total yield.

The last section devoted to measurements on Kapton (Section 4.2.3) was a collection of measurements made on previously irradiated samples. These materials were subject to intense electron beam radiation prior to this set of measurements with the intent of studying the effects that radiation damage had on electron yield and emission spectra. While this section was not meant to be a complete treatment of the subject, it was interesting to note that the electron emission spectra measured and presented here show dramatic changes in the behavior of Kapton after electron beam radiation. Most notably, when a continuous electron-beam of incident energy 200 eV ($\sigma > 1$) impinged on the sample to measure surface potential, the spectral shift method revealed that the material was charging *negatively* up to -28 V and that this negative voltage evolved over tens of minutes. It was speculated that this is due to the production of increased trapping states within the band gap (Connell, 2000; Dever *et al.*, 2001). We also speculated that the secondary electron escape energy was determined by the electric field at the point of origin rather than by the net electric field at the sample surface. The theories in this section are purely speculative, but they do provide tantalizing clues that could provide a wealth of information about Kapton and how radiation damage might modify the material.

From the charging perspective and for the purposes of this study polycrystalline aluminum oxide provides the most challenging material and was addressed in Section 4.3. This material has a low conductivity ($3 \cdot 10^{-16}$ (Ω-cm)$^{-1}$) (can store charge for tens of minutes) and an very high total yield (~7). The combination of these two material properties make polycrystalline aluminum oxide exceptionally good at gathering and storing charge, and provides conditions that tested the capabilities of the instrumentation and methods developed herein. Material characterization was difficult due to its proprietary nature and limited specific information, but a general treatment of aluminum oxide and its possible contamination origins are presented. Results

for most of the characterization tests and calculations done for CP1 and Kapton were presented for aluminum oxide.

Section 4.3.2.1 displayed data taken from the pulse yield system on polycrystalline aluminum oxide and showed evidence of significant charging at energies between the crossover energies (E_1=74±8 eV, E_2= 3290±50 eV). CP1 and Kapton both showed evidence of charging, but always in the negative charging regime where the effects are more easily explained and quantified. Polycrystalline aluminum oxide showed little charging effects in the negative charging regimes, but dramatic effects in the positive charging regime. The magnitude of the effects was not quantifiable using traditional pulse yield methods. For this reason, in Section 4.3.2.2 the material was heated to 348 K to thermally enhance the conductivity of the material, thereby reducing its charge susceptibility. This approach showed some relief from the effects of charging, but ultimately did not alleviate the problem.

Therefore, in Section 4.3.2.3 the theory developed in Chapter 2 was employed to extrapolate a yield decay curve back to its uncharged value. Decay curves were then taken at a spectrum of energies ranging from 200 eV to 5000 eV and all were extrapolated to a zero surface potential. In this way, it was possible to use a combination of experimental data and the theoretical models from Section 2 to predict an intrinsic yield on materials that would not otherwise be measurable. This method not only gave information about the intrinsic yield, it was able to predict yield curves as a function of surface potential or equivalently, using the DDLM, as a function of incident flux. This method correctly predicted the emergence of the dual peaks seen in the data. It also predicted a reasonable value of σ_{max}~7, consistent with other available (but limited) yield data for bulk aluminum oxide. Further, it served to corroborate the explanations developed to qualitatively describe the numerous features observed in the different energy regions of the yield curves attributed to charge accumulation. The agreement between the model for

intrinsic yield curves and the measured emission properties of the most challenging aluminum oxide samples is the most significant accomplishment of the work presented in this thesis.

Finally, in Section 5.2, a path forward is presented that further explores all the loose ends and ideas that have been presented in this thesis. Further work in determining dose dependence of yield modification is outlined in Section 5.2.1 and includes a method of determining the total yields on the fly as the pulse progresses through its 5 μs duration. In Section 5.2.2 a method is proposed to recreate literature results using a high flux density beam to take the yield in concert with direct surface voltage measurements to confirm or invalidate the idea that RIC might be responsible for results seen in the literature. Finally, we will build on the previous section to use the surface voltage measurements to support the models put forth in Section 2.3, namely the DDLM for internal charge distribution.

5.2 Future Work

This work provides a solid foundation for the measurement of electron yields, but there are several experiments that could be done to strengthen the argument and prove or improve some of the assumptions that have been made throughout the text. This section provides a clear way forward for the Materials Physics Group at Utah State University with the overall goal of advancing the field of spacecraft charging. It first outlines the concern raised in the text and then proposes a set of experiments to answer the associated questions. The experiments described in this section are mentioned as an outline only; the details will be left up to future researchers.

5.2.1 Dose Decay Curves

The dose decay curves described in Section 4.2.2.5 were taken by measuring the yield at constant incident energy, but changing the total fluence in each pulse. In the theory developed in Section 3 the total flux is not what is required; rather it is the flux density, given in current per unit area. To explore this difference the following measurements should be made.

The methods described in Section 3.2.4 should be used to determine settings for beam spot sizes of 1 and 5 mm. These settings will bracket the measurements shown here at 1.7 mm. Dose curves, like those presented in Section 4.2.2.5, should be taken at 1 mm and 5 mm spot size settings. This will establish the dependence of charging on, not only the total flux, but the more correct flux density. These results will also have important implications for understanding the effects of RIC on electron yield, charging and discharge.

Changing the duration of the incident pulse will also provide another method of establishing the dependence of the charging on the total flux. This will help clarify the total flux dependence, but does nothing for the flux density dependence.

5.2.2 Inclusion of Conductivity in Model for Flux Dependent Yield

The model developed in Section 2 has been effectively applied to model how the total yield will respond to surface potential. This was accomplished by making several assumptions; one of which was that the internal charge distribution was static once established. In other words, the materials' total conductivity was assumed to be infinite. This is, of course, not generally a valid assumption for all materials and was used only as a proof of concept in this work.

Inclusion of conductivity should be relativity straight forward and will closely follow the work by Roth *et al.* (2008, 2009). This work models the charge deposited in the material as a single slab. It derives the electric field within the bulk of the material and ultimately the current moving in two directions. One direction is up/toward the incident surface from the deposited charge layer toward the incident beam; the other current moves down/in the opposite direction from the charge layer to the grounded substrate. Roth (2009) models the current going up in terms of the RIC and the DC conductivity and the current going down in terms of the DC conductivity only. This leads to two charge transport terms for the single charge layer in this model. This model is extended to ungrounded top surfaces in Hodges (2010) and Sim develops an extensive theory of charge accumulation and dissipation from an electron transport perspective (Sim, 2010).

This method can be used in our application simply by taking each of the three layers predicted by the DDLM in Eq. (2.19) in turn, and applying the same techniques as Roth did for a single charge layer. This will give currents flowing both up and down for each layer, and when summed, will provide an expression for the total current flowing within the material. It is a simple matter after this to relate the current flowing to and from each of the layers to the total charge deposited, dissipated and ultimately the surface potential.

The addition of finite resistivity into the DDLM will increase the model's applicability to the problem of material charging by allowing the measurement of high-yield materials that have charge decay times on the order of our experiment (a few seconds). Such a theory could produce a fit to electron yield decay curves such as that for CP1 in FIG. 4.12 for CP1 with relatively high conductivity. It might also yield new information about the material, such as the DC or RIC parameters. These parameters might be fitting parameters to the measured decay curves. This would provide a relatively easy method of determining these parameters compared to current methods that are both costly and time consuming (Dennison *et al.*, 2007).

5.2.3 Reproduction of Literature Results

It is not possible for us to reproduce the exact conditions that are typically used to measure the electron yields in insulators in high flux SEM or AES systems; our chamber is not a SEM and has no raster capability. However with modest modifications it may be possible to use some existing instruments to reproduce SEM conditions. With no modification, however, we are able to create a high-fluence pulse. According to the manufacturer of our primary electron gun (Staib Instruments, 2002), we can achieve 80 μA of beam current and a spot size of 80 μm. This would produce a beam density of 0.02 A-mm^{-2}. While this is considerably less than the beam densities seen in a SEM, we estimate the radiation induced conductivity for Kapton^{TM} to be 10^{-12} $(\Omega\text{-cm})^{-1}$, with a charge decay of ~1 s. The RIC effect should still play a significant role in

dissipating any built up charge and be apparent in the following measurements. The experiment would proceed as follows:

- Use the Faraday cup to determine the settings needed for maximum beam current and constant beam spot size.

- Measure the total and backscatter yields using these settings, with the shortest delay possible between pulses, and no flooding on Kapton and polycrystalline aluminum oxide. Do this for energies ranging from 50-1500 eV.

- Use a DC beam and the tightest possible focus to measure the SE and BSE yields on polycrystalline aluminum oxide. This will approximate literature test conditions.

- Repeat the above experiment with electron flooding durations of 1, 3, and 5 seconds. This will indicate any dependence on low-energy electron flooding.

- Use the newly developed surface voltage probe (Hodges, 2010) to measure surface voltage during these various experiments to directly measure the net accumulated charge.

These experiments will approximate the condition in a SEM and provide information about the RIC influence and its dependence, if any, on flooding during the pulse yield cycle. If RIC is a significant factor, the dual peaks seen in our low-fluence pulsed yield measurement (e.g. FIG. 4.30) should not appear. In addition, collaborations are planned with Dr. Jbara at the *Université de Reims* in France to make measurements for comparison using his SEM system.

5.2.4 Surface Voltage Measurements

Work is underway to add a moveable noncontact electrostatic field probe (Hodges, 2010) to the existing HGRFA detector used in pulse yield measurements. This will allow the measurement of the surface potential *in situ,* while pulse yields are being measured. This upgrade will allow the following measurements to be made.

Surface voltage measurements will provide the means to verify the decay curve method of determining electron yields by measuring the surface potential rather that inferring it from the DDLM. While the DDLM is a venerated method of inferring surface potential, it introduces a level of uncertainty by using it in the context of this study. By measuring the surface potential rather than inferring it, we greatly enhance the strength of the arguments presented here.

The charge storage method is a very sensitive technique for determining the bulk resistivity of highly insulating materials (Fredrickson and Dennison, 2003; Swaminathan, 2004; Hodges, 2010). We first charge an insulator up to a large surface potential by depositing a thin layer of electrons near the surface using an electron gun. Measurements of the potential are then taken with a non-contact electrostatic field (Flipper) probe that can make the measurement without disturbing the charge distribution (Hoffmann *et al.*, 2009). Over time, the electrons will migrate through the material to the grounded sample mounting plate. This depletion of electrons will manifest as a roughly exponential decrease in surface potential (Dennison *et al.*, 2007; Sim, 2010). By making surface potential measurements over time as charge decays, we can infer the bulk resistivity of the material (Green and Dennison, 2008).

If RIC plays a significant role in discharging the material, as we have suggested, then this will be evident in the non exponential nature of the charge decay. RIC persists for >100 sec after the radiation is turned off, so we would expect to see a quick decay of the surface potential in the initial tens of seconds after the beam is turned off. The rate of decay will then slow until it reaches the much lower dark current conductivity. The following set of measurements will provide the data needed to examine RIC as an explanation for the discrepancy in our traditional pulse yield measurements to those of the literature, as described in Section 4.3.3.

- Use a well characterized high-fluence electron beam to charge Kapton with a known dose and dose rate, and measure the surface potential for several hours after charging has ended.

- Repeat this basic experiment with different parameters such as dose rate, spot size, beam energy, material thickness, and material type.

Charge layering was postulated as a possible cause for the apparent change in charging behavior seen in irradiated Kapton and polycrystalline aluminum oxide in Sections 4.2.3.2 and 4.3.2.4. This was evidenced by using the spectral shift method of determining surface potential. While we have shown that this method is valid, it remains an indirect and less precise method of determining surface potential. Measuring the surface potential immediately after spectra, like those in the sections mentioned above, are finished will give insight into the nature of the phenomenon. This is similar to the work done by Green (Green and Dennison, 2008), and like his study, might provide insight into, not only the net surface potential, but also the interplay of charged layers as they recombine.

Throughout Sections 4.2 and 4.3 we have used the idea that the potential at the SE production site is the potential barrier that must be overcome to contribute to the yield. This supposition could be confirmed by measuring the surface potential as the yield is measured. The penetration depth is dictated by the incident electron energy, so it is possible to control the depth of the penetration electrons. Using a low-energy beam, it may be possible to determine a relationship of penetration depth and surface voltage.

It would be beneficial to measure charge accumulation curves of surface voltage at numerous energies along the CP1, Kapton HN, and Al_2O_3 to test our speculations about how charge is affecting total, SE, and BSE yields. I would recommend that these tests be conducted in each of the six zones indentified in FIG. 4.8.

Surface voltage measurements will also shed some light on the anomalous behavior seen in zone 4 in FIG. 4.17. The argument was made that the electric field was enhancing the production and escape mechanisms for SE's. This enhancement was evidenced by an increase in the total yield to values above one at beam energies higher than the second crossover. This

second peak leads to an effective crossover point at a much higher energy than the first. Data regarding the surface voltage will shed some light on this result and allow incorporation of this behavior into existing models that currently do not adequately treat the negative charging areas. One specific test would be to measure the equilibrium voltage induced by the beam well above the effective second crossover energy to determine if the surface voltage is equal to either the difference E_o-E_2 or E_o-E_2^{eff}.

Section 3.2.1.2 develops the idea of using UV photon sample flooding to induce the photoelectric effect and dissipate negative surface potential. The instruments are in place, but lack of time has forced us to move forward without validation of the charge dissipation method or equipment. Having this capability would be of tremendous value. In Sections 4.1.2 and 4.2.2 we have shown yield curves that show significant charge related features at energies $>E_2$. We have speculated as to the nature of these features, but are unable to make measurements because there does not exist a time effective way of dissipating the negative charge that develops in this energy range. Using the electrostatic field probe, we could not only validate UV flooding of materials for discharging, but we could enhance our understanding of this region (E_1>E_o>E_2) of the yield curve.

5.2.5 Detector Characterization

Extensive work has been done to characterize the detector in this work and by previous researchers (Chang *et al.*, 1998; Nickles and Dennison, 2000; Nickles *et al.*, 2001; Thomson *et al.*, 2003), but there remains a few loose ends to tie up that will remove some minor but lingering concerns about detector functionality. Performing the following measurements will reduce error bars associated with both yield and spectral measurements.

Section 3.1.3 provides a treatment of electron emission spectra taken from biased conductors to show the basic behavior of the inner grid, sample and BSE peaks. This was used throughout Section 4 to infer negative surface potential. To measure spectra from positively

biased conductors, it will be necessary to perform a suite of measurements like those in Section 3.1.3, only with the sample and inner grid held at a positive bias. These measurements should contain combinations of positive biases on the inner grid and the sample to establish basic behavior. These voltages should not exceed 100 V as the spectral system cannot measure peaks any higher than that without upgrading the power supply that controls the discriminating voltage. This will allow the use of the spectral shift method of surface voltage determination on insulating materials with a positive potential. A better understanding of the effects of grid biasing may also be used to minimize the contamination of the SE spectra by the inner-grid peak by shifting the peak relative to the sample peak.

It was also shown throughout Section 4 that there is a small, secondary emission peak of roughly consistent intensity centered at ~42 eV. In this work, this small peak has been attributed to SE from some unspecified element in the detector and has largely been ignored. The source of this peak can be found by applying a few volt bias to each element in the HGRFA and taking an emission spectrum of a clean grounded Au sample. When the correct element is biased, the peak at ~42 eV will shift by the amount of the applied bias. Once the source of this peak is determined, efforts can then be taken to eliminate the peak altogether.

This work has required some modest modification to the HGRFA, most notable are several apertures drilled in the collector for the admission of flooding electrons and photons. These holes have reduced the collection area of the hemisphere by <1% and have introduced edges in the collection area that might change the overall efficiency of the collector. In order to maintain the <5% error in measuring absolute electron yields, we must be sure that the collector efficiency is well known. The work done by Thomson (2004) measures the efficiency of the detector in Section 4.3 of his dissertation. He finds a correction factor for the total yield of 1.15 in agreement with modeling of the detector by Nickles (2002), thus accounting for the 15% loss inherent to the HGRFA. I suggest we make the same measurements by taking the uncorrected

yield using a DC electron beam on a clean grounded Au sample; we then only need to adjust the incident energy until the sample current reads zero. We know by this that we have found the crossover energy and that the yield is unity by definition. The efficiency is then given by the ratio of the measured yield to the true yield of unity. As a corollary to this recalibration, measurements can be made from each detector element (sample, stage, inner grid, bias grid and detector) to confirm the separate component currents predicted by the detector modeling of Nickels *et al.* (2001).

5.2.6 Miscellaneous

The following measurements are those that do not fall easily into any category, but could still yield significant results by extending our understanding

It was considered in Section 3.2 that it might be possible to extend the limit of the pulse yield system to measure yields from insulators with an incident pulse that is an order of magnitude smaller that the lowest currently obtainable. This is accomplished, be taking advantage of the extremely fast electrometers developed by Zavyalov (2003) that are used to measure the currents from the pulsed yield system. These electrometers have rise times on the order of 1 μs. A typical pulsed yield is measured by capturing the signal from the electrometer and integrating the entire pulse with respect to time to get the total charge from each channel. The charge from each channel is then used to calculate the yield of the material. This has proven to be accurate and effective, but it might be possible to use the pulse and calculate the yield point-for-point along the entire curve instead of integrating it to find total charge. This would require careful characterization of the electron gun, HGRFA, electrometers, and any stray capacitance on the connecting cabling and inherent in the electrometer amplifiers. Such detailed characterization would be time consuming, but the payoff would be an order of magnitude decrease in the measurable probe pulse of the pulsed yield system. An added benefit would be that we may be able to extract useful information about the electron mobility as this experiment closely resembles

a time-of-flight measurement (Samarin *et al.*, 2003). Sim is developing applicable models of such time of flight experiments for the MPG systems (Sim, 2010).

Another set of work that was touched on in Section 4.2.3 is the effect of radiation damage on insulating materials. Section 4.2.3 is a brief glimpse into a wealth of data that has yet to be analyzed in any meaningful way. We have speculated that the unusual charging behavior is a result of the increased number of trap states in the band gap of the material. This would have broad implications on the conductivity and the production of SE's. It would provide a wealth of information to review this information using the models developed in Sim (2010). The primary goal of his work is to unify all the different models that exist for conduction, ESD, RIC, internal charge distribution and SE production and emission. This is based on the fundamental transport equations and should give good predictions as to how the basic characteristics of a material will change as trap sites are modified. We can then apply these predictions to this body of existing data and confirm or refute many of the speculations made in this work.

REFERENCES

Abbott, J., and J. Dennison, 2005, "Methods for Determining Crossover Energies in Insulating Materials," in *Proceedings of the Utah State University Student Showcase* (Logan, UT), p.385.

Alig, R., and S. Bloom, 1975, "Electron-Hole-Pair Creation Energies in Semiconductors," Phys. Rev. Lett. **35**, 1522.

Ashcroft, N., and N. Mermin, 1976, *Solid State Physics* (Holt Rinehart and Winston, New York).

Auday, G., P. Guillot, and J. Galy, 2000, "Secondary Emission of Dielectrics Used in Plasma Display Panels," J. Appl. Phys. **88**, 4871.

Baroody, E., 1950, "A Theory of Secondary Electron Emission from Metals," Phys. Rev. **78**, 780.

Bartnikas, R., 1987, *Engineering Dielectrics, Vol IIB: Electrical Properties of Solid Insulating Materials: Measurement Techniques* (ASTM International).

Bass, A., P. Cloutier, and L. Sanche, 1998, "Measurements of Charge Accumulation Induced by Monochromatic Low-Energy Electrons at the Surface of Insulating Samples," J. Appl. Phys. **84**, 2740.

Belhaj, M., S. Odof, K. Msellak, and O. Jbara, 2000, "Time-Dependent Measurement of the Trapped Charge in Electron Irradiated Insulators: Application to Alo–Sapphire," J. Appl. Phys. **88**, 2289.

Bethe, H., and W. Heitler, 1934, "On the Stopping of Fast Particles and on the Creation of Positive Electrons," in *Proceedings of the Royal Society of London. Series A, Containing Papers of a Mathematical and Physical Character* **146**, 83.

Boggio, J., and R. Plumb, 1966, "Theory of Formation of Very Thin Oxide Films on Metals," J. Chem. Phys. **44**, 1081.

Bruining, H., and J. De Boer, 1938, "Secondary Electron Emission: Part I. Secondary Electron Emission of Metals," Physica **5**, 17.

Brunson, J., 2009, Ph.D. dissertation (Utah State University).

Cazaux, J., 1999, "Some Considerations on the Secondary Electron Emission, Δ, from E Irradiated Insulators," J. Appl. Phys. **85**, 1137.

Cazaux, J., 2003, "Scenario for Time Evolution of Insulator Charging under Various Focused Electron Irradiations," J. Appl. Phys. **95**, 731.

Cazaux, J., 2005, "A New Model of Dependence of Secondary Electron Emission Yield on Primary Electron Energy for Application to Polymers," J. Phys. London-D Applied Physics **38**, 2433.

Chang, W., J. Dennison, P. Judd, and U. Logan, 2000a, "Measurements of Electronic Properties of Conducting Spacecraft Materials with Application to the Modeling of Spacecraft Charging," in *Proceedings of the 38th American Institute of Aeronautics and Astronomics on Aerospace Sciences* (Reno, NV).

Chang, W. Y., J. Dennison, J. Kite, and R. E. Davies, 2000b, "Effects of Evolving Surface Contamination on Spacecraft Charging," in *Proceedings of the 38th American Institute of Aeronautics and Astronomics Meeting on Aerospace Sciences* (Reno, NV).

Chang, W. Y., J. Dennison, N. Nickles, and R. E. Davies, 1998, "Utah State University Ground-Based Test Facility for Study of Electronic Properties of Spacecraft Materials," in *Proceedings of the 6th Spacecraft Charging Technology Conference* (Air Force Research Laboratory Science Center, Hanscom Air Force Base, MA).

Chang, W. Y., N. Nickles, J. Dennison, and C. D. Thomson, 2000c, "An Improved Database of Electronic Properties of Spacecraft Materials for Modeling of Spacecraft Charging," in *Proceedings of the 7th Spacecraft Charging Technology Conference* (Noordwijk, The Netherlands).

Chung, M., 1975, "Improved Calculations of Secondary Electron Energy Distributions of Metals," J. Appl. Phys. **46**, 465.

Chung, M., and T. Everhart, 1974, "Simple Calculation of Energy Distribution of Low Energy Secondary Electrons Emitted from Metals under Electron Bombardment," J. Appl. Phys. **45**, 707.

Chung, M., and T. Everhart, 1977, "Role of Plasmon Decay in Secondary Electron Emission in the Nearly-Free-Electron Metals. Application to Aluminum," Phys. Rev. B **15**, 4699.

Compton, D., G. Cheney, and R. Poll, 2004, "Radiation-Induced Conductivity in Plastic Films at High Dose Rates," J. Appl. Phys. **36**, 2434.

Connell, J., 2000, "The Effect of Low Earth Orbit Atomic Oxygen Exposure on Phenylphosphine Oxide-Containing Polymers," High Performance Polymers **12**, 43.

Corbridge, J., J. Dennison, and A. Hunt., 2008, "Radiation Induced Conductivity Measurements of Insulating Materials at Low Temperatures," in *Proceedings of the: 21st International Conference on the Application of Accelerators in Research and Industry* (Fort Worth, TX).

Davies, R., 1996, "An Instrument for Experimental Secondary and Backscattered Electron Investigations with Applications to Space Craft Charging," M.S. thesis (Utah State University).

Dawson, P., 1966, "Secondary Electron Emission Yields of Some Ceramics," J. Appl. Phys. **37**, 3644.

Dennison, J., 2008, "USU JWST Induced Electrostatic Breakdown ICIM Samples," in *Proceedings of the James Webb Space Telescope Spacecraft Charging Working Group Seminar* (NASA Goddard Space Flight Center, Greenbelt, MD).

Dennison, J., J. Abbott, R. Hoffman, and J. Corbridge, 2006a, "Electron Emission Testing of Solar Sail Nanocomposite Materials," (NASA Jet Propulsion Laboratory, Pasadena, CA) private communication.

Dennison, J., J. Brunson, S. Hart, J. Gillespie, J. Dekany, C. Sim, and D. Arnfield, 2009a, "Engineering Tool for Temperature, Electric Field and Dose Rate Dependence of High Resistivity Spacecraft Materials," in *Proceedings of the 47th American Institute of Aeronautics and Astronomics Meeting on Aerospace Sciences* (Orlando, FL).

Dennison, J., J. Brunson, P. Swaminathan, N. Green, and A. Frederickson, 2006b, "Methods for High Resistivity Measurements Related to Spacecraft-Charging," IEEE Trans. Plasma. Sci. **34**, 2191.

Dennison, J., A. Chang, N. Nickles, C. D. Thomson, J. Kite, and R. Davies, 2002, "Ground-Based Measurements Simulating Space Environment Interaction of Materials and See Spacecraft Charging Materials Database for Spacecraft Charging Modeling," in *Proceedings of the International Union of Radio Scientists (URSI) National Radio Science Meeting* (University of Colorado, Boulder, CO).

Dennison, J., A. Frederickson, and P. Swaminathan, 2003a, "Charge Storage, Conductivity and Charge Profiles of Insulators as Related to Spacecraft Charging," in *Proceedings of the 8th Spacecraft Charging Technology Conference* (NASA Marshall Space Flight Center, Huntsville, AL).

Dennison, J., J. Gillespie, J. Hodges, R. Hoffmann, J. Abbott, and A. W. Hunt, 2007, "Radiation Induced Conductivity of Highly-Insulating Spacecraft Materials," in *Proceedings of the 10th Spacecraft Charging Technology Conference* (Biarritz, France).

Dennison, J., and N. Green 2006c, "Recent Advances in Measurements Related to the Charging and Discharging of Spacecraft Materials," in *Proceedings of the AIAA Space Environments and Effects Working Group Annual Meeting* (Redondo Beach, CA).

Dennison, J., J. L. Hodges, J. Duce, and A. Evans, 2009c, " Flight Experiments on the Effects of Contamination on Electron Emission of Materials," in *Proceedings of the 1st AIAA Atmospheric and Space Environments Conference,* (San Antonio, TX).

Dennison, J., R. Hoffmann, J. Roth, and A. Sim, 2008, "Effects of Radiation Induced Conductivity on Samples Charged by Particle Beams," in *Proceedings of the 2008 Joint Fall Meeting of the Texas and Four Corners Sections of APS, AAPT, and Zones 13 and 16 of SPS, and the Societies of Hispanic and Black Physicists* (Fort Worth, TX).

Dennison, J., A. Sim, J. Brunson, S. Hart, J. Gillespie, J. Dekany, C. Sim, and D. Arnfield, 2009b, "Engineering Tool for Temperature, Electric Field and Dose Rate Dependence of High Resistivity Spacecraft Materials Paper Number," in *Proceedings of the 47th American Institute of Aeronautics and Astronomics Meeting on Aerospace Sciences* (Orlando, FL).

Dennison, J., C. Thomson, J. Kite, V. Zavyalov, and J. Corbridge, 2003b, "Materials Characterization at Utah State University: Facilities and Knowledgebase of Electronic Properties of Materials Applicable to Spacecraft Charging," in *Proceedings of the 8 th Spacecraft Charging Technology Conference,* (NASA Marshall Space Flight Center, Huntsville, Al).

Dennison, J., C. Thomson, J. Kite, V. Zavyalov, and J. Corbridge, 2004, "Materials Characterization at USU: Facilities and Knowledge Base of Electronic Properties Applicable to Spacecraft Materials," in *Proceedings of the 8th Spacecraft Charging Technology Confrence* (Huntsville, AL).

Dever, J., R. Messer, C. Powers, J. Townsend, and E. Wooldridge, 2001, "Effects of Vacuum Ultraviolet Radiation on Thin Polyimide Films," High Performance Polymers **13**, S391.

Dionne, G., 1975, "Origin of Secondary Electron Emission Yield Curve Parameters," J. Appl. Phys. **46**, 3347.

Donegan, M., J. Sample, J. Dennison, and R. Hoffmann, 2010, "Spacecraft Coating-Induced Charging: A Materials and Modeling Study of Environmental Extremes," J. Space. Rock. **47**, 134.

Doniach, S., and M. Sunjic, 1970, "Many-Electron Singularity in X-Ray Photoemission and X-Ray Line Spectra from Metals," J. Phys. C **3**, 285.

Dupont, 2010, "Technical Data Sheet," http://www2.dupont.com/Kapton/en_US/assets/downloads/pdf/HN_datasheet.pdf

Fowler, J., 1956, "X-Ray Induced Conductivity in Insulating Materials," in *Proceedings of the Royal Society of London. Series A, Mathematical and Physical Sciences* (1934-1990) **236**, 464.

Frederickson, A. R., and J. Dennison, 2003, "Measurement of Conductivity and Charge Storage in Insulators Related to Spacecraft Charging," in *Proceedings of the 2003 IEEE Nuclear and Space Radiation Effects Conference* (Monterey, CA).

Fredrickson, A. R., and J. Dennison, 2003, "Measurement of Conductivity and Charge Storage in Insulators Related to Spacecraft Charging," IEEE Trans. Nucl. Sci. **50**, 2284.

Girard, P., P. Charpenel, and H. Martin, 1992, "Determination of the Noncharging Electron-Beam Energy on Insulators," J. Appl. Phys. **71**, 2871.

Green, N., and J. Dennison, 2008, "Deep Dielectric Charging of Spacecraft Polymers by Energetic Protons," IEEE Trans. Plasma Sci. **36**, 2482.

Green, N., A. Frederickson, and JR Dennison, 2006a, "Experimentally Derived Resistivity for Dielectric Samples from the CRRES Internal Discharge Monitor," IEEE Trans. Plasma Sci. **34**, 1973.

Green, N. W., A. R. Frederickson, and J. Dennison, 2006b, "Charge Storage Measurements of Resistivity for Dielectric Samples from the CRRES Internal Discharge Monitor," IEEE Trans. Plasma Sci. **34**, 5.

Griffiths, D., and C. Inglefield, 1999, *Introduction to Electrodynamics* (Prentice Hall, Upper Saddle River, NJ).

Griseri, V., K. Fukunaga, T. Maeno, C. Laurent, L. Levy, and D. Payan, 2004, "Pulsed Electro-Acoustic Technique Applied to in-Situ Measurement of Charge Distribution in Electron-Irradiated Polymers," IEEE Trans. Dielectrics and Electrical Insulation **11**, 891.

Hansen, F. Y., L. W. Bruch, H. Taub, JR Dennison, V. Frank, and H. J. Lauter, 1989, "Theoretical and Experimental Studies of the Lattice Dynamics of a Commensurate Nitrogen Monolayer Adsorbed on Graphite," in *Proceedings of the APS March Meeting* (St. Louis, MO).

Hayward, W. C., 2009, "Controlled Resistivity Alumina "
http://www.wesgo.com/resist.htm

Henke, B., J. Liesegang, and S. Smith, 1979, "Soft-X-Ray-Induced Secondary-Electron Emission from Semiconductors and Insulators: Models and Measurements," Phys. Rev. B **19**, 3004.

Hodges, J., 2010, "In Situ Electric Field Measurements," M.S. thesis (Utah State University).

Hoffmann, R., and J. Dennison, 2006, "Effects of Fluence and Charge Density for Pulsed, Low-Fluence Measurements of Electron Emission in Highly Insulating Materials," in *Proceedings of the Four Corners Section of the APS Fall Meeting* (Logan UT).

Hoffmann, R., J. Dennison, C. Thomson, and J. Albretsen, 2008, "Low-Fluence Electron Yields of Highly Insulating Materials," IEEE Trans. on Plasma Sci. **36**, 2238.

Hoffmann, R., J. L. Hodges, J. Hayes and J. Dennison, 2009, "Measurement of Charging and Discharging of High Resistivity Materials Spacecraft Materials by Electron Beams," in *Proceedings of the 47th American Institute of Aeronautics and Astronomics Meeting on Aerospace Sciences* (Orlando, FL).

Jbara, O., M. Belhaj, S. Odof, K. Msellak, E. Rau, and M. Andrianov, 2001, "Surface Potential Measurements of Electron-Irradiated Insulators Using Backscattered and Secondary Electron Spectra from an Electrostatic Toroidal Spectrometer Adapted for Scanning Electron Microscope Applications," Rev. Sci. Instrum. **72**, 1788.

Joy, D., 1995, "A Database on Electron-Solid Interactions," Scanning **17**, 270.

Kanter, H., 1961, "Energy Dissipation and Secondary Electron Emission in Solids," Phys. Rev. **121**, 677.

Kite, J., 2007, "Secondary Electron Production and Transport Mechanisms by Measurement of Angle-Energy Resolved Cross Sections of Secondary and Backscattered Electron Emission," Ph.D. dissertation (Utah State University).

Klaffky, R., B. Rose, A. Goland, and G. Dienes, 1980, "Radiation-Induced Conductivity of Al_2O_3: Experiment and Theory," Phys. Rev. B **21**, 3610.

Levy, L., D. Sarrail, and J. Siguier, 1985, "Conductivity and Secondary Electron Emission Properties of Dielectrics as Required by NASCAP," in *Proceedings of the Third European Symposium on Spacecraft Materials in Space Environment* (Noordwijk, The Netherlands).

Lide, D., 1993, *CRC Handbook of Chemistry and Physics* (CRC Press, Boca Raton, FL).

Lye, R., and A. Dekker, 1957, "Theory of Secondary Emission," Phys. Rev. **107**, 977.

Mandell, M., I. Katz, and M. Hilton, 2001, "Nascap-2k Spacecraft Charging Models: Algorithms and Applications, in 2001: A Spacecraft Charging Odyssey," in *Proceedings of the 7th Spacecraft Charging Technology Conference* (Noordwijk, The Netherlands).

ManTech SRS Technologies, 2010, http://www.mantechmaterials.com/_images/documents/2_7_doc.pdf.

Melchinger, A., and S. Hofmann, 1995, "Dynamic Double Layer Model: Description of Time Dependent Charging Phenomena in Insulators under Electron Beam Irradiation," J. Appl. Phys. **78**, 6224.

Meyza, X., D. Goeuriot, C. Guerret-Piecourt, D. Treheux, and H. Fitting, 2003, "Secondary Electron Emission and Self-Consistent Charge Transport and Storage in Bulk Insulators: Application to Alumina," J. Appl. Phys. **94**, 5384.

Mizuhara, Y., J. Kato, T. Nagatomi, Y. Takai, and M. Inoue, 2002, "Quantitative Measurement of Surface Potential and Amount of Charging on Insulator Surface under Electron Beam Irradiation," J. Appl. Phys. **92**, 6128.

Morrell, R., 1987, *Handbook of Properties of Technical and Engineering Ceramics. Part 2: Data Reviews. Section I: High-Alumina Ceramics* (Her Majesty's Stationery Office, London, England).

National Institute of Standards and Technology, 2010a, "ESTAR, Stopping Power and Range Tables for Electrons" (http://physics.nist.gov/PhysRefData/Star/Text/ESTAR.html).

National Institute of Standards and Technology, 2010b, "Stopping power and Range tables for Electrons, Protons and Helium Ions" (http://www.nist.gov/physlab/data/star/index.cfm).

Nickles, N., 2002, "The Role of Bandgap in the Secondary Electron Emission of Small Bandgap Semiconductors: Studies of Graphitic Carbon," Ph.D. dissertation (Utah State University).

Nickles, N., W.Y. Chang, and J. Dennison, 2001, "Hemispherical Grid Retarding Field Analyzer for Absolute Measurement of Secondary and Back-Scattered Electron Yields," in *Proceedings of the American Physical Society March Meeting,* (Seattle, WA).

Nickles, N., R. Davies, and J. Dennison, 1998, "Applications of Secondary Electron Energy-and Angular-Distributions to Spacecraft Charging," in *Proceedings of the 6th Spacecraft Charging Conference,* (AFRL Science Center, Hanscom AFB, MA).

Nickles, N., and J. Dennison, 2000, "Instrumentation and Measurement of Secondary Electron Emission for Spacecraft Charging," in *Proceedings of the 6th Rocky Mountain NASA Space Grant Consortium NASA Fellowship Symposium,* (Salt Lake City, UT).

Oliphant, D., 2009, "The Modified Chung and Everhart Model for Secondary Electron Energy Distribution," (Utah State University) private communication.

Osawa, N., S. Takahashi, Y. Tanaka, T. Takada, R. Watanabe, N. Tomita, V. Griseri, L. Levy, and C. Laurent, 2003, "Measurement of Bulk Charge in Dielectric Materials Irradiated by Electron Beam in Vacuum Environment," in *Proceedings of the 8th Spacecraft Charging Technology Conference,* (Huntsville, AL).

Otterstrom, J., and J. Dennison, 2005, "Pulsed System for Optical Discharge of Thin-Film Insulators," in *Proceedings of the Utah State University Student Showcase,* (Logan, UT).

Quinn, J., 1962, "Range of Excited Electrons in Metals," Phys. Rev. **126**, 1453.

Reimer, L., 2000, "Scanning Electron Microscopy: Physics of Image Formation and Microanalysis," Measurement Sci. Technol. **11**, 1826.

Rose, A., 1951, "An Outline of Some Photoconductive Processes," RCA Rev. **12**, 362.

Roth, J. A., R. Hoffmann, and J. Dennison, 2008, "Observation and Characterization of Electrostatic Discharge in Insulating Materials Induced by Electron Beam Bombardment," in *Proceedings of the American Physical Society Four Corner Section Meeting* (University of Texas-El Paso, El Paso , TX).

Roth, J. A., R. Hoffmann, and J. Dennison, 2009, "Effects of Radiation Induced Conductivity on Electrostatic Discharge in Insulating Materials," in *Proceedings of the 1ˢᵗ AIAA Atmospheric and Space Environments Conference* (San Antonio, TX).

Samarin, S., O. Artamonov, D. Waterhouse, J. Kirschner, A. Morozov, and J. Williams, 2003, "Highly Efficient Time-of-Flight Spectrometer for Studying Low-Energy Secondary Emission from Dielectrics: Secondary-Electron Emission from Lif Film," Rev. Sci. Instrum. **74**, 1274.

Schwoebel, P., and I. Brodie, 1995, "Surface-Science Aspects of Vacuum Microelectronics," J. Vac. Sci. Technol. B **13**, 1391.

Seiler, H., 1983, "Secondary Electron Emission in the Scanning Electron Microscope," J. Appl. Phys. **54**, R1.

Shih, A., J. Yater, C. Hor, and R. Abrams, 1997a, "Secondary Electron Emission Studies," Appl.Surf. Sci. **111**, 251.

Shih, A., J. Yater, P. Pehrsson, J. Butler, C. Hor, and R. Abrams, 1997b, "Secondary Electron Emission from Diamond Surfaces," J. Appl. Phys. **82**, 1860.

Shugg, W., 1970, *Handbook of Electrical and Electronic Insulating Materials; the Guide to Plastics by the Editors of Modem Plastics Encyclopedia,* Vol. 2, (McGraw-Hill, New York).

Sim, A., 2010, "A Unified Theory of Charge Dynamics in Highly Insulating Materials," Ph.D. dissertation (Utah State University).

Sim, A., J. Dennison and C. Thomson, 2005, "Evolution of the Electron Yield Curves of Insulators as a Function of Impinging Electron Fluence and Energy," in *Proceedings of the 9ᵗʰ Spacecraft Charging Technology Conference* (Epochal Tsukuba, Japan).

Spencer, L., 1955, "Theory of Electron Penetration," Phys. Rev. **98**, 1597.

Staib Instruments, 2002, "Instruction Manual Electron Gun Model EK-5-S".

Sternglass, E., 1950, "Secondary Electron Emission and Atomic Shell Structure," Phys. Rev. **80**, 925.

Stolz, H., and H. Streitwolf, 1958, "The Theory of Secondary Electron Emission from Metals," Z. Nautrforsch.

Swaminathan, P., 2004, "Measurement of Charge Storage Decay Time and Resistivity of Spacecraft Insulators," M.S. thesis (Utah State University).

Takada, T., H. Miyake, and Y. Tanaka, 2006, "Pulse Acoustic Technology for Measurement of Charge Distribution in Dielectric Materials for Spacecraft," IEEE Trans. on Plasma Sci. **34**, 2176.

Tanuma, S., C. Powell, and D. Penn, 2005, "Calculations of Stopping Powers of 100 eV to 30 keV Electrons in 10 Elemental Solids," Surf. Inter. Anal. **37**, 978.

Thomson, C., 2004, "Measurements of the Secondary Electron Emission Properties of Insulators," Ph.D. dissertation (Utah State University).

Thomson, C. D., V. Zavyalov, and J. R. Dennison, 2003, "Instrumentation for Studies of Electron Emission and Charging from Insulators," in *Proceedings of the 8th Spacecraft Charging Technology Conference,* (NASA Marshall Space Flight Center, Huntsville, AL).

Thomson, J., 1897, "Cathode Rays," Philosophical Magazine **44**, 293.

Usui, Y., T. Sakai, M. Ishikawa, T. Isono, Y. Tanaka, T. Takada, R. Watanabe, and N. Tomita, 2003, "Measurement of Charge Distribution in Electron Beam Irradiated PMMA Using Electro-Optical Effect," in *Proceedings of the 8th Spacecraft Charging Technology Conference* (Huntsville AL).

Whetten, N., 2004, "Cleavage in High Vacuums of Alkali Halide Single Crystals—Secondary Electron Emission," J. Appl. Phys. **35**, 3279.

Willis, R., and D. Skinner, 1973, "Secondary Electron Emission Yield Behavior of Polymers," Solid State Commun **13**, 685.

Wilson, G., and J. Dennison, 2010, "Approximation of Range in Materials as a Function of Incident Electron Energy," in *Proceedings of the 11th Spacecraft Charging and Technology Confrence,* (Albuquerque, NM).

Wintle, H., 1983, *Conduction Processes in Polymers, Vol. IIA* (American Society for Testing and Materials, Baltimore, MD).

Yoshimura, M., and H. Bowen, 2006, "Electrical Breakdown Strength of Alumina at High Temperatures," J. Am. Ceram. Soc. **64**, 404.

Zangwill, A., 1988, *Physics at Surfaces* (Cambridge University Press, Cambridge, MA).

Zavyalov, V., 2003 (Available from JR Dennison at jr.dennison@usu.edu, Logan, UT) private communication.